INFORMATION TRANSFER IN OPEN QUANTUM SYSTEMS
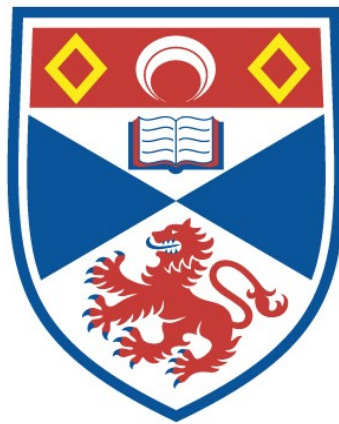
Elliott Kendrick Levi

A Thesis Submitted for the Degree of PhD
at the
University of St Andrews
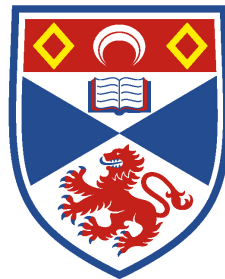
2017

Information Transfer in Open Quantum Systems

Elliott Kendrick Levi

University of
St Andrews

This thesis is submitted in partial fulfilment for the degree of Doctor
of Philosophy
at the
University of St Andrews

August 26, 2016

1. Candidate's declarations:

I, Elliott Kendrick Levi, hereby certify that this thesis, which is approximately 45000 words in length, has been written by me, and that it is the record of work carried out by me, or principally by myself in collaboration with others as acknowledged, and that it has not been submitted in any previous application for a higher degree.

I was admitted as a research student in September 2012 and as a candidate for the degree of Doctor of Philosophy in September 2012; the higher study for which this is a record was carried out in Heriott-Watt University between 2012 and 2013 and in the University of St Andrews between 2013 and 2016.

I, Elliott Kendrick Levi, received assistance in the writing of this thesis in respect of language, grammar, spelling and syntax, which was provided by Doctor Peter Kirton

Date   signature of candidate

2. Supervisor's declaration:

I hereby certify that the candidate has fulfilled the conditions of the Resolution and Regulations appropriate for the degree of Doctor of Philosophy in the University of St Andrews and that the candidate is qualified to submit this thesis in application for that degree.

Date   signature of supervisor

3. Permission for publication:

In submitting this thesis to the University of St Andrews I understand that I am giving permission for it to be made available for use in accordance with the regulations of the University Library for the time being in force, subject to any copyright vested in the work not being affected thereby. I also understand that the title and the abstract will be published, and that a copy of the work may be made and supplied to any bona fide library or research worker, that my thesis will be electronically accessible for personal or research use unless exempt by award of an embargo as requested below, and that the library has the right to migrate my thesis into new electronic forms as required to ensure continued access to the thesis. I have obtained any third-party copyright permissions that may be required in order to allow such access and migration, or have requested the appropriate embargo below.

The following is an agreed request by candidate and supervisor regarding the publication of this thesis:

PRINTED AND ELECTRONIC COPY
Embargo on abstract and Chapter 5 of print and electronic copies for a period of 1 year on the following ground:
- Publication would preclude future publication

Date   signature of candidate   signature of supervisor

Please note initial embargos can be requested for a maximum of five years. An embargo on a thesis submitted to the Faculty of Science or Medicine is rarely granted for more than two years in the first instance, without good justification. The Library will not lift an embargo before confirming with the student and supervisor that they do not intend to request a continuation. In the absence of an agreed response from both student and supervisor, the Head of School will be consulted. Please note that the total period of an embargo, including any continuation, is not expected to exceed ten years.
Where part of a thesis is to be embargoed, please specify the part and the reason.

"They've done studies, you know. 60% of the time, it works every time."

Brian Fantana, Anchorman

Abstract

This thesis covers open quantum systems and information transfer in the face of dissipation and disorder through numerical simulation.

In Chapter 3 we present work on an open quantum system comprising a two-level system, single bosonic mode and dissipative environment; we have included the bosonic mode in the exact system treatment. This model allows us to gain an understanding of an environment's role in small energy transfer systems. We observe how the two-level system-mode coupling strength and the spectral density form characterising the environment interplay, affecting the system's coherent behaviour. We find strong coupling and a spectral density resonantly peaked on the two-level system oscillation frequency enhances the system's coherent oscillatory dynamics.

Chapter 4 focusses on a physically motivated study of chain and ladder spin geometries and their use for entanglement transfer between qubits. We consider a nitrogen vacancy centre qubit implementation with nitrogen impurity spin-channels and demonstrate how matrix product operator techniques can be used in simulations of this physical system. We investigate coupling parameters and environmental decay rates with respect to transfer efficiency effects. Then, in turn, we simulate the effects of missing channel spins and disorder in the spin-spin coupling. We conclude by highlighting where our considered channel geometries outperform each other.

The work in Chapter 5 is an investigation into the feasibility of routing entanglement between distant qubits in 2D spin networks. We no longer consider a physical implementation, but keep in mind the effects of dissipative environments on entanglement transfer systems. Starting with a single sending qubit-ancilla and multiple addressable receivers, we show it is possible to target a specific receiver and establish transferred entanglement between it and the sender's ancilla through eigenstate tunnelling techniques. We proceed to show that eigenstate tunnelling-mediated entanglement transfer can be achieved simultaneously from two senders across one spin network.

Acknowledgements

The last four years have been filled with the typical highs and lows that accompany a PhD. Despite it being common knowledge that there will be good days, weeks and months and bad days, weeks and months, it is nearly impossible to prepare a PhD student for how tough those bad periods can be. However we don't go through them alone.

I'd first like to thank my supervisor, because without Brendon Lovett this thesis would not exist. I am happy that I made the right choice in him and working with him has been an enjoyable way to achieve what I have. It could never be overstated, the effect that a good supervisor has on their students. Thanks need also go to my collaborators, Elinor Irish and Peter Kirton, whose experience and knowledge helped me reach the lofty heights of published academic authorship. The academic and administerial staff of the CM-CDT have provided help, advice and phenomenal organisational skills and ensured that no place I ever work will be run as well or by such friendly people.

A person can't exist on work alone and I've made a lot of friends in the time documented by this thesis. Too many to name, it would be unfair on those I mistakenly forgot. Those of you who contributed to keeping me occupied, whether it be a trip to the cinema, a board game night, cake day or something else entirely, know who you are. I hope you know you were a welcome and necessary part of what I've been through, torment and all.

Finally I'd like to make a dedication. My thesis is dedicated to my grandparents, those still with me and those passed. Barry, Elsie, Geoff, Joyce and Mildred have had an unwavering faith and confidence in me for as long as I can remember. They have always been extremely supportive and I hope, even if they never see this, they know how much that all means to me.

Publications

[1] *Coherent exciton dynamics in a dissipative environment maintained by an off-resonant vibrational mode* E. K. Levi, E. K. Irish, and B. W. Lovett, Phys. Rev. A **93**, 042109 (2016).

[2] *Designing spin-channel geometries for entanglement distribution* E. K. Levi, P. G. Kirton, and B. W. Lovett, Phys. Rev. A **94**, 032302 (2016).

Contents

1

Introductions and the way forward

THE universe, as a whole, is a closed system and every sub-system within it is therefore an open system. In general, systems are 'things'; ecosystems, cars, computers, atoms. Closed systems are contained, so only the system's parts dictate its behaviour whereas an open system has some interaction with external entities. To fully describe the behaviour of an open system the external environment must be considered. Definitions of closed and open systems do vary slightly with the scale of the physics being studied, for instance classically closed means no forces are exerted from outside and matter and energy are conserved. Thermodynamically a closed system permits energy flow but no matter, when both matter and energy exchanges are absent it would be an isolated system (similar to a closed classical mechanical system). And in standard quantum mechanics an isolated thermodynamic system is usually termed a closed system; one governed by the Schrödinger equation where no information (meaning energy or matter) can enter or leave the system (see Fig. 1.1). Conversely then, generally an open quantum system (OQS) is free to exchange information and energy with its environment.

It is not uncommon to approximate an OQS or its surrounding environment through various mathematical techniques and physical assumptions [1, 2], but as physics progresses and we wish to harness the great powers of quantum mechanics our understanding must evolve and so must our models. As quantum devices come more heavily into the focus of the scientific and industrial communities we are reminded that there is still a large amount for us to learn about OQSs; a great jigsaw still decades from completion. It is as pieces of this jigsaw we wish this thesis and

Open system

Closed system
approximation
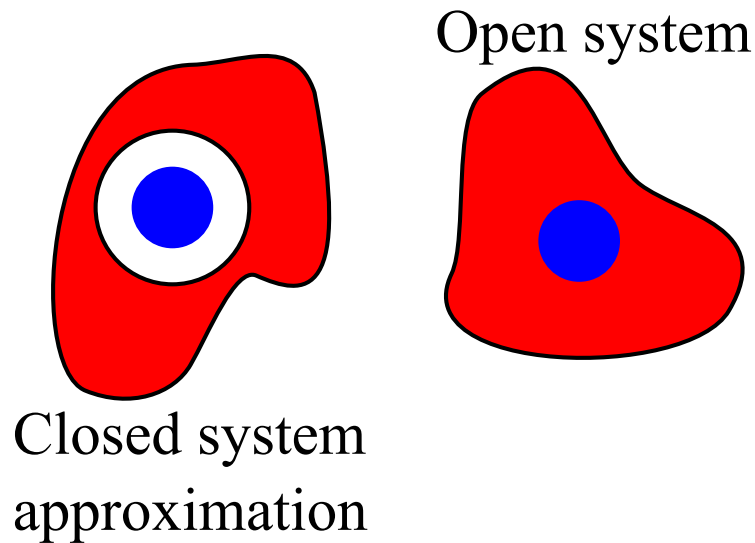
FIGURE 1.1: Schematic illustrations of closed and open quantum systems. A closed system (left) where only the circular blue 'system' is considered and the environment is either functionally or approximately uncoupled; information (such as energy or particles) is conserved within the system. The open system (right) is now in contact with its environment and in general information can flow between them. As such, information in the blue system is now not conserved.

the work within to serve. We concern ourself with investigations of a few different aspects of the OQS jigsaw; extending methods, considering novel system realisations and subverting expectations with regards to intuitive concepts.

1.1 Thesis overview

AIRLY traditionally this thesis is split into chapters covering the work carried out over the period of study and comprising extra material to support it. We have already introduced the highest level motivation and intent for the work in this chapter. We shall continue to outline and explore the thesis here, introducing in more detail the concepts associated with OQSs and what we intend to do.

1.1.1 Open quantum systems theory

In Chapter 2 we extend the concepts introduced here with the mathematical formalisms and techniques required for their study and description. Specifically the requirement for density matrices which generalise the description of a state beyond

state vectors due to the latter's inability to describe OQSs. The environment itself, although often vastly complex and numerically intractable must be handled in some way and this will be discussed. We will detail a master equation formalism for modelling an OQS in contact with an environment and the matrix product operator approach to solving a master equation. Finally we cover a measure of entanglement which we employ in later chapters to quantify system performance.

1.1.2   Maintenance of coherent dynamics in a dissipative environment

Chapter 3 is our first chapter of original work (forming the basis for Publication 1) and concerns the interplay between a system and its environment when part of that environment is being considered as a component of the system. This is a novel example of extending current methods to reduce the level of approximation used to treat environments and the precise formulation of the model could be thought of as a toy for photosynthetic systems. Making use of a symmetry-exploiting transformation, a 'microscopic' (as opposed to phenomenological) master equation is derived and a computational solution of it described in order to describe the system exactly. We show that exact treatment of this included environmental component leads to interesting behaviour, in that by tuning its coupling within the system one can change the coherent properties of the system. An analytic interpretation of this effect is presented and its relation to the description of the environment is explored.

1.1.3   Entanglement transfer spin channel geometries

Shifting focus, Chapter 4 features work (covered in Publication 2) contributing to the understanding of nitrogen vacancy centre (NV) based quantum computing implementations, as well as pushing the boundaries of simulations of such systems. It is clear, from the multitude of processes, algorithms and devices that rely on it, that entanglement is vital to quantum engineering and here we study a physically motivated realisation of its distribution between spatially separated qubits. The idea of using spin chains as a channel between qubits has been seen to be effective in the past, but here we extend this to ladders of spins and compare the behaviours of the

two kinds of channel in the face of an imperfect hypothetical manufacturing process. Part of our results will be obtained using a matrix product operator approach, employing it beyond the usual application to theoretical models and performing it in such a way as to extend what sized systems can be studied. We find that there is, once again, an interplay between the environment and system affecting coherent dynamics. Further, when the manufacturing imperfections are considered it is possible for a ladder to outperform a chain in terms of entanglement distribution, but perhaps not to the degree that was expected when one considers the extra couplings present in a ladder geometry.

1.1.4   Entanglement routing

Born of the considerations of the preceding chapter, Chapter 5 asks: if we can distribute entanglement between pairs can we send it in an addressable way and, if so, can multiple transmission processes coexist? Relaxing the physical restrictions slightly and considering this more as a question answered with a physically inspired toy model, we consider 2D grids of spins (a superset of the ladder and chain geometries considered previously) with sender and receiver qubits coupled to them. In consideration of what is possible we return to an idea investigated in earlier work associated with quantum state transfer, namely eigenmode transport, showing that with this it is indeed theoretically possible to route entanglement from a sender. Using this process we can distinguishably route entanglement, initially between the sender and an ancilla, such that at some time later only a desired receiver (one of multiple coupled to the spin network) is entangled with the ancilla. Then, extending this, we incorporate a second sender-ancilla pair and show that concurrent routing events can be realised with similar distinguishability.

1.2   Open Quantum Systems

AVING seen what will be included in this thesis let us go back and look at why we are interested in doing this work. It would be fair to say that the theoretical difficulties faced with an OQS approach to modelling are akin to those faced in many

body physics, in the sense that we currently cannot hope to deal with all of the states of a system and its surrounding environment exactly. As an aside, throughout this thesis the terms 'environment', 'bath' and 'surroundings' will be used more or less interchangeably to describe the same thing. With an OQS the stance is often adopted that, as we are not interested in the state of the environment, it is assumed to be of a simplified form that is easier to manage and can approximate averaged behaviours or weakly coupled parameter limits. But there are cases when the environment has been shown to be important, such as with the revelation of the quantum coherent processes in photosynthetic systems [3–5], which we will now discuss.

1.2.1 Photosynthesis

Despite being at the forefront of a lot of experimental [6–9] and theoretical [10–19] inquiry we have still only part knowledge as to the sources of the coherence and how precisely it enhances the transport efficiency of the photosynthetic process [20–22]. Some of the big open questions in the field include how to best model complicated biological structures accurately, whether *ex-vivo* experiments displaying coherence under coherent light sources can shed light on *in-situ* operation [23–25] and whether the coherence observed is electronic, vibrational or some mixture [26–28].

It might not be immediately obvious what the role of a physicist studying photosynthesis is, so let us provide an introduction to the process. Photosynthesis is the most common instance of converting energy on the planet [29] and is vital in supporting nearly all non-bacterial life on the planet [30]. Whilst the molecular description of the structures that mediate the many steps in this complicated process differ between organisms, the overall procedure follows the same description [30] and a schematic diagram can be seen in Fig. 1.2. Light harvesting complexes (LHCs) absorb photons, creating electronic excitations (excitons), which then migrate towards a reaction centre where the charge separated state is harnessed to perform chemical reactions. These two structures, the LHC and the reaction centre, are the primary constituents of a photosynthetic unit. LHCs are collections of chromophores, or pigments, that absorb light (i.e. have an electronic structure amenable to photoexcitation) and typically

a reaction centre is comprised of two closely spaced chromophores.
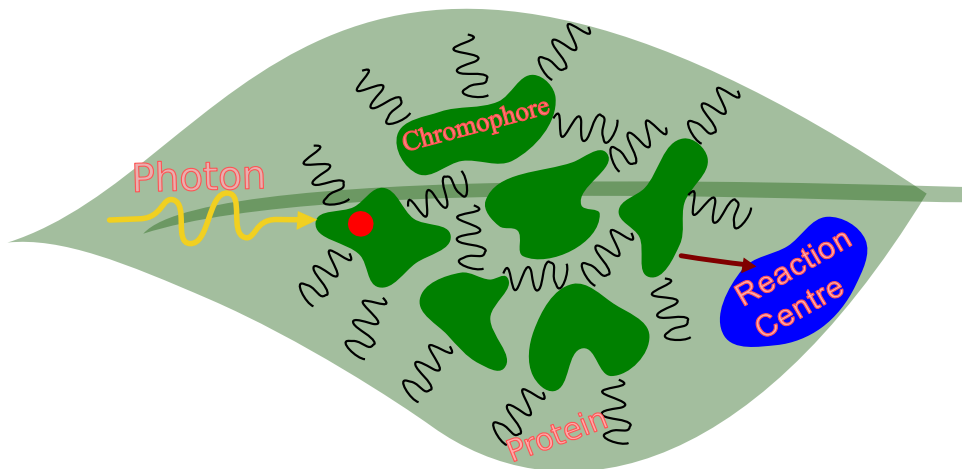
FIGURE 1.2: A schematic impression of a photosynthetic unit comprised of chromophores (collectively forming the light harvesting complex), the reaction centre (where the chemical process is initiated) and a surrounding protein environment.

There are a range of chromophores (like chlorophylls or carotenoids) with different properties; generally each is responsive to a different part of the electromagnetic spectrum and can also serve to protect the organism by absorbing light that would otherwise be damaging to the plant [31]. In many instances chromophores are surrounded by a protein basket, referred to together as a pigment-protein complex, and since changes to the protein's conformation also affect the chromophore the spectral properties of the latter can be tuned [32]. A chlorosome is another pigment structure that has been observed in LHCs, these are large collections of chromophores bound together without protein baskets [33].

Whilst much is known about the biological and chemical structure and operation of the different photosynthetic units, there is still more to learn about the physics of energy transfer through the unit. The chemical make up of a photosynthetic unit for a particular organism is a good basis for understanding the physical dynamics of the system, however the information is sometimes too much to deal with; a full molecular description of an LHC is certainly beyond a fully quantum mechanical simulation for instance. Fig. 1.3 illustrates some of the different information that can be obtained and represented using a particular LHC (the Fenna-Matthews-Olsen (FMO) complex) as an example [34].
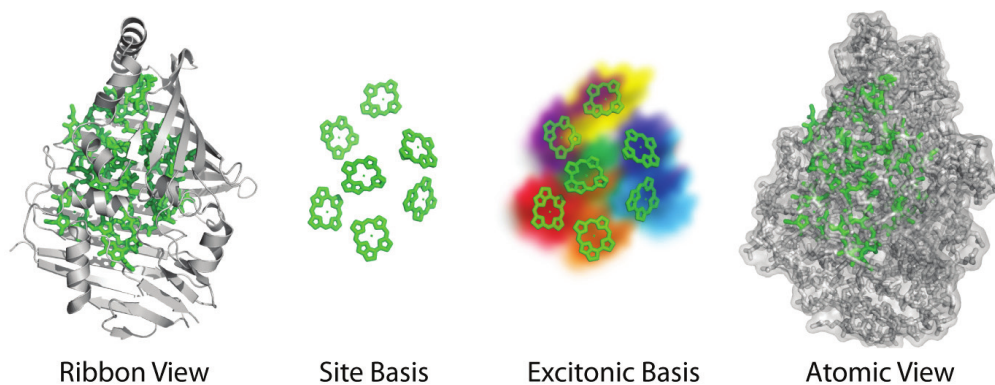
FIGURE 1.3: Four representations of the Fenna-Matthews-Olsen LHC. The ribbon view shows a biological representation of the protein ribbons surrounding the green chromophores. The site basis identifies the individual chromophores which, in the case of this organism, are chlorin rings. The excitonic basis is a physical representation of the density clouds (represented as different colours) of the single excitation associated with each chromophore. Finally the atomic view shows how densely packed this LHC is and just how many constituent atoms there are to consider. Figure obtained from Ref. [34].

As previously mentioned, it is known that the exciton travels through the chromophores to reach the reaction centre, but the precise mechanism by which this occurs is unknown. The energy dynamics can be probed using spectroscopic techniques and commonly used now in photosynthetic studies is 2D electronic spectroscopy. This uses four-wave-mixing and elicits third order correlations in the form of an emitted signal field resulting from the laser-sample interaction [35]. This technique represents a step forward in our probing technologies as one of its big advantages is that the spectrum obtained is in terms of amplitudes (as opposed to intensities) so the system's quantum phase is directly accessible; this means that quantum coherence can be observed.

Traditionally the belief was that biological systems were too 'warm and wet' to depend on anything other than classical descriptions because quantum states are fragile things; clearly the results for photosynthesis say otherwise. So we have said that coherence can be measured, how those measurements are achieved and given an overview of the system in which this is all taking place, but let us give a physical interpretation for how electronic coherence might emerge (or remain in the face of an active environment) in a system like this. A two parameter discussion can successfully explain the two limiting cases of the dynamics which are illustrated in Fig. 1.4. The two parameters can either be energies or time scales (one being related to the inverse

of the other). Starting with energies we shall consider the inter-chromophore electronic coupling strength and the bath-chromophore interaction strength. When bath-chromophore beats electronic coupling, chromophore localised electronic states make the most logical basis states, with a perturbative treatment of inter-chromophore excitonic coupling; this approach is called Förster theory [36]. This limit can be thought of as a hopping limit, where the electron exists on one site at a time, and hops between chromophores. In the opposing limit, when the electronic coupling is greater than bath-chromophore interactions, a localised electron is not a convenient state description as it may delocalise across chromophores; now the bath-chromophore couplings are treated perturbatively to produce a quantum master equation, such as in Redfield theory [37].
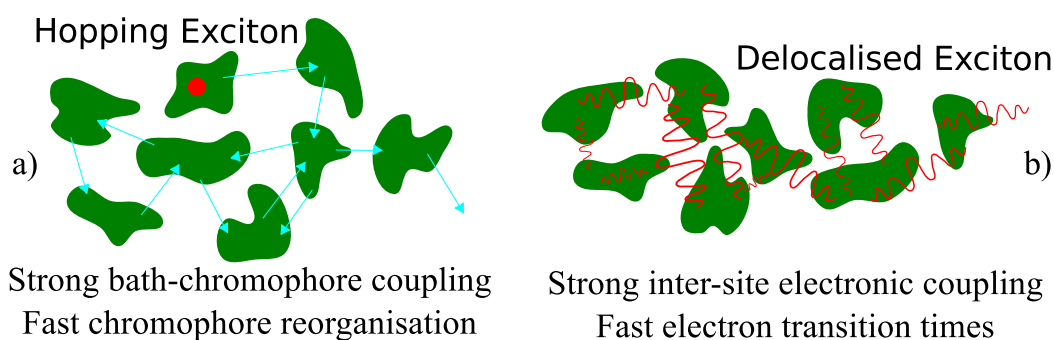
FIGURE 1.4: Illustrations of electronic behaviour in the a) hopping and b) delocalised regimes of chromophoric energy transfer.

A consideration in terms of time scale parameters reinforces this picture; the time scales are the electron transition (between chromophores) and nuclear reorganisation times. The presence of an excited electron on a chromophore presents it with an energetic change that the molecular structure wants to act to minimise; the time it takes to do this is the nuclear reorganisation time. If the reorganisation is fast (by comparison) then any transfer happens after the rapid structural change has decohered the state of the electron and behaviour can be described as similar to a classical random walk; here we are again in the hopping regime. An active surrounding protein environment would, if strongly coupled, cause similar electronic decoherence, hence the equivalent regime. Correspondingly if the electronic transfers are rapid, occurring before the bath or reorganisation has had time to decohere its state, then a delocalised electron description would be suitable; one way to increase transfer speeds would

be to have strong inter-chromophoric couplings so again we see an understandable equivalence.

Whilst there are systems that these limiting coupling and/or time scale regimes can describe there are also a large number of cases where the parameters fall into intermediate or competing regimes. Theoretical consideration here is hampered due to the inapplicability of common perturbative or 'weak coupling' approaches because of the lack of vanishingly small parameters. In order to investigate the regime where chromophoric coupling is of the same scale as chromophore-protein coupling it is worth noting that whilst precise models of whole LHCs can elucidate *in situ* performance they tend to be computationally expensive and may produce a lot of information. As we are still at a stage of understanding where the mechanisms themselves are still in question, it can be physically instructive to proceed with studies of smaller systems or more manageable toy models. In doing so approximations are made that reduce the possibility of quantitative comparisons with real systems, however the qualitative, physical conclusions drawn from such work can help move forward our understanding of basic governing principles. Chapter 3 contains work that has been motivated by such thinking, taking a system that whilst not quantitatively representative does capture the essence of several physical systems where there is a complex interplay between system and environment.

1.2.2 Quantum state transfer

The system-environment interplay is also of interest in the fields of quantum computing and devices, where quantum coherence is often an invaluable resource; decoherence has been widely studied but is still a topic where there is more to be done [38–43]. It is beyond the scope of this body of work to introduce the entire quantum fields of computing, devices and cryptography so we shall focus on one pertinent practice: quantum state transfer (QST) along spin-1/2 chains. This might seem like a unusual shift, but inherently any device designed to implement such a process can be described as an OQS, with the originating and destination qubits as well as the chain itself existing in contact with some environment. For instance, a solid state

implementation will exist inside (or possibly on top of) a crystalline environment, constantly experiencing phononic vibrations similar to the protein baths of our previous example. We can also still use many of the already established OQS methods and techniques then to investigate this novel application of quantum mechanics.

The use of spin-1/2 chains as QST channels is a well covered subject [44–46] and has been extended to dual- [47] and multi-rail [48, 49] spin chains. The intent is simple, take an arbitrary quantum state $|\psi\rangle = a|\uparrow\rangle + b|\downarrow\rangle$ defined on one sending qubit and transfer it to a second receiving qubit whilst maintaining high fidelity. It is this last point, maintenance of high fidelities, that motivates study as this is clearly an area where understanding how a system interacts with its environment can pave the way for new device constructions and scientific advancements.

In Fig. 1.5 we present the basic structure required for such a QST process. There are a number of ways QST can be implemented along a chain such as this, including modulating spin energies and controlling couplings between them [50–55]. The way we consider here is a minimal control approach, in so far as the chain is dark and control of the process is governed only by the state qubits themselves. As we have presented it in Fig. 1.5 the system is uniform in spin placements (spacings) but in general the idea of dark spin wiring that we will introduce does not need this to be the case.
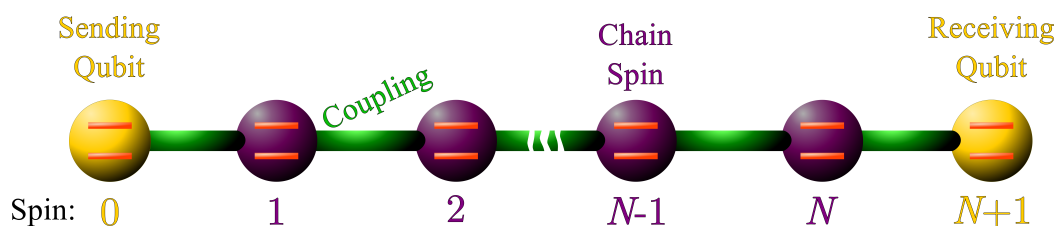
FIGURE 1.5: Illustration of a spin-1/2 chain quantum state transfer system. The sender qubit is initialised in an arbitrary state which, as the system evolves, is transferred to the receiving qubit.

If one considers a system where the couplings of the state qubits to the chain are weak, compared to the intra-chain couplings, then the process of an excitation moving onto the chain can be treated perturbatively. Being in this weak coupling regime means that the qubits can effectively excite a single eigenstate of the chain if

the Zeeman splitting of the qubits match it; this is represented in Fig. 1.6. With perturbative state qubit-chain interactions one is able to solve the eigen-system of the isolated chain and obtain its eigenvalues. We can restrict ourselves to considering only the single excitation states of the chain as transport eigenmodes as the sender qubit can only introduce one excitation; this assumes the chain is initially all spin down. Theoretically this operating mode can transport the state with very high fidelity as interference due to phase effects of differing transfer speeds through different eigenstates of the chain are minimised.
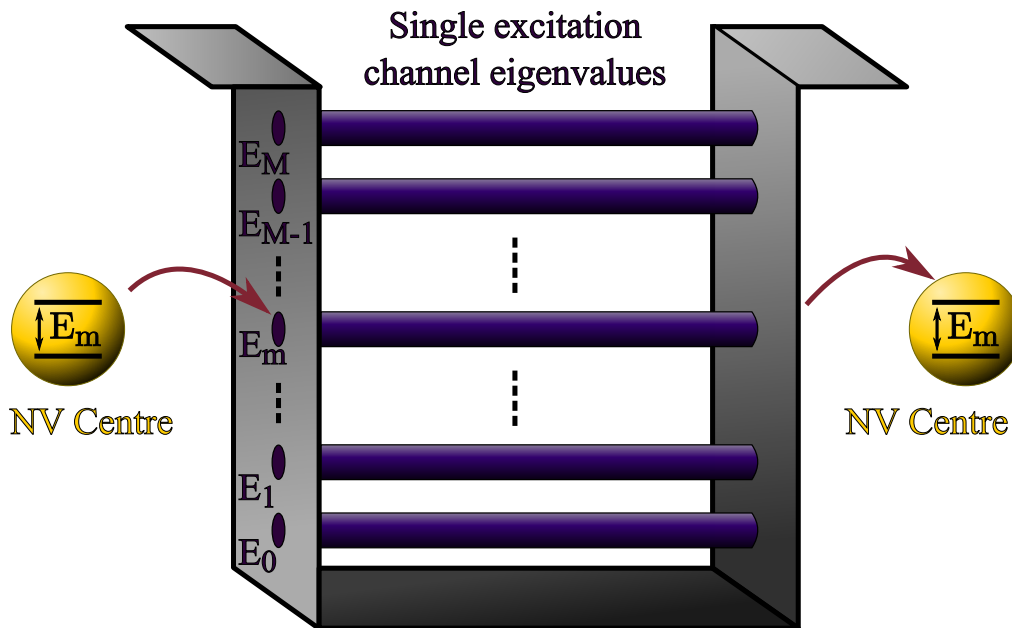
FIGURE 1.6: A schematic of the eigenmode tunnelling mechanism of spin channel wiring. Provided the qubit-chain coupling is weak compared to the intra-chain coupling then transfer via only one mode occurs which is free from interference effects and thus is of high fidelity.

1.2.3 Nitrogen vacancy centres

Theory of this minimal control technique, for transferring a quantum state, naturally requires implementation in order to progress and in 2011 a proposal was made to use the popular, diamond-based, nitrogen vacancy centre (NV) qubits wired by nitrogen impurities placed between them [56]. As displayed in Fig. 1.7, an NV is a substitutional nitrogen atom in diamond neighbouring a crystal vacancy and a nitrogen impurity lacks this neighbouring vacancy. NV centre implementations are one of the current front-runners in the quantum computer race [57] due to their long

(room temperature) electron and nuclear spin decoherence times [58, 59]. They are also amenable to precise measurement and manipulation [60] which has led to an experimentally realisable set of universal quantum operations [61, 62]. And their fluorescence properties make them experimentally convenient ways of interfacing between optics and solid state schemes.
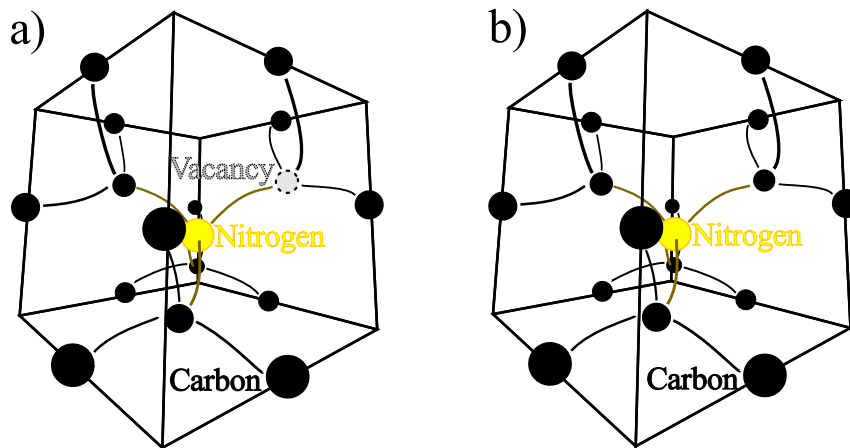
FIGURE 1.7: a) A diamond unit cell with one missing carbon atom and one nitrogen atom substitution forming an NV. b) A single substitutional nitrogen atom in a diamond unit cell which is known as a nitrogen impurity.

An NV has a (ground) multi-level electronic structure as depicted in Fig. 1.8, clearly not a neat two level system, however we can control it as if it were, isolating two levels [61, 63]. The system can be initialised in $|\downarrow\rangle$ through optical pumping to excited levels and non-radiative decay via the singlet state [64]. A magnetic field can split the degenerate $m_s = \pm 1$ levels [60] and we can define the $m_s = 0$ and $m_s = 1$ as $|\downarrow\rangle$ and $|\uparrow\rangle$ respectively giving us a well defined two level basis. Finally with microwave pulses the coherent control of $|\downarrow\rangle$ and $|\uparrow\rangle$ can be implemented [65].

1.2.4 Entanglement distribution

A full OQS consideration of an NV implementation of the dark spin QST process requires inclusion of the decay rates inherent to the crystal which introduces a phonon environment. Unfortunately the work of Ping *et al.* showed realistic spin and phase decay time scales prove prohibitive for high fidelity QST using this method [63]. It was also shown here that this implementation could be suitable for entanglement
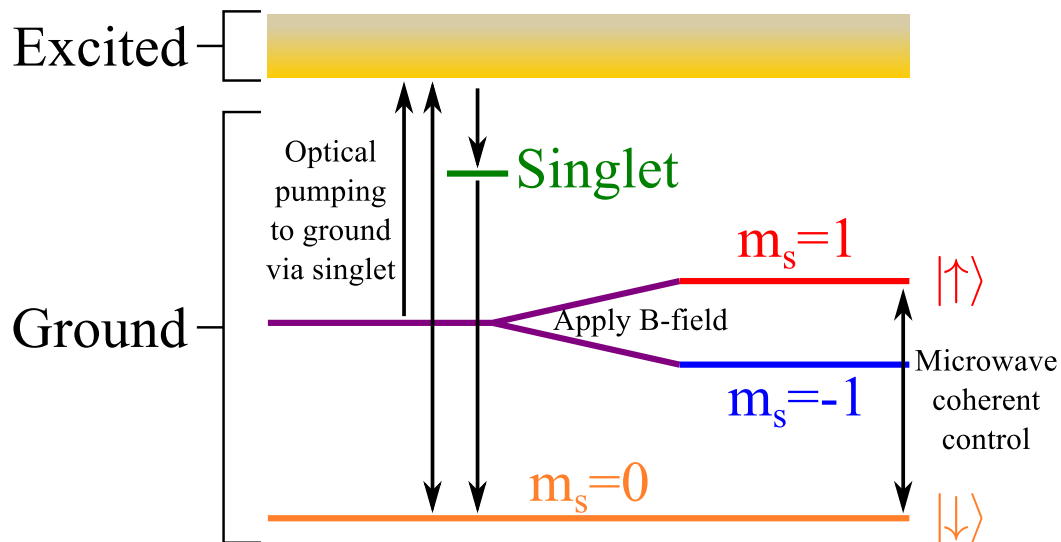
FIGURE 1.8: The simplified electronic structure of an NV with the relevant computational basis levels labelled. Application of a magnetic field causes splitting of the degenerate triplet levels. Optical pumping achieves an initialised down state and through microwave control the up state can be populated coherently.

distribution where perfect fidelity transfer is not necessarily required. Whilst many quantum frontier implementations are still a little way off, one constant theme appears to be entanglement; in realisations of quantum computing [66, 67], cryptography [68, 69] and metrology [70, 71] there is clearly a need for the creation of entangled states.

Spatially separate parties will likely require access to created entangled states so distribution methods are also important. A major problem with distribution via direct transmission will likely be the noisy transfer environment, however there are ways to circumvent this drawback. For instance, it has been shown theoretically that two distant systems can be entangled via a separable ancilla [72, 73] and experimentally realised with photons [74] and Gaussian beams [75, 76]. Another possibility is counterfactual entanglement which is created with no physical interaction [77, 78]. The method of entanglement distillation [79–81] is also promising: a large ensemble of weakly entangled pairs are distributed and through local operations and classical communication are refined into a small ensemble of highly entangled pairs.

In Chapters 4 and 5 we consider this concept of distributing entanglement, envisioning the subsequent use of a distillation protocol. To this end we do not require

perfect fidelity and we therefore choose, in Chapter 4, to extend the understanding of distribution mechanisms by comparing two geometries of spin wire implemented with NVs and impurities. The work in Chapter 5 takes the distribution idea further. We consider more complex geometries, handling large rectangular lattices of spins, to study the more complex process of routing entanglement. While there is not a hard and fast definition of what this means, our interpretation follows the idea that it should be possible to distribute information between multiple receivers in an addressable manner [82].

2

Open quantum systems theory

ONTAINED within this chapter, will be an introduction to the methods and techniques of open quantum systems (OQSs), specifically for obtaining time dependent dynamics. We will first highlight the tool used for description of the systems themselves, density matrices, then move onto to how we formulate a description of a system's evolution using quantum master equations. Finally we shall cover one method for solving a quantum master equation using matrix product operator techniques and include details on the measure of entanglement we employ in later chapters which becomes our assessment of system performance.

By way of an introduction, consider the difference between pure and mixed states. When a system is in a pure state writing a state vector, or a superposition thereof, is one way of describing it. For example, $|\Psi\rangle = \sum_i C_i |i\rangle$ is a superposition of the basis states $\{|i\rangle\}$, these and their superposition are pure states; we have complete information about the phase of the basis states. Suppose that we did not have all of this information, but instead we are presented with an ensemble of these systems after undergoing a measurement. Now we have a statistical mixture of the state outcomes that can no longer be represented as a state vector; this is a mixed state.

If we lack a state vector description we require something else to describe our system and that is what a density matrix achieves; density matrices are completely positive, Hermitian and have trace unity [83]. Sometimes called a density operator and traditionally given the symbol ρ, a density matrix allows us to describe a quantum state in complete generality, regardless of it being pure or mixed. The purity

(or conversely mixedness) of a state is a continuous property measured as $\text{Tr}\left(\rho^2\right)$. A purity of 1 is perfectly pure and a maximally mixed state of dimension d has purity $1/d$.

We can freely write a density matrix as

$$\rho = \sum_j p_j \left|\psi_j\right\rangle \left\langle\psi_j\right|, \tag{2.1}$$

where we describe a quantum system made up of a statistical mixture of states, $\left|\psi_j\right\rangle$, each weighted by a probability p_j. This description encompasses both pure and mixed states. Returning to our previous expression of a pure state we have only one element in the summation over j, our superposition $\left|\Psi\right\rangle$. As our superposition is the state with certainty this implies $p_1 = 1$ and therefore perfect purity. We could of course expand the superposition in its basis bringing two (one for the ket and one for the bra) summations over the basis: $\rho = \left|\Psi\right\rangle \left\langle\Psi\right| \rightarrow \sum_{ii'} C_i C_{i'} \left|i\right\rangle \left\langle i'\right|$. When $i = i'$ we get the diagonal elements of ρ with the probabilities of the basis states, and for all $i \neq i'$ we obtain the off diagonal 'coherence' elements of ρ which contain information about the phase relation between the states in this basis. Any density matrix can be written in a diagonal basis and whilst this would necessarily change the coherences visibly present between basis states it would not change the purity of the density matrix.

Alternatively let us imagine an experiment in which someone is provided with an ensemble of spin-1/2 particles prepared in the basis $\{\left|\uparrow\right\rangle, \left|\downarrow\right\rangle\}$. Although the distributor of the spins knows the superposition state coefficients ($\left|\psi\right\rangle = \alpha \left|\uparrow\right\rangle + \beta \left|\downarrow\right\rangle$) the recipients do not and as such, following measurements in the preparation basis, they find themselves in a mixed state with only statistical information available. The recipient can use a description like Eq. 2.1, with $\psi_j \in \{\uparrow, \downarrow\}$ and the corresponding p_j's as the results of their measurements; i.e. given repeated experiments the probability of what the spin orientation would be. They would have only diagonal elements of ρ in this basis which means their degree of understanding of the system does not include coherence information and is mixed to some degree. Measurements performed in a complimentary basis could help the recipient learn more about the coherence

properties of their states.

If we write a state vector representation for the system and environment of an OQS, initialised in some coherent way then, should we be able to proceed with a theoretical treatment of this full representation, we would see pure state evolution (assuming the environment is decoupled from the universe). It is commonly the case that it is impossible to fully formulate the complexities of an environment and we must partially trace it out so as to treat only the system

$$\rho_\mathrm{S} = \mathrm{Tr}_\mathrm{E}\left(\rho\right). \tag{2.2}$$

In effect this introduces mixedness into the system description based on how the environment acts on average; the resulting system density matrix ρ_S is said to be 'reduced'. This mixing can be thought of as the environment performing some measurement on the state to which an observer is unaware of the result. One can also say that mixedness implies the environment and system have become entangled.

2.1 Dynamical density matrices

PRESENTED then with an OQS that can no longer in general be described using a state vector, we have to move beyond the Schrödinger equation to an equation of motion for density matrices; such an equation is called a quantum master equation. In the remainder of this chapter we shall endeavour to stick to the convention of using 'OQS' to refer to the system we are interested in and the environment it is openly interacting with; technically, combined as this, our OQS is closed. When we use 'system' that will be the system part of the OQS. For a full OQS density matrix the equivalent to the Schrödinger equation $\left(|\dot{\psi}_j(t)\rangle = -i\hat{H}|\psi_j\rangle\right)$ is

$$\dot{\rho}(t) = \sum_j p_j |\dot{\psi}_j\rangle \langle\psi_j| + p_j |\psi_j\rangle \langle\dot{\psi}_j| = \sum_j p_j(-i)\hat{H}|\psi_j\rangle \langle\psi_j| + p_j i |\psi_j\rangle \langle\psi_j|\hat{H}$$

$$= -i\left[\hat{H}, \rho(t)\right] = \mathcal{L}\rho(t), \tag{2.3}$$

where we have chosen the convention $\hbar = 1$ as we do throughout this thesis. This is the Liouville-von Neumann equation [1] and is the most general example of a quantum master equation. The $\hat{H}$ in Eq. (2.3) is a Hamiltonian for the entire OQS, system and environment, and we have defined $\mathcal{L}$ which is the Liouville superoperator; a superoperator acts on operators to produce operators. The integrated solution of this equation, for the evolution of this density matrix then is

$$\rho(t) = e^{\mathcal{L}t}\rho(0), \tag{2.4}$$

in analogy to the time evolution of a state vector, $|\psi(t)\rangle = \exp\left(-i\hat{H}t\right)|\psi(0)\rangle$. This clearly is not always a simple equation to write an explicit form of or indeed employ for calculation of $\rho(t)$ due to the complexity of the full OQS Hilbert space and its operators.

Thus far we have considered a Schrödinger picture, where any time dependence resides with state vectors (which extends to the density matrix as well). Let us reformulate in the interaction picture, where time dependence is shared between states and operators, to progress towards a more tractable form of Eq. (2.3). We start by acknowledging the Schrödinger picture OQS Hamiltonian can be split into $\hat{H} = \hat{H}_0 + \hat{H}_I$, with the first part generally containing isolated system and environment terms (i.e. their energies) and the second describing interactions between the system and its environment. The form of this splitting can vary a lot depending on the system studied, or which techniques are going to be (or have been) applied. Conversion of the density matrix and interaction Hamiltonian to the interaction picture, using the unitary $\hat{U}_0 = \exp\left(-i\hat{H}_0 t\right)$, follows as

$$\rho^{(\mathrm{I})}(t) = \hat{U}_0^\dagger \rho(t)\hat{U}_0 \tag{2.5}$$

$$\hat{H}_I^{(\mathrm{I})}(t) = \hat{U}_0^\dagger \hat{H}_I \hat{U}_0, \tag{2.6}$$

with the (I) superscript indicating the interaction picture and noting that $\rho^{(\mathrm{I})}(t = 0)$ coincides with the Schrödinger picture $\rho(t = 0)$.

Differentiating Eq. (2.5) we obtain an interaction picture version of Eq. (2.3) [84]

$$
\begin{aligned}
\dot{\rho}^{(\mathrm{I})}(t) =& i\hat{H}_0\hat{U}_0^{\dagger}\rho(t)\hat{U}_0 - i\hat{U}_0^{\dagger}\rho(t)\hat{H}_0\hat{U}_0 + \hat{U}_0^{\dagger}\dot{\rho}(t)\hat{U}_0 \\
=& i\left[\hat{H}_0, \rho^{(\mathrm{I})}(t)\right] - i\hat{U}_0^{\dagger}\left[\hat{H}, \rho(t)\right](t)\hat{U}_0 \\
=& i\left[\hat{H}_0, \rho^{(\mathrm{I})}(t)\right] - i\left[\hat{H}_0, \rho^{(\mathrm{I})}(t)\right] - i\left[\hat{H}_{\mathrm{I}}^{(\mathrm{I})}(t), \rho^{(\mathrm{I})}(t)\right] \\
=& -i\left[\hat{H}_{\mathrm{I}}^{(\mathrm{I})}(t), \rho^{(\mathrm{I})}(t)\right].
\end{aligned}
\tag{2.7}
$$

This can also be written in an integral form

$$
\rho^{(\mathrm{I})}(t) = \rho^{(\mathrm{I})}(0) - i\int_0^t \left[\hat{H}_{\mathrm{I}}^{(\mathrm{I})}(s), \rho^{(\mathrm{I})}(s)\right]\mathrm{d}s.
\tag{2.8}
$$

What we have presented so far enables us, broadly speaking, to find the dynamics for a composite (system-environment) OQS density matrix. Should we have an OQS that has a simple or convenient analytical form we could use a Liouville-von Neumann equation to obtain an expression for the composite density matrix. Following from this we can calculate the reduced $\rho_{\mathrm{S}}(t)$ for the system (which is typically what we are interested in). But an environment is a tricky thing to deal with on account of its large Hilbert space, so relying on a dynamical description where this is required explicitly and completely (as it is in our descriptions so far) can often create an intractable problem. To tackle this issue we will now approach a derivation of a particular example of an approximate master equation, allowing us to obtain reduced dynamics for $\rho_{\mathrm{S}}(t)$, without requiring analytic computation of the entire combined system-environment problem.

2.1.1 Born-Markov master equation

The Born-Markov master equation is a widely used and recognised time local formulation that allows one, by inclusion of the two eponymous assumptions, to describe the reduced dynamics of a system. Its derivation can be found in a number of places [1, 83, 84] and what follows treads this familiar ground, describing the approximations made and introducing the formulation. For clarity, the general Hamiltonian splitting we performed earlier can be thought of as being comprised of $H_0 = H_{\mathrm{S}} + H_{\mathrm{E}}$,

that is system and environment parts acting only on those respective areas and the H_I describing the interaction between them.

We start from the interaction picture Liouville-von Neumann equation and its integral form in Eqs. (2.7) and (2.8), noticing that we can substitute the latter into the former

$$\dot{\rho}^{(\mathrm{I})}(t) = -i \left[\hat{H}_I^{(\mathrm{I})}(t), \rho^{(\mathrm{I})}(0) - i \int_0^t \left[\hat{H}_I^{(\mathrm{I})}(s), \rho^{(\mathrm{I})}(s) \right] \mathrm{d}s \right]$$
$$= -i \left[\hat{H}_I^{(\mathrm{I})}(t), \rho^{(\mathrm{I})}(0) \right] - \int_0^t \left[\hat{H}_I^{(\mathrm{I})}(t), \left[\hat{H}_I^{(\mathrm{I})}(s), \rho^{(\mathrm{I})}(s) \right] \right] \mathrm{d}s \qquad (2.9)$$

Now we carry out a partial trace over the environment to provide us with the reduced system dynamics

$$\dot{\rho}_S^{(\mathrm{I})}(t) = -\int_0^t \mathrm{Tr}_E \left(\left[\hat{H}_I^{(\mathrm{I})}(t), \left[\hat{H}_I^{(\mathrm{I})}(s), \rho^{(\mathrm{I})}(s) \right] \right] \right) \mathrm{d}s, \qquad (2.10)$$

where we have assumed $\mathrm{Tr}_E \left(\left[\hat{H}_I^{(\mathrm{I})}(t), \rho^{(\mathrm{I})}(0) \right] \right) = 0$ without loss of generality.

To proceed, we introduce the Born approximation which will allow us to express both sides of Eq. (2.10) in terms of the reduced density matrix; a desirable goal as it lifts the requirement for complete knowledge of the environmental state. It does this by acknowledging a weak coupling approximation between the system and the environment such that the system has a negligible influence on the dynamics of the environment and as such it remains unchanged from its initial state $\rho_E(t) = \rho_E(0) = \rho_E$. If we assume, due to this weak coupling, initially we had a separable state, then we can write for all times that $\rho(t) \approx \rho_S(t) \otimes \rho_E$ (which holds in both the Schrödinger and interaction pictures). Due to this approximation Born-Markov master equations are sometimes also referred to as weak coupling master equations. Employing the Born approximation allows us to write Eq. (2.10) as

$$\dot{\rho}_S^{(\mathrm{I})}(t) = -\int_0^t \mathrm{Tr}_E \left(\left[\hat{H}_I^{(\mathrm{I})}(t), \left[\hat{H}_I^{(\mathrm{I})}(s), \rho_S^{(\mathrm{I})}(s) \otimes \rho_E \right] \right] \right) \mathrm{d}s; \qquad (2.11)$$

a slightly simpler problem now as we require the reduced system density matrix and the initial state of the environment as opposed to previously needing the full OQS density matrix.

Unfortunately Eq. (2.11) is still not time local, it requires information about the history of the reduced density matrix. The Markov approximation helps us with this, stating that the system dynamics at any given instant in time do not have any memory of what happened before, allowing us to make the change $\rho_S^{(I)}(s) \to \rho_S^{(I)}(t)$:

$$\dot{\rho}_S^{(I)}(t) = -\int_0^t \mathrm{Tr}_E \left(\left[\hat{H}_I^{(I)}(t), \left[\hat{H}_I^{(I)}(s), \rho_S^{(I)}(t) \otimes \rho_E \right] \right] \right) \mathrm{d}s; \qquad (2.12)$$

this form is known as the Redfield equation. This assertion of memoryless dynamics is valid given the physical interpretation that any correlations present in the environment decay over a time scale τ_E which is much shorter than the dynamical time scale of the system, τ_S. There is a second simplification $\tau_E \ll \tau_S$ can imply: the lower limit of the integrand can be extended down to $-\infty$ due to the fact that we have rapidly vanishing correlations which imply the integrand will vanish for $s \gg \tau_E$. Applying this and the substitution $s = t - s'$ we reach

$$\dot{\rho}_S^{(I)}(t) = -\int_0^\infty \mathrm{Tr}_E \left(\left[\hat{H}_I^{(I)}(t), \left[\hat{H}_I^{(I)}(t - s'), \rho_S^{(I)}(t) \otimes \rho_E \right] \right] \right) \mathrm{d}s'. \qquad (2.13)$$

The Born-Markov master equation we have now in Eq. (2.13) is still very general, but is time local and can generate the reduced system dynamics given an interaction Hamiltonian and the initial environmental and reduced system density matrices. The application of the Markov approximation essentially amounts to a coarse graining of time: we look not at the fast τ_E but proceed considering dynamics on the scale of τ_S. In our application of the Born approximation, although we assumed a weakly coupled, negligibly affected environment that does not mean there are no excitations in it, but when we couple this with the Markov assumption of rapidly decaying bath correlations we see that these excitations are coarse grained out.

2.1.2 Lindblad master equation

The Lindblad form for a master equation is again well covered [1, 83, 84] and is the most general master equation formulation that ensures the complete positivity of the reduced density matrix; a necessary condition if we wish to interpret its diagonal

entries as probabilities. In Chapter 3 we give a derivation, starting from Eq. (2.13) and using the Hamiltonian and system defined for a particular OQS, to express a Lindblad master equation. Here we proceed to elucidate in broader strokes how we can reach the Lindblad form by highlighting the key extra assumption that goes into its formulation, the secular approximation.

First consider one term in the double commutator of Eq. (2.13)

$$
\begin{aligned}
\Xi &= \hat{H}_{\mathrm{I}}^{(\mathrm{I})}(t)\hat{H}_{\mathrm{I}}^{(\mathrm{I})}(t-s') \cdot \rho_{\mathrm{S}}^{(\mathrm{I})}(t) \otimes \rho_{\mathrm{E}} \\
&= \mathrm{e}^{(i\hat{H}_0 t)}\hat{H}_{\mathrm{I}}\mathrm{e}^{(-i\hat{H}_0 t)}\mathrm{e}^{(i\hat{H}_0(t-s'))}\hat{H}_{\mathrm{I}}\mathrm{e}^{(-i\hat{H}_0(t-s'))} \cdot \mathrm{e}^{(i\hat{H}_{\mathrm{S}} t)}\rho_{\mathrm{S}}\mathrm{e}^{(-i\hat{H}_{\mathrm{S}} t)} \otimes \mathrm{e}^{(i\hat{H}_{\mathrm{E}} t)}\rho_{\mathrm{E}}\mathrm{e}^{(-i\hat{H}_{\mathrm{E}} t)} \\
&= \mathrm{e}^{(i\hat{H}_0 t)}\hat{H}_{\mathrm{I}}\mathrm{e}^{(-i\hat{H}_0 t)}\mathrm{e}^{(i\hat{H}_0(t-s'))}\hat{H}_{\mathrm{I}}\mathrm{e}^{(-i\hat{H}_0(t-s'))} \cdot \mathrm{e}^{(i\hat{H}_{\mathrm{S}} t)}\rho_{\mathrm{S}}\mathrm{e}^{(-i\hat{H}_{\mathrm{S}} t)} \otimes \rho_{\mathrm{E}},
\end{aligned}
\tag{2.14}
$$

where we have shown explicitly the conversion to the interaction picture and expanded $\hat{H}_0 = \hat{H}_{\mathrm{S}} + \hat{H}_{\mathrm{E}}$ around the separated density matrices. Now suppose we can decompose the interaction Hamiltonian into operators that correspond to the system and environment subspaces such that

$$
\hat{H}_{\mathrm{I}} = \sum_{\mu\epsilon} \hat{S}_\mu(\epsilon) \otimes \hat{E}_\mu,
\tag{2.15}
$$

where we implicitly require that the $\hat{S}$ are projected in the eigenbasis of $\hat{H}_{\mathrm{S}}$, with the ϵ dependence due to a difference of eigenbasis projector eigenvalues, and noting $\hat{H}_{\mathrm{I}}^{(\mathrm{I})} = \left(\hat{H}_{\mathrm{I}}^{(\mathrm{I})}\right)^\dagger$. We can then split the exponentiated $\hat{H}_0$'s as we did for the density matrix above and convert these sub-operators to the interaction picture in Eq. (2.14)

$$
\Xi = \sum_{\mu\nu\epsilon\epsilon'} \mathrm{e}^{i\epsilon' t}\hat{S}_\mu^\dagger(\epsilon') \otimes \left(\hat{E}_\mu^{(\mathrm{I})}\right)^\dagger(t) \cdot \mathrm{e}^{-i\epsilon(t-s')}\hat{S}_\nu(\epsilon) \otimes \hat{E}_\nu^{(\mathrm{I})}(t-s') \cdot \rho_{\mathrm{S}}^{(\mathrm{I})}(t) \otimes \rho_{\mathrm{E}},
\tag{2.16}
$$

where the action of the picture changing unitary exponentials on the system operators is to select eigenvalues of the system projectors.

Proceeding to separate Ξ into system and environment terms as

$$\Xi = \sum_{\mu\nu\epsilon\epsilon'} \Xi_S \otimes \Xi_E,$$

$$\Xi_S = e^{i(\epsilon'-\epsilon)t} \hat{S}_\mu^\dagger(\epsilon') \hat{S}_\nu(\epsilon) \rho_S^{(I)}(t),$$

$$\Xi_E = e^{i\epsilon s'} \left(\hat{E}_\mu^{(I)}\right)^\dagger(t) \hat{E}_\nu^{(I)}(t-s') \rho_E, \tag{2.17}$$

we group terms containing the integration variable into the environment component allowing us to perform the integration and the trace only on this component; the partial trace over the environment acting on environmental operators effectively reproduces the trace. The complex exponential in Ξ_S will give oscillating contributions in the summand which can be rapid if $|\epsilon' - \epsilon|$ is large. The secular approximation can be used here and assumes that all contributions for which $\epsilon \neq \epsilon'$ are rapid and only terms containing $\epsilon = \epsilon'$ are included in the summand as they will have meaningful impact considering the coarse grained time scale τ_S of the Markov approximation.

Expanding the double commutator in Eq. (2.13), applying a decomposition as in Eq. (2.17) and enforcing the secular approximation are what is required to derive a Lindblad form from a Born-Markov master equation. We now present then a general Lindblad master equation in the Schrödinger picture:

$$\dot{\rho}_S(t) = -i\left[\hat{H}'_S, \rho_S(t)\right] + \sum_{\mu\nu} \Upsilon_{\mu\nu}\left(2\hat{S}_\nu\rho_S(t)\hat{S}_\mu^\dagger - \left\{\hat{S}_\mu^\dagger\hat{S}_\nu, \rho_S(t)\right\}\right). \tag{2.18}$$

The first term describes the unitary dynamics of the reduced system, directly equivalent to Eq. (2.3); if there was no environment or it was decoupled we would only have this term. The second term is called the dissipator and it contains the environmental interaction aspect of the dynamics. The $\hat{S}$ operators are the system operators acting to change the state of the system density matrix incoherently with a rate determined by Υ. This rate is the result of the integration and partial trace in Eq.(2.13) on Ξ_E as mentioned earlier when describing Eq. (2.17). The unitary dynamics term can no longer in general be interpreted as consisting of the bare system Hamiltonian, hence the prime. The rate integrals are principal value integrals, with the (typically small) principal value parts contributing Lamb shifts to the bare system Hamiltonian in the

first term. This Lindblad form can be simplified further by diagonalising with respect to the summand operators ($\mu, \nu \to \mu'$), with the new dissipator operators being known explicitly as Lindblad operators.

Lindblad-form master equations need not be obtained following the microscopic procedure described in this chapter of first deriving a Born-Markov equation and continuing to Lindblad form. A phenomenological approach can be taken whereby the form is achieved based on intuition of how the system being dealt with will operate. A microscopic approach is taken in Chapter 3 whereas a phenomenological approach is taken in Chapters 4 and 5.

2.2   Characterising environments

NCLUSION of the environment in a master equation generally follows a different procedure if one is using a phenomenological method as opposed to a microscopic derivation. Suppose we have two interacting two level qubits (spins) in a crystalline environment, an OQS for which we wish to define a Lindblad-form master equation. We imagine also that there has been experimental studies of equivalent systems in the past to determine the quantum properties of the qubits. A common piece of information obtained in such instances is coherence times of qubits. Typically there are two coherence times that are of interest: the state relaxation time (T_1) and the phase coherence time (T_2). State refers to, for example, the ability to ensure a spin initialised up remains so and often dissipation of this type is said to cause spin-flip errors. Phase refers to the coherence between qubits due to relative phase, with any 'phase-flip' errors due to interactions between the many surrounding phase components of the environment. Both of these time scales indicate how long the relative piece of quantum information remains coherent and in some sense 'quantum'.

2.2.1 Phenomenology

If we wish to use a diagonal Lindblad master equation defined phenomenologically for this system it is possible to define our dissipator such that the decay rate is experimentally informed by a physical property of the system being considered. This process can be done considering the summation range in a diagonal version of Eq. (2.18) to consist of simply a sum over qubits. Then, to impose the dissipation induced error we are choosing to consider, each qubit has one associated operator, tensor producted with the relative identity matrix to match dimensions. This way of conceptualising the dissipation assumes the bath is uncorrelated between spins, but of course this can be extended to considering multiple types of error or environmental actions including correlations.

Spin-flip errors can be modelled using $\hat{\sigma}^X$ and $\hat{\sigma}^\pm$ operators where $\hat{\sigma}^X = \hat{\sigma}^+ + \hat{\sigma}^-$ is the Pauli spin matrix composed of raising and lowering operators. One can think of $\hat{\sigma}^-$ and $\hat{\sigma}^+$ as operators giving and taking from the bath respectively; e.g. the $\hat{\sigma}^-$ flips an up spin down corresponding to an energy increase for the bath. In general the rates of these two operations can be different, but $\hat{\sigma}^X$ dissipation could be used with a decay rate of $1/T_1$ as an approximate spin-flip dissipation. Phase-flip errors can be modelled with a decay rate of $1/T_2$ using $\hat{\sigma}^Z$ operators which induce a relative phase change between the levels of a spin. Obviously this same thought experiment discussion can be had with regards to qudits and their relevant operators.

The nitrogen vacancy centres introduced in Chapter 1 are a good example of a system that can be (and is) modelled using this sort of approach; something we ourselves do in Chapter 4. Although we start with one, we chose not to include a dissipative environment for the entirety of Chapter 5. This decision was partly due to the fact that we do not consider a specific physical implementation. Also, because the processes we model here are similar to those in Chapter 4, we can make informed observations without the presence of dissipation as we know from Chapter 4 it will act to reduce the effectiveness of the processes but not destroy it.

2.2.2 Derivation

In order to derive a Lindblad-form master equation, for the example OQS of two cou-
pled spins in a crystalline environment that we introduced at the start of this section,
one requires a description of the environment in terms of operators to build the Ξ_E
of Eq. (2.17). It is quite common to describe a bath as a series of phonon modes, us-
ing a harmonic oscillator description, where each mode couples to the system with
a certain energy. Phononic environments can be thought of as delocalised because
typically the phonon wave function can have a large spatial extent; it is this type of
bath we consider repeatedly in this thesis. The crystalline environment in our current
section example lends itself well to phononic description, as do the protein baths we
discussed in Chapter 1 that play such an important role in photosynthetic systems.
Our derivation in Chapter 3 is also given for a system where we assume a phononic
environment form. Another type of bath descriptor used (but not considered here) is
a spin bath which might be suitable when the environment is dominated by charged
impurities and at low temperatures; such baths usually coincide with local impurity
descriptions such as electronic charge fluctuations.

To generate a Lindblad master equation we recall from Eqs. (2.13) and (2.17) that
one must perform a partial trace and time integration over Ξ_E. We shall demonstrate
now how to perform these operations and what considerations are borne having cho-
sen to use a bosonic harmonic environment picture. This will be done using a simple
example and leaving explanation of some of the finer points for our derivation in
Chapter 3. In this picture the environment is described by a series of harmonic oscil-
lators with the $\mathbf{k}$-th mode having frequency $\omega_{\mathbf{k}}$, creation and annihilation operators
$\hat{a}_{\mathbf{k}}^{\dagger}$ and $\hat{a}_{\mathbf{k}}$ and system coupling strength $h_{\mathbf{k}}$. Consider now one component of Ξ_E in
Eq. (2.17) and the trace and time integration of it

$$\int_0^\infty e^{i\epsilon s'} \operatorname{Tr}_E \left\{ h_{\mathbf{k}}^2 e^{i\omega_{\mathbf{k}} s'} \hat{a}_{\mathbf{k}}^\dagger \hat{a}_{\mathbf{k}} \rho_E \right\} ds', \tag{2.19}$$

where we have used the environment operators $\left(\hat{E}_\mu^{(I)} \right)^\dagger (t) = h_{\mathbf{k}} e^{i\omega_{\mathbf{k}} t} \hat{a}_{\mathbf{k}}^\dagger$ and $\hat{E}_\nu^{(I)} (t - s) = h_{\mathbf{k}} e^{-i\omega_{\mathbf{k}}(t-s')} \hat{a}_{\mathbf{k}}$. The exponential in each of these operators originates from their
conversion in to the interaction picture.

For one mode we might know $h_{\mathbf{k}}$, but when dealing with a sum to infinity of all modes in the bath this becomes a daunting prospect. The first step in a process of handling an extended environment, such as we have here, is to define the spectral density (SD)

$$\chi(\omega) = \sum_{\mathbf{k}} h_{\mathbf{k}}^2 \delta(\omega - \omega_{\mathbf{k}}); \tag{2.20}$$

this completely encapsulates the interaction behaviour of the environment in terms of the system interaction energies $h_{\mathbf{k}}$. This discrete expression for the SD allows us to define an identity

$$
\begin{aligned}
\int_0^\infty \chi(\omega)\phi(\omega)\mathrm{d}\omega &= \int_0^\infty \sum_{\mathbf{k}} h_{\mathbf{k}}^2 \delta(\omega - \omega_{\mathbf{k}})\phi(\omega)\mathrm{d}\omega \\
&= \sum_{\mathbf{k}} h_{\mathbf{k}}^2 \int_0^\infty \phi(\omega)\delta(\omega - \omega_{\mathbf{k}})\mathrm{d}\omega \\
&= \sum_{\mathbf{k}} h_{\mathbf{k}}^2 \phi(\omega_{\mathbf{k}}).
\end{aligned}
\tag{2.21}
$$

Equation (2.21) allows conversion of an arbitrary discrete function of bath modes to a continuous description in terms of an SD, suppressing the explicit dependence on system interaction energy.

As is shown in the Chapter 3 derivation, terms of the form in Eq. (2.19) can benefit from the use of this identity in working towards a Lindblad master equation. Now, rather than having to deal with discrete modes, a continuous form of the SD can be specified which captures behaviour of the environment; further details of these forms are presented in Chapter 3. What one finds, when the derivation is completed, is that the decay rate of a particular system process defined by a transition between system eigenstates, is dependent upon the SD sampled at the frequency of the transition. Therefore choosing between different forms of continuous SD affects the frequency dependence of the decay rate.

The continuous form of an SD can be a simple curve, it could contain multiple sharp features and it can contain combinations of both of these structures. The examples in Fig. 2.1 were presented in Ref. [85] and show these different styles of SD well; they were chosen to represent realistic behaviour of a particular light harvesting complex. The two SDs ($J_{\mathrm{CM}}(\omega)$ and $J_{\mathrm{QM}}(\omega)$) are actually low and high frequency

components of the overall SD in the model. Clearly $J_{CM}(\omega)$ (inset) is the low frequency component, exhibiting a smooth profile, whereas $J_{QM}(\omega)$ in the main panel is the high frequency component which exhibits a much more structured nature. The position and strength of the structured peaks in the SD are informed from spectroscopic experiments on the light harvesting complex, that is to say that the particular vibrational mode frequencies of the complex that are susceptible to excitation inform one as to where a strong SD effect is required. The equation of the smooth low frequency term was chosen as it reproduced previously observed behaviour. The discrete, vertical lines on the figure are excitonic transition frequencies that the model used predicts.
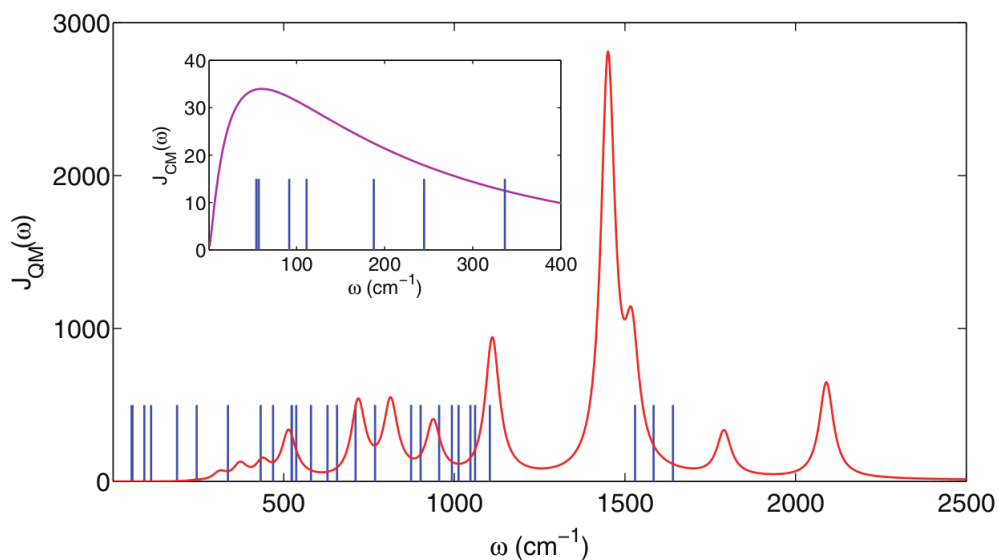
FIGURE 2.1: A two part SD intended to model a particular light harvesting complex with (inset) smooth low frequency and (main) structured high frequency components. The vertical lines in both frames are excitonic transition energies obtained in the particular model for this complex. Figure obtained from Ref. [85].

With a description now that encapsulates the entire bath conveniently, namely χ, we might like a measure of the strength or effectiveness of the bath in terms of its ability to interact with a system. The reorganisation energy is calculated as

$$\lambda = \int_0^\infty \frac{\chi(\omega)}{\omega} d\omega \qquad (2.22)$$

and defines just such a quantity [86]: the energy associated with the displacement of each mode of the bath in response to the dynamics of the system, with a high value

implying more effective dissipation. In the language of our photosynthesis example in Chapter 1, λ would be a measure of the energy available in the protein bath which is used to deform chromophores for instance. Comparisons between different SD forms should fix λ so that even if the SDs are different the total interaction energy of the active bath is the same. This consideration is taken in Chapter 3 where we do indeed compare the effects of different SDs on system dynamics.

2.2.3 Markovianity and methods

Finally in this section on descriptions of environments there remains a word to be said about descriptive nomenclature and other methods of solution. Earlier we made the Markov approximation which can be described as enforcing an environment that has no memory of its interaction with the system; we say this makes the environment Markovian. Even earlier, when we had our comprehensive Liouville-von Neumann equations, our environment-system interaction was defined explicitly and should we have an OQS we can treat analytically in this form our environment would have a full dynamical description; here there would be a memory of information or energy that had flowed into it, this is a non-Markovian environment.

There exists a whole range of OQS techniques along a non-Markovianity spectrum where clearly the ideal solution would balance recollection of the information flow between system and environment behaviour with accuracy and ease of calculation of predictions. We have already introduced master equations [1] but, beyond the weak-coupling approach we have spent considerable time on, there are treatments that introduce some degree of non-Markovianity such as using polaron approximations [87, 88]. Moving past master equations there are also quasi-adiabatic path integrals [89, 90], quantum Monte Carlo techniques [91, 92], hierarchy equations of motion [93], multilayer [94] and multiconfiguration time-dependent Hartree theory [95], time dependent numerical [96] and density matrix [97] renormalisation group approaches, time dependent variational matrix product states [98] and Dirac-Frenkel methods [99, 100]. This is by no means an exhaustive list and some of these techniques can be combined and are constantly being refined or extended to treat more

systems more generally or more efficiently (in terms of computation time or ease). We will be using master equations but introducing some non-Markovianity in Chapter 3 by grouping a single harmonic oscillator in with our qubit system. To improve our investigation in Chapter 4 we will combine a master equation with a matrix product operator solution technique which, while not affecting the Markovianity of our bath, does allow us to extend the dimensionality of the system we can simulate for the realistic nitrogen vacancy based system we consider.

2.3 Matrix product operator formalism

THIS section will introduce the method of matrix product states, and by extension matrix product operators. These are decompositional techniques that can make quantum simulations of (quasi-)1D systems possible on classical computers where traditionally the Hilbert space dimension precludes it. In our context they were first put forward by Vidal in 2003 [101] but had previously been introduced as the ground state of the 1D quantum anti-ferromagnetic Affleck-Kennedy-Lieb-Tasaki (AKLT) model in the late 1980s [102–104] and discussed as an extension to density matrix renormalisation group (DMRG) in the 1990s [105]. We shall shortly describe the decomposition process and subsequently how we evolve such a decomposition in time using the time-evolving block decimation scheme.

2.3.1 The Schmidt and singular value decompositions

Before we can formulate a matrix product state (MPS) we need to be aware of a particularly helpful decomposition one can perform on a bipartite system. The Schmidt decomposition takes any pure bipartite state (where bipartite can mean two parts of different dimension),

$$|\Psi\rangle_{A,B} = \sum_{a,b} C_{a,b} |a_A\rangle |b_B\rangle, \tag{2.23}$$

and expresses it in a diagonal co-basis

$$|\Psi\rangle_{A,B} = \sum_{c} C_c |c_A\rangle |c_B\rangle, \tag{2.24}$$

where $|c_A\rangle$ is an orthonormal basis for part A, $|c_B\rangle$ is an orthonormal basis for part B and the coefficients C are real and non-negative with $\sum_c C_c^2 = 1$ [106]. The $|c_i\rangle$ bases are known as Schmidt bases and the C_c as Schmidt coefficients.

A proof of this decomposition can be shown with the singular value decomposition (SVD). The SVD can be used to transform any complex matrix, into a product of three matrices, one diagonal sandwiched between two unitaries [107]:

$$M = USV^\dagger. \tag{2.25}$$

The dimensionality of the process is shown in Fig. 2.2. The elements of the diagonal S, known as the singular values, are non-negative and are arranged in decreasing size.
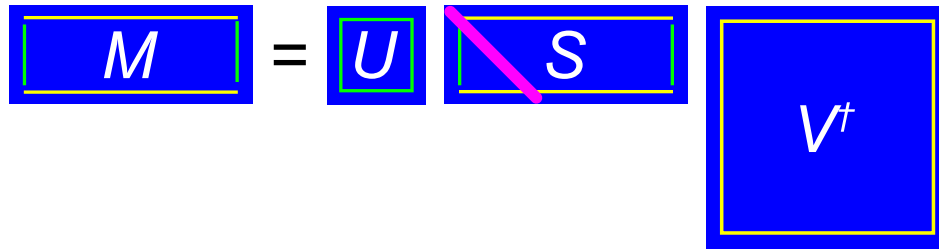
FIGURE 2.2: A diagrammatic representation of the singular value decomposition in Eq. (2.25). Coloured outlines indicate the shared dimensions of the matrices. The pink diagonal line in S denotes the singular values with all off-diagonal elements necessarily equal to zero.

Performing an SVD on the bipartite state coefficients in Eq. (2.23) we can obtain

$$|\Psi\rangle_{A,B} = \sum_{a,b} C_{a,b} |a_A\rangle |b_B\rangle = \sum_{a,b} U_{a,c} S_{c,c} V_{c,b}^\dagger |a_A\rangle |b_B\rangle. \tag{2.26}$$

If we allow the unitaries U and $V^\dagger$ to define new bases for the parts A and B

$$|c_A\rangle = \sum_a U_{a,c} |a_A\rangle \qquad |c_B\rangle = \sum_b V_{c,b}^\dagger |b_B\rangle, \tag{2.27}$$

we can see we have obtained the Schmidt decomposition;

$$|\Psi\rangle_{A,B} = \sum_s S_{c,c} |c_A\rangle |c_B\rangle, \tag{2.28}$$

where $S_{s,s} \equiv C_c$.

One of the nice features of an SVD is that the singular values are ordered, meaning it is easy to locate the smallest ones and it can be shown that a good approximation to the original matrix can be obtained if the smallest of these values are omitted. This trick is used in image compression but it is also useful to us as the scaling of computational resources required for increasing state space sizes is an endemic problem in quantum mechanics. If we look at the form of Eq. (2.28) we can see that truncating S would reduce the number of states we need to keep track of, effectively reducing the complexity of the original $C_{a,b}$ we started with. We will make use of this property in our MPS formulation next.

2.3.2 A matrix product state

With our examples of the SVD and Schmidt decomposition we have already started to show the procedure for obtaining an MPS [101, 106, 108–110] and shown why we might want to. Let us start now with a 1D array of N two level systems (TLSs) and a pure expression of its state in a basis we desire for our computation:

$$|\Psi\rangle = \sum_{\{n_i\}} C_{n_1,n_2,...,n_N} |n_1, n_2, ..., n_N\rangle . \tag{2.29}$$

Computationally it is the 2^N complex coefficients $C_{n_1,n_2,...,n_N}$ (which form an N-th order tensor) we would store and manipulate to perform computations and this clearly scales exponentially with system size. Matrix product formalism seeks to reduce this through an expression of $2N - 1$ lower order tensors.

To proceed we reshape the system to present as bipartite

$$|\Psi\rangle = \sum_{n_1,m} C_{n_1,m} |n_1, m\rangle , \tag{2.30}$$

where m contains all $i > 1$ making our coefficient tensor 2nd order to match our bipartite state. We can perform a Schmidt decomposition on this getting

$$|\Psi\rangle = \sum_{n_1,\nu_1} \Gamma^{[1]n_1}_{\nu_1} \lambda^{[1]}_{\nu_1} |n_1, \phi_{\nu_1}\rangle , \tag{2.31}$$

where $\Gamma^{[1]}$ is the unitary matrix responsible for converting to $|n_1\rangle$ from its Schmidt basis and we represent the singular values as the vector $\lambda_{\nu_1}^{[1]}$; bracketed numerical superscripts are labels. The right part of the partition remains in its Schmidt basis. The index ν_1 is known now as the bond dimension, limiting this would reduce the dimensionality of the problem leading to a more efficient (albeit approximate) solution.

We can now look at the compounded Schmidt state, splitting the second TLS from it (in our preferred basis), leaving behind the remaining right state in a different basis,

$$|\phi_{\nu_1}\rangle = \sum_{n_2} |n_2\rangle |\theta_{\nu_1,n_2}\rangle. \tag{2.32}$$

We can then Schmidt decompose as before and convert the second TLS to our preferred basis

$$|\phi_{\nu_1}\rangle = \sum_{n_2,\nu_2} \Gamma_{\nu_1\nu_2}^{[2]n_2} \lambda_{\nu_2}^{[2]} |n_2\rangle |\phi_{\nu_2}'\rangle \tag{2.33}$$

which we can substitute back in

$$|\Psi\rangle = \sum_{n_1,n_2,\nu_1,\nu_2} \Gamma_{\nu_1}^{[1]n_1} \lambda_{\nu_1}^{[1]} \Gamma_{\nu_1\nu_2}^{[2]n_2} \lambda_{\nu_2}^{[2]} |n_1,n_2,\phi_{\nu_2}'\rangle. \tag{2.34}$$

This process repeats until the entire array has been processed and we obtain

$$|\Psi\rangle = \sum_{\{n_i\},\{\nu_j\}} \Gamma_{\nu_1}^{[1]n_1} \lambda_{\nu_1}^{[1]} \Gamma_{\nu_1\nu_2}^{[2]n_2} \lambda_{\nu_2}^{[2]} \times ... \times \Gamma_{\nu_{N-2}\nu_{N-1}}^{[N-1]n_{N-1}} \lambda_{\nu_{N-1}}^{[N-1]} \Gamma_{\nu_{N-1}}^{[N]n_N} |n_1,n_2,...,n_{N-1},n_N\rangle. \tag{2.35}$$

As we said earlier, the $C_{n_1,n_2,...,n_N}$ in Eq. (2.29) is what a computation would use and now we see

$$C_{n_1,n_2,...,n_N} = \sum_{\{\nu_j\}} \Gamma_{\nu_1}^{[1]n_1} \lambda_{\nu_1}^{[1]} \Gamma_{\nu_1\nu_2}^{[2]n_2} \lambda_{\nu_2}^{[2]} \times ... \times \Gamma_{\nu_{N-2}\nu_{N-1}}^{[N-1]n_{N-1}} \lambda_{\nu_{N-1}}^{[N-1]} \Gamma_{\nu_{N-1}}^{[N]n_N} \tag{2.36}$$

is the MPS formulation with the interpretation that $\Gamma^{[i]}$ is a unitary converting the Schmidt basis of TLS i to our preferred basis and $\lambda^{[i]}$ are both the Schmidt coefficients between sites i and $i+1$ and the singular values between $\Gamma^{[i]}$ and $\Gamma^{[i+1]}$. If the sum runs over all of each of the ν_j then the MPS and explicit N-th rank tensor forms are equivalent. The scaling of an exact $C_{n_1,n_2,...,n_N}$ for large systems is computationally

infeasible, but if we now truncate the bond dimension ν_j at the J-th entry we can obtain an approximate representation of our state that no longer has scaling 2^N but instead about $(2J^2 + J)N$.

2.3.3 Expressing density matrices

Of course, as we wish to apply matrix product formalism to master equations we need a description of density matrices rather than state vectors. Direct substitution would give us

$$
\begin{aligned}
\rho &= \sum_{\{n_i\},\{n_j'\}} D_{n_1,n_2,...,n_N,n_1',...,n_N'} \, |n_1, n_2, ..., n_N\rangle \, \langle n_1', n_2', ..., n_N'| \\
&= \sum_{\{n_i\},\{\nu_j\}\{n_{i'}'\},\{\nu_{j'}'\}} \left(\Gamma_{\nu_1}^{[1]n_1} \lambda_{\nu_1}^{[1]} ... \right) \left(\Gamma_{\nu_1'}^{[1]n_1'} \lambda_{\nu_1'}^{[1]} ... \right) |n_1, ..., n_N\rangle \, \langle n_1', ..., n_N'| \, .
\end{aligned}
\tag{2.37}
$$

This picture of the density matrix is a bit of an unwieldy expression, but there are ways of simplifying it using a purification method [108, 111] or an operator basis expansion [106, 112]. We will introduce our use of the latter shortly.

The density matrix of a TLS can be described completely using the Pauli spin matrices as a basis

$$
\rho = \sum_i p_i \hat{\sigma}^i = A\hat{\sigma}^I + B\hat{\sigma}^X + C\hat{\sigma}^Y + D\hat{\sigma}^Z = \begin{pmatrix} A + D & B - iC \\ B + iC & A - D \end{pmatrix}.
\tag{2.38}
$$

This basis can be thought of as a vector and we can portray this as $|\rho\rangle = \sum_j p_j |\sigma^j\rangle$. Writing an expression for our 1D array of N TLSs in a Pauli basis vector form

$$
|\rho\rangle = \sum_{\{s_i\}} p_{s_1,s_2,...} |\sigma^{s_1}\sigma^{s_2}...\sigma^{s_N}\rangle
\tag{2.39}
$$

there is a clear similarity with Eq. (2.29) where now we have a vector of Pauli matrices on TLS s_i where before we had states labelled n_i.

We can proceed along the SVD based procedure to decompose our density matrix

$$p_{s_1,s_2,\ldots,s_N} = \sum_{\{\nu_j\}} \Gamma^{[1]s_1}_{\nu_1} \lambda^{[1]}_{\nu_1} \Gamma^{[2]s_2}_{\nu_1 \nu_2} \lambda^{[2]}_{\nu_2} \times \ldots \times \Gamma^{[N-1]s_{N-1}}_{\nu_{N-2}\nu_{N-1}} \lambda^{[N-1]}_{\nu_{N-1}} \Gamma^{[N]s_N}_{\nu_{N-1}} \tag{2.40}$$

where the number of coefficients is increased by the power of two due to the move from state vector to density matrix. This is now in a matrix product operator (MPO) form. The bond dimension truncation trick can still be used to great effect allowing us to reduce system complexity to enhance numerical simulation. The degree to which we can truncate our system and produce accurate solutions depends on the extent or amount of entanglement with more extensive entanglement requiring a larger bond dimension.

2.3.4 The Suzuki-Trotter expansion

Before we get on to exactly what 'numerical simulation' implies for an MPO we should introduce a helpful mathematical operation. In dealing with time evolving unitary operators we often come across exponentiated operators of the form

$$\mathrm{e}^{(A+B)t} \tag{2.41}$$

where the matrices A and B are typically some Hamiltonian components and do not necessarily commute. Mathematical application of this operator necessitates diagonalisation of the exponent and this can be difficult so we wish to split the exponent into smaller chunks to simplify its application.

The Suzuki-Trotter expansion is a way of approximating the exponent that does provide us with simplified exponents. There is a first order variant [113]

$$\mathrm{e}^{(A+B)t} = \mathrm{e}^{At}\mathrm{e}^{Bt} + O(t^2), \tag{2.42}$$

which can be simply extended to higher orders [114]. We use here the second order variant

$$\mathrm{e}^{(A+B)t} = \exp\left(\frac{At}{2}\right) \exp(Bt) \exp\left(\frac{At}{2}\right) + O(t^3). \tag{2.43}$$

If we were to discretise the arbitrary time t into T smaller steps then we could write [115]

$$\left(\exp\left(\frac{(A+B)t}{T}\right)\right)^T = \left(\exp\left(\frac{At}{2T}\right)\exp\left(\frac{Bt}{T}\right)\exp\left(\frac{At}{2T}\right)\right)^T + O\left(\frac{t^3}{T^2}\right) \quad (2.44)$$

and clearly see the expansion is exact in the limit $T \to \infty$.

2.3.5 Time-evolving block decimation

We can now present the time-evolving block decimation scheme (TEBD). In general the TEBD is a prescription for applying time evolution operations to a 1D matrix product decomposed state (where state could be an MPS vector as Eq (2.36) [116] or an MPO density matrix as Eq (2.40) [112]). Moving forward we shall describe the process in terms of MPOs undergoing dissipative evolution via a Lindblad master equation of diagonal form,

$$\dot{\rho}_{\rm S}(t) = -i\left[\hat{H}, \rho_{\rm S}(t)\right] + \sum_\mu \Upsilon_\mu \left(2\hat{L}_\mu \rho_{\rm S}(t)\hat{L}_\mu^\dagger - \left\{\hat{L}_\mu^\dagger \hat{L}_\mu, \rho_{\rm S}(t)\right\}\right). \quad (2.45)$$

As shown earlier, Eq. (2.45) formally has the solution $\rho_{\rm S}(t) = \exp\left[\mathcal{L}t\right]\rho_{\rm S}(0)$ where $\mathcal{L}$ is the superoperator comprising the terms on the right hand side which act on the reduced density matrix from the left and right. Our MPO form for $\rho_{\rm S}$ is however vectorised so we require an expression for $\mathcal{L}$ where the operators act only from the left. This is further complicated by the fact that we have not performed the simplest vectorisation (transplanting column by column [117]) but rather expanded in a basis. We need a conversion such that for any $\hat{o}\rho = \sum_{ij} o_{ij} |i\rangle\langle j|$ or $\rho\hat{o} = \sum_{ij} |i\rangle\langle j| o_{ij}$ in operator form we have a suitable superoperator form $\hat{O}' |\rho'\rangle = \sum_{ij} O'_{ij} |\rho'_j\rangle$ where we have written the vectorised basis $|\rho'\rangle$ of the form in Eq. (2.39). In the subsequent discussion we shall stick with a Pauli matrix based description, but the method extends to three level systems using the Gell-Mann basis [118] and our method in Chapter 3 relies on an extension to four level systems [119].

Taking a step back, changing the basis of a traditional matrix operator $\hat{o}$, to some orthonormal vector basis $\{|i\rangle\}$ can be done simply with $\hat{o}'_{ij} = \langle i|\hat{o}|j\rangle$. The process of

converting to a superoperator in a vectorised Hermitian matrix basis $\{\hat{\sigma}^i\}$ follows the similar procedure $O_{ij} = \text{Tr}\left[\hat{\sigma}^i\hat{o}\hat{\sigma}^j\right]$. Let us illustrate this for the operation $\hat{o}\rho$ using the Pauli basis $\{\hat{\sigma}^I, \hat{\sigma}^X, \hat{\sigma}^Y, \hat{\sigma}^Z\}$ and with the basis expression $|\rho\rangle = \sum_i p_i |\hat{\sigma}^i\rangle$. Firstly if we define $\hat{o}\rho = \rho' \equiv |\rho'\rangle = \hat{O}|\rho\rangle = \sum_i q_i |\hat{\sigma}^i\rangle$ as the action of the operator (mixing representations some what) and recall the Pauli basis property $\text{Tr}\left[\hat{\sigma}^i\hat{\sigma}^j\right] = 2\delta_{ij}$, we see

$$\frac{1}{2}\text{Tr}\left[\hat{\sigma}^i\rho'\right] = \frac{1}{2}\text{Tr}\left[\sum_j q_j\hat{\sigma}^i\hat{\sigma}^j\right] = \sum_j q_j\delta_{ij} = q_i. \tag{2.46}$$

Making an explicit substitution for the operation now

$$q_i = \frac{1}{2}\text{Tr}\left[\hat{\sigma}^i\hat{o}\rho\right] = \frac{1}{2}\sum_j p_j \text{Tr}\left[\hat{\sigma}^i\hat{O}\hat{\sigma}^j\right] = \frac{1}{2}\sum_j p_j O_{ij}, \tag{2.47}$$

we can appreciate the value q_i as an element in the resulting vectorised density matrix calculated as a sum of each old element multiplied by the corresponding element from the row in superoperator $\hat{O}$.

This method then leads to four conversions

$$\hat{o}\rho \rightarrow O_{ij} = \text{Tr}\left[\hat{\sigma}^i\hat{o}\hat{\sigma}^j\right] \tag{2.48}$$

$$\rho\hat{o} \rightarrow (O_{ij})^{\mathsf{T}} \tag{2.49}$$

$$\hat{o}^\dagger\rho \rightarrow (O_{ij})^\dagger \tag{2.50}$$

$$\rho\hat{o}^\dagger \rightarrow (O_{ij})^*. \tag{2.51}$$

For example take $\hat{o} = \hat{\sigma}^X$, if we calculate all of the 16 elements $\Sigma^X_{ij} = \text{Tr}\left[\hat{\sigma}^i\hat{\sigma}^X\hat{\sigma}^j\right]$ (as i and j each contain the four Pauli basis members)

$$\hat{\Sigma}^X = \begin{pmatrix} 0 & 1 & 0 & 0 \\ 1 & 0 & 0 & 0 \\ 0 & 0 & 0 & -i \\ 0 & 0 & i & 0 \end{pmatrix}. \tag{2.52}$$

If we perform $\hat{\Sigma}^X |\rho\rangle$ we obtain the same result as $\hat{\sigma}^X\rho$.

Now we have the ability to construct our Liouvillian from Eq. (2.45) in a linear superoperator form

$$\mathcal{L} = -i\left(\hat{H} - \hat{H}^{\mathsf{T}}\right) + \sum_{\mu} \Upsilon_{\mu}\left(2\hat{L}_{\mu}\hat{L}_{\mu}^{*} - \hat{L}_{\mu}^{\dagger}\hat{L}_{\mu} - \left(\hat{L}_{\mu}^{\dagger}\hat{L}_{\mu}\right)^{\mathsf{T}}\right), \qquad (2.53)$$

where all operators are now their superoperator versions. Our formal solution could now be implemented as $|\rho_{\mathrm{S}}(t)\rangle = \exp[\mathcal{L}t]\,|\rho_{\mathrm{S}}(0)\rangle$ but we need to understand how to apply the time evolution operator to our MPO density matrix.

A first step would be to see that computationally it makes more sense to write $|\rho_{\mathrm{S}}(t + \delta t)\rangle = \exp[\mathcal{L}\delta t]\,|\rho_{\mathrm{S}}(t)\rangle$ when we want to see dynamics. This highlights that we only have to define $\hat{T} = \exp[\mathcal{L}\delta t]$ initially, however this operator is still only defined as a large matrix and application of it could be difficult. To proceed we impose that our 1D array system interacts only via nearest neighbour interactions so our Liouvillian consists of terms acting on an individual TLS and between neighbouring sites. With this in mind we obtain a splitting of $\mathcal{L} = \mathcal{L}^{E} + \mathcal{L}^{O}$ with superscripts denoting even and odd neighbour-bonds if we think of $\mathcal{L} = \sum_{i} \mathcal{L}_{i}$, a sum over site-pairs; this is sketched in Fig. 2.3. Going a step further we can see $\mathcal{L}^{k} = \sum_{i} \mathcal{L}_{i}^{k}$ for $k \in \{E, O\}$ where generally $[\mathcal{L}_{i}^{E}, \mathcal{L}_{j}^{O}] \neq 0$ but $[\mathcal{L}_{i}^{k}, \mathcal{L}_{j}^{k}] = 0$.
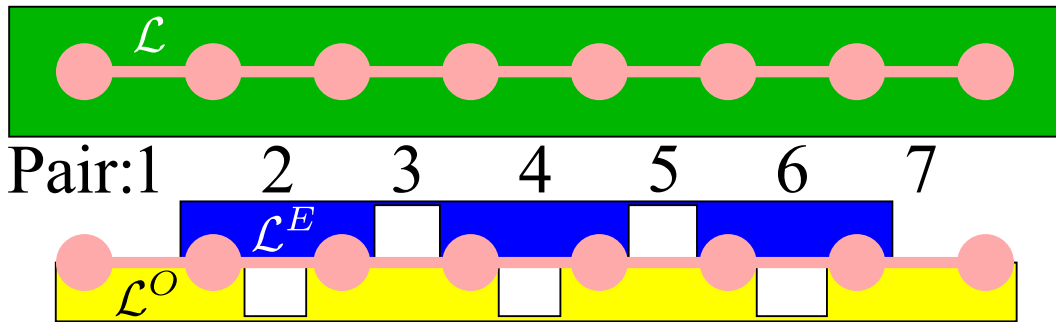

FIGURE 2.3: An illustration of how the Liouvillian components contain the even and odd pair-bonded neighbours in a 1D TLS array. An exponentiated time evolution with this composite Liouvillian can then be Trotter-Suzuki exapanded to aid computation.

So employing a Trotter-Suzuki expansion on our time evolution operator with our odd-even Liouvillians we get

$$
\begin{aligned}
\hat{T} &= \exp\left(\frac{\mathcal{L}^O \delta t}{2}\right) \exp\left(\mathcal{L}^E \delta t\right) \exp\left(\frac{\mathcal{L}^O \delta t}{2}\right) \\
&= \prod_{ijk} \exp\left(\frac{\mathcal{L}_i^O \delta t}{2}\right) \exp\left(\mathcal{L}_j^E \delta t\right) \exp\left(\frac{\mathcal{L}_k^O \delta t}{2}\right).
\end{aligned} \tag{2.54}
$$

where we have made use of the previously mentioned intra-component commutation. Computationally the operation of each group of odd or even exponentials in Eq. (2.54) can be done in parallel allowing much improved computation time.

The exponentials in Eq. (2.54) as described are, based on our discussion of $\mathcal{L}$ so far, matrices which operate on a vector (understood to be in the Pauli basis). Technically though our vector is described in an MPS form and as such our operator $\hat{T}$ needs to be in an appropriate form for operation. Each matrix $\hat{T}_i^E = \exp\left[\mathcal{L}_i^E \delta t\right]$ and $\hat{T}_i^O = \exp\left[\mathcal{L}_i^O \delta t/2\right]$ acting on a pair of TLS sites can undergo an SVD to be brought into an MPO form which can act on our $|\rho(t)\rangle$ via tensor contraction. The TEBD proceeds with the application of the components of $\hat{T}$ followed by a refresh of the MPO decomposition of the state and this is repeated successively until some final time [112, 116]. Any errors due to the truncation of the bond dimension and size of the Trotter-Suzuki step are minimised through convergence testing.

2.4   Simulations

NOWING now how a simulation can be carried out, allowing us to evolve a reduced system density matrix in time we must ask the question what do we want to infer from such dynamics? Shortly we will mention the two measures we use to make conclusions about our dynamical simulations, but first a note on what goes in to a simulation.

All density matrix dynamics in this thesis have been obtained numerically using computer code developed in Fortran or Python, with some parallelisation in place where it would enhance computation time. Numerical solution of master equations

requires discretised time solutions and the degree of discretisation (the size of time steps) must be ensured to be small enough that the observed behaviours do not appreciably depend on it. Such convergence can only be obtained through repeated simulations at smaller time steps to find the most efficient value that balances simulation accuracy and efficiency. Further, in Chapter 3 we truncate a bosonic mode and convergence must also be found such that we can be satisfied that including more bosonic levels would not have an effect on the dynamics. Finally, as we mentioned a moment ago, bond dimension of our MPO formulation is also a parameter that must be refined through convergence of the dynamics. The values at which these parameters result in converged dynamics have an interdependence and also a dependence on the parameter regime of the system; traditionally strongly coupled or rapidly fluctuating systems require smaller time steps for instance.

2.4.1 Probability

In order to converge a simulation one must be producing a 'measurement' value to characterise the dynamics. An obvious value that can be obtained from a density matrix is the probability of a particular state. Having an awareness of the basis being simulated allows us to extract a diagonal value from a ρ and infer what the probability of occupation of a basis state would be. Probability is the measurement used in Chapter 3 to provide us insight into the oscillatory state dynamics between the two sites in a dimer.

2.4.2 Entanglement of formation

In Chapters 4 and 5 we wish to assess the degree to which entanglement with an ancilla has been transferred from a nearby sender to a distant receiver and for this we need a suitable measure of entanglement. There exist numerous bipartite entanglement measures [120, 121] including distillable entanglement, entanglement cost, entanglement of formation and the relative entropy of entanglement. We chose the entanglement of formation [122] for our measure as it is a simple to calculate entanglement monotone in the range 0 (for a perfectly disentangled state) to 1 (for a maximally

entangled Bell state). Given a bipartite system of two spin-1/2 particles described by ρ, the entanglement of formation between the spins is calculated using

$$E(\rho) = h\left(\frac{1 + \sqrt{1 - C(\rho)^2}}{2}\right),$$ (2.55)

where

$$h(\theta) = \theta \log_2 \theta - (1 - \theta) \log_2 (1 - \theta)$$ (2.56)

is the binary entropy function and $C(\rho) = \max(0, \lambda_1 - \lambda_2 - \lambda_3 - \lambda_4)$ is the concurrence. This is calculated using the descending-ordered eigenvalues of $\sqrt{\rho\tilde{\rho}}$ where $\tilde{\rho} = (\sigma^y \otimes \sigma^y)\, \rho^*\, (\sigma^y \otimes \sigma^y)$. The entanglement of formation can be interpreted as the number of Bell states required to produce the given state, hence the bounding cases of 0 and 1; no two particle state can be more entangled than a Bell pair.

2.4.3 Unit conversion

These measures of probability and entanglement are somewhat abstract and a reference point can often be helpful, whether this is the time scale of the dynamics or the strength of coupling in a system. As a final point in this theory section we present a review of how the use of frequency units for energy is obtained, as it is used throughout this thesis (and in some associated literature).

We start with the formula for photon energy $E = hf = hc/\lambda$ with everything in SI units and where the symbols have their traditional meanings. If we want to now describe energy in meV and have a wavelength in cm^{-1} then the equation becomes

$$E = \frac{hc}{10^5 e\lambda}.$$ (2.57)

The unit of cm^{-1} is another common energy unit and using Eq. (2.57) we can say that $1\,\text{meV} = e/10^5 ch\ \text{cm}^{-1} \approx 8\ \text{cm}^{-1}$ or $1\,\text{cm}^{-1} = 10^5 ch/e\ \text{meV} \approx 0.12\ \text{meV}$.

If we take the dispersion relation for EM waves in a vacuum $\omega = ck = 2\pi c/\lambda$ and again choose wavelength in cm^{-1} and angular frequency in THz we get

$$\omega = \frac{2\pi c}{10^{10}\lambda}.$$ (2.58)

This gives $1\,\mathrm{THz} \approx 5.3\,\mathrm{cm}^{-1}$ or $1\,\mathrm{cm}^{-1} \approx 0.19\,\mathrm{THz}$. Combining our conversions gives $1\,\mathrm{THz} = 10^{15}h/2\pi e$ meV≈ 0.66 meV and $1\,\mathrm{meV} = 2\pi e/10^{15}h$ THz≈ 1.52 THz.

3

Maintenance of coherent dynamics in a dissipative environment

THIS chapter will be concerned with an investigation into the coherent dynamics of a particular toy model interacting with a Markovian environment and how the structure of that environment plays an important role. Since there is still a great deal we can learn about open quantum systems (OQSs) we can still gain insight by considering simple models. We will include a non-Markovian element in our model by incorporating some of the environment within the OQS allowing us to consider systems where part of the environment couples strongly. Our system comprises a two site system, or dimer, in which we are principally interested, and a single oscillatory mode (SM). The environment considered is bosonic, Markovian and weakly coupled to the OQS.

Examples of real physical problems this maps to include photosynthetic complexes [85], which we introduced in Sec. 1.2.1, and superconducting qubits coupled to both microwave [123] and nanomechanical [124] resonators (see Fig. 3.1 for some images of experimental set-ups). To reiterate, our model would be suitable for describing a two site chromophore strongly interacting with one protein mode and weakly interacting with the wider protein environment. The idea of a superconducting qubit experiment in which it is strongly coupled to a single mode of an adjacent resonator is also a good fit to this model where the other resonator modes are weakly coupled and form the bath.

Studies concerning coupled, structured environments, where a particular feature
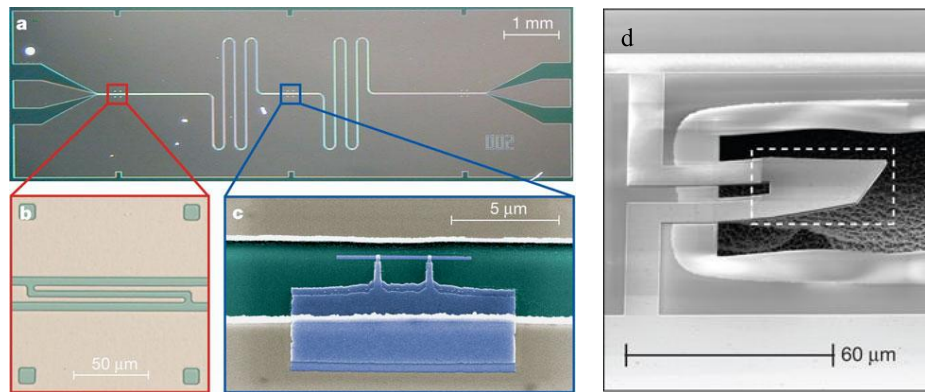
FIGURE 3.1: a-c) From Ref. [123] showing (a) their cavity QED circuit with (c) superconducting qubit in the centre. b) Capacitive coupling between resonator and input-output feed line. d) A quantum mechanical resonator taken from and presented in Ref. [124].

has been represented as a SM, have previously been carried out [125–129], and the complexity of systems with such descriptions has been reduced through symmetry exploitations [130, 131]. Our chosen system configuration is, however, not represented by these works; in them the SM and bath are either not distinguished or are coupled directly (which is not our intention). For example in Ref. [126], a system, consisting of a symmetric dimer coupled to a bosonic environment, is reformulated as a symmetric dimer coupled to a single bosonic mode which in turn couples to a bosonic environment. The results obtained in their study of this dissipative system are restricted to low temperatures due to the truncation imposed in their treatment of the single mode. The use of low temperature truncations is common and was also used in Refs. [130] and [131]; herein a symmetric dimer is coupled to multiple oscillator modes but their analytic approach requires them to be truncated to two levels.

One study that did use a SM demonstrated that the coherence of the dynamics in an asymmetric, excitonic dimer was enhanced by it; here (unlike in our approach) each site of the dimer was coupled to its own Markovian bath [132]. In contrast to our work, a polaron transform was employed to approximate the non-Markovian aspects of their model. Finally we find examples of dimer models with asymmetric site energies used to investigate the vibrational protein networks of photosynthetic systems and their coherent or non-classical electronic properties [13, 133]

3.1 The model

$\mathbb{W}$E chose to investigate the system of a symmetric dimer coupled to a bosonic SM and a dissipative bosonic environment. The levels of the SM will not be truncated in a way which can preclude validity in high temperature regimes and its frequency will be off-resonant with the transition frequency of the dimer. A weak coupling master equation will be derived and used to investigate the effects of different forms of the environmental spectral density (SD) on the coherent system dynamics.
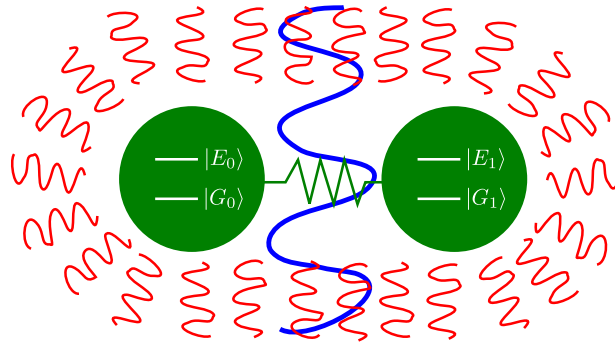

FIGURE 3.2: A schematic diagram of the model given in Eq. (3.1). The symmetric dimer is composed of two identical sites with a dipole-dipole interaction between them (green). This is linearly coupled to a Markovian bosonic environment of oscillators (red). One bosonic mode of the environment (blue) is assumed to be much more strongly coupled to the dimer than the others, and is therefore considered as part of the system that must be treated exactly.

Our dimer is made up of two sites, defined as '0' and '1'; they are identical and both have an electronic ground state, $|G\rangle$, and a state $|E\rangle$ which corresponds to a single excitation, an exciton. The Hamiltonian describing this, the SM and the environment can be expressed as

$$H_{\text{Full}} = H_{\text{D}} + H_{\text{SM}} + H_{\text{D-SM}} + H_{\text{B}} + H_{\text{D-B}} \qquad (3.1)$$

and is shown schematically in Fig. 3.2. The dimer term describing its electronic features is

$$H_{\text{D}} = \varepsilon \left(|E_0\rangle \langle E_0| + |E_1\rangle \langle E_1| \right) - J(|E_0 G_1\rangle \langle G_0 E_1| + \text{H.c}), \qquad (3.2)$$

where each site has excitation energy ε and a dipole-dipole interaction energy of J. The vibrational SM is included through the terms

$$H_{\text{SM}} = \Omega \hat{a}^\dagger \hat{a}, \tag{3.3}$$

$$H_{\text{D-SM}} = -\left(g_0 \left|E_0\right\rangle \left\langle E_0\right| + g_1 \left|E_1\right\rangle \left\langle E_1\right|\right)\left(\hat{a}^\dagger + \hat{a}\right), \tag{3.4}$$

where the SM frequency is Ω, has annihilation and creation operators $\hat{a}$ and $\hat{a}^\dagger$ and the coupling strength to each site of the dimer is $g_0 = -g_1 = g$. Finally, the environment is incorporated with the terms

$$H_{\text{B}} = \sum_{\mathbf{q}} \omega_{\mathbf{q}} \hat{b}_{\mathbf{q}}^\dagger \hat{b}_{\mathbf{q}}, \tag{3.5}$$

$$H_{\text{D-B}} = -\sum_{\mathbf{q}} \left(h_{\mathbf{q},0} \left|E_0\right\rangle \left\langle E_0\right| + h_{\mathbf{q},1} \left|E_1\right\rangle \left\langle E_1\right|\right)\left(\hat{b}_{\mathbf{q}}^\dagger + \hat{b}_{\mathbf{q}}\right), \tag{3.6}$$

which describe harmonic modes with wave vector $\mathbf{q}$, frequencies $\omega_{\mathbf{q}}$, annihilation and creation operators $\hat{b}_{\mathbf{q}}$ and $\hat{b}_{\mathbf{q}}^\dagger$ and dimer site coupling strengths $h_{\mathbf{q},0} = -h_{\mathbf{q},1} = h_{\mathbf{q}}$. In the site basis, the bath and SM couplings to the dimer are linear in displacement.

Three subspaces span the Hamiltonian of Eq. (3.1) and their basis vectors are $\{\left|G_0, G_1\right\rangle\}$, $\{\left|E_0, E_1\right\rangle\}$ and $\{\left|E_0, G_1\right\rangle, \left|G_0, E_1\right\rangle\}$. These subspaces are uncoupled from each other and therefore restricting ourselves to the last, the single excitation subspace, is perfectly reasonable if we wish to study the dynamics of population transfer. A definition which suitably simplifies proceedings has $\left|0\right\rangle = \left|E_0, G_1\right\rangle$ and $\left|1\right\rangle = \left|G_0, E_1\right\rangle$.

We can now consider our Hamiltonian in this reduced two dimensional subspace:

$$H_{\text{F}} = -J\hat{X} - \hat{Z}g(\hat{a}^\dagger + \hat{a}) - \hat{Z}\sum_{\mathbf{q}} h_{\mathbf{q}}(\hat{b}_{\mathbf{q}}^\dagger + \hat{b}_{\mathbf{q}}) + \Omega\hat{n} + \sum_{\mathbf{q}} \omega_{\mathbf{q}}\hat{n}_{\mathbf{q}}. \tag{3.7}$$

The Hamiltonian H_{F} comprises a single two level system (TLS) description of the dimer, where the levels correspond to the presence of an excitation on either of the original dimer sites. Included now are the Pauli operators in the site-basis $\hat{Z} = \left|0\right\rangle \left\langle 0\right| - \left|1\right\rangle \left\langle 1\right|$ and $\hat{X} = \left|0\right\rangle \left\langle 1\right| + \left|1\right\rangle \left\langle 0\right|$ and the SM and $\mathbf{q}$-th bath mode number

operators $\hat{n} = \hat{a}^\dagger \hat{a}$ and $\hat{n}_{\mathbf{q}} = \hat{b}_{\mathbf{q}}^\dagger \hat{b}_{\mathbf{q}}$. The form of Eq. (3.7) is a modified spin-boson model Hamiltonian. Despite only being exactly solvable in certain special circumstances, the spin-boson model has been widely investigated and employed to aid in studies of OQS properties [44, 134–138]. The model is typically comprised of a two level 'spin' interacting with a bath of harmonic bosons; our modification is the inclusion of the SM, which we group with the TLS into our 'system' which will receive an exact treatment.

3.1.1 The Fulton-Gouterman transformation

If we focus on the TLS-SM system and disregard the environment for the moment, Eq (3.7) can be written as

$$H = -J\hat{X} - \hat{Z}g(\hat{a}^\dagger + \hat{a}) + \Omega\hat{n}, \tag{3.8}$$

which is diagonalisable in the TLS subspace using the Fulton-Gouterman transformation (FGT). Posited in 1961 [139] as a subspace diagonalisation tool for vibronic-electronic problems (such as molecular dimers) where the electronic element had a two level structure, it was later extended to N level electronic systems [140] and refined to display an exponential form [141]. The transform is unitary and the form used here is [142, 143]

$$U = \frac{1}{\sqrt{2}}\left[|0\rangle\langle 0| - |1\rangle\langle 0| + \hat{P}\big(|0\rangle\langle 1| + |1\rangle\langle 1|\big)\right], \tag{3.9}$$

although others do exist in the literature [130, 144]. The parity operator, $\hat{P} = (-1)^{\hat{n}}$, operates in the SM subspace and obeys the anti-commutation relations

$$\{\hat{P}, \hat{a}\} = \{\hat{P}, \hat{a}^\dagger\} = 0. \tag{3.10}$$

The action of the FGT is to separate states of like excitation parity into two uncoupled Hamiltonians. If we transform Eq. (3.8) into the superposition basis, $|\pm\rangle =$

$\frac{1}{\sqrt{2}}(|0\rangle \pm |1\rangle)$, (still describing the SM in Fock states) and display the matrix form,

$$
\underline{\underline{\mathbf{H}}} = \begin{array}{c} \\ \langle +0| \\ \langle -0| \\ \langle +1| \\ \langle -1| \\ \vdots \end{array} \begin{array}{c} |+0\rangle \quad |-0\rangle \quad |+1\rangle \quad |-1\rangle \quad \cdots \\ \begin{pmatrix} -J & 0 & 0 & -g & \cdots \\ 0 & J & -g & 0 & \cdots \\ 0 & -g & -J+\Omega & 0 & \cdots \\ -g & 0 & 0 & J+\Omega & \cdots \\ \vdots & \vdots & \vdots & \vdots & \ddots \end{pmatrix} \end{array},
\tag{3.11}
$$

we can see a pattern between which states are coupled. The system states where the excitations present are of even ($|+0\rangle, |-1\rangle, \dots$) or odd ($|-0\rangle, |+1\rangle, \dots$) parity only link with same-parity states, allowing us to isolate

$$
\underline{\underline{\mathbf{H}}}^+ = \begin{array}{c} \\ \langle +0| \\ \langle -1| \\ \vdots \end{array} \begin{array}{c} |+0\rangle \quad |-1\rangle \quad \cdots \\ \begin{pmatrix} -J & -g & \cdots \\ -g & J+\Omega & \cdots \\ \vdots & \vdots & \ddots \end{pmatrix} \end{array}, \quad \underline{\underline{\mathbf{H}}}^- = \begin{array}{c} \\ \langle -0| \\ \langle +1| \\ \vdots \end{array} \begin{array}{c} |-0\rangle \quad |+1\rangle \quad \cdots \\ \begin{pmatrix} J & -g & \cdots \\ -g & -J+\Omega & \cdots \\ \vdots & \vdots & \ddots \end{pmatrix} \end{array}.
\tag{3.12}
$$

If we apply the transform to our Eq. (3.8) Hamiltonian we obtain

$$
\tilde{H} = UHU^\dagger = \frac{H^+}{2} |0\rangle \langle 0| + \frac{H^-}{2} |1\rangle \langle 1|,
\tag{3.13}
$$

with

$$
H^\pm = \Omega \hat{n} - g(\hat{a}^\dagger + \hat{a}) \mp J\hat{P}.
\tag{3.14}
$$

The parity conserving subspace Hamiltonians are the same as those in matrix form earlier, hence the FGT is equivalent to a basis rotation and a rearranging of states. It should also be noted that $H^\pm$ are both tridiagonal in matrix form which affords efficient numerical diagonalisation. The eigenstates of the transformed Hamiltonian $\tilde{H}$ are

$$
|\psi_k^\pm\rangle = \frac{1}{\sqrt{2}} \left[\pm |0\rangle + \hat{P} |1\rangle \right] |\phi_k^\pm\rangle,
\tag{3.15}
$$

where we have made a site basis expansion. So for clarity then the Schrödinger equations here are $H^\pm |\phi_k^\pm\rangle = E_k^\pm |\phi_k^\pm\rangle$ and $\tilde{H} |\psi_k^\pm\rangle = E_k^\pm |\psi_k^\pm\rangle$.

3.1.2   Add the bath

Moving to a superposition basis representation of the TLS, $\{|\pm\rangle\}$, Eq. (3.8) is now

$$H_{\mathrm{S}} = -J\hat{\sigma}_z - \hat{\sigma}_x g(\hat{a}^\dagger + \hat{a}) + \Omega\hat{n} \tag{3.16}$$

where the 'S' subscript is being used to indicate the TLS-SM 'system'. The basis rotation means our new Pauli spin matrices are $\hat{\sigma}_z = |+\rangle\langle+| - |-\rangle\langle-|$ and $\hat{\sigma}_x = |+\rangle\langle-| + |-\rangle\langle+|$. So bringing the bath back, our full Hamiltonian including system, bath and interaction parts is

$$H_{\mathrm{F}} = H_{\mathrm{S}} + \sum_{\mathbf{q}} \omega_{\mathbf{q}} \hat{n}_{\mathbf{q}} + \hat{\sigma}_x \sum_{\mathbf{q}} h_{\mathbf{q}} \big(\hat{b}_{\mathbf{q}}^\dagger + \hat{b}_{\mathbf{q}} \big), \tag{3.17}$$

from which we can derive a Markovian master equation that assumes the oscillator environment only couples weakly to the TLS-SM system.

3.2   Derived master equation

As was introduced in detail in Chapter 2, a master equation can be used to describe the dynamics of an OQS, with a general Born-Markov, interaction picture form of

$$\frac{\mathrm{d}\rho_{\mathrm{S}}(t)}{\mathrm{d}t} = -\int_0^\infty \mathrm{d}s \, \mathrm{Tr}_B \Big[H_{\mathrm{I}}(t), \big[H_{\mathrm{I}}(t-s), \rho_{\mathrm{S}}(t) \otimes \rho_{\mathrm{B}} \big] \Big]. \tag{3.18}$$

The reduced system density matrix, $\rho_S(t)$, has its dynamics described with respect to the stationary thermal bath density matrix, ρ_{B} and the interaction Hamiltonian in the interaction picture, $H_{\mathrm{I}}(t)$. We will now proceed with a derivation specific to the way our model has been formulated above, exploiting the form of our H_S eigenstates following the FGT.

3.2.1 The interaction picture

Through a unitary operator method the interaction picture version of the interaction is found with

$$H_{\mathrm{I}}(t) = \mathrm{e}^{\imath(H_{\mathrm{S}}+H_{\mathrm{B}})t} H_{\mathrm{I}} \mathrm{e}^{-\imath(H_{\mathrm{S}}+H_{\mathrm{B}})t}, \tag{3.19}$$

where $H_{\mathrm{I}} = \hat{\sigma}_x \sum_{\mathbf{q}} h_{\mathbf{q}}(\hat{b}_{\mathbf{q}}^{\dagger} + \hat{b}_{\mathbf{q}})$ and $H_{\mathrm{B}} = \sum_{\mathbf{q}} \omega_{\mathbf{q}} \hat{n}_{\mathbf{q}}$ from Eq. (3.17) and H_{S} is as Eq. (3.16). The form of H_{I} is separable in its bath and system components and as $[H_{\mathrm{S}}, H_{\mathrm{B}}] = 0$ we can write a separated version of Eq. (3.19)

$$H_{\mathrm{I}}(t) = \mathrm{e}^{\imath H_{\mathrm{S}}t} \hat{\sigma}_x \mathrm{e}^{-\imath H_{\mathrm{S}}t} \otimes \mathrm{e}^{\imath H_{\mathrm{B}}t} \sum_{\mathbf{q}} h_{\mathbf{q}}(\hat{b}_{\mathbf{q}}^{\dagger} + \hat{b}_{\mathbf{q}}) \mathrm{e}^{-\imath H_{\mathrm{B}}t}. \tag{3.20}$$

It is at this stage we wish to make use of $\{|\psi_k^{\pm}\rangle\}$, the FGT eigenstates of H_{S}. Using them as a basis in which to express $\hat{\sigma}_x$ means the exponential terms encasing it in Eq. (3.20) will now compute as eigenvalues, thus simplifying the derivation; these eigenvalues can be solved numerically.

3.2.2 Changing bases

Our derivation proceeds by realising that $\hat{\sigma}_x$ is defined in the superposition basis whilst our H_{S} eigenstates in Eq. (3.15) are in a joint site-Fock basis and that we must unify these expressions. Let us define the superposition basis TLS lowering and raising operators $\hat{\sigma}_- = |-\rangle\langle+|$ and $\hat{\sigma}_+ = |+\rangle\langle-|$ such that $\hat{\sigma}_x = \hat{\sigma}_+ + \hat{\sigma}_-$. Since the eigenstates span both the TLS and SM we actually require

$$\hat{\sigma}_{+n} = \hat{\sigma}_+ \otimes \hat{I} = \sum_n |+n\rangle\langle-n|, \tag{3.21}$$

$$\hat{\sigma}_{-n} = \hat{\sigma}_- \otimes \hat{I} = \sum_n |-n\rangle\langle+n|. \tag{3.22}$$

To aid us with the change of basis of $\hat{\sigma}_x$ we wish next to write a superposition basis expansion of the eigenstates

$$|\psi_k^{\pm}\rangle = \frac{1}{2}\left[(\hat{P} \pm 1)|+\rangle - (\hat{P} \mp 1)|-\rangle\right]|\phi_k^{\pm}\rangle, \tag{3.23}$$

$$|\phi_k^{\pm}\rangle = \sum_n C_{kn}^{\pm}|n\rangle. \tag{3.24}$$

The $C_{kn}^{\pm} = \langle n|\phi_k^{\pm}\rangle$ coefficients in the Fock expansion of the SM subspace eigenstates are calculated numerically. Looking at the definitions above we can observe that the superposition basis states are associated with Fock states of differing parity as

$$|\psi_k^{\pm}\rangle = \sum_{\text{even } n} C_{kn}^{\pm}|\pm n\rangle + \sum_{\text{odd } n} C_{kn}^{\pm}|\mp n\rangle; \tag{3.25}$$

it is clear here that $\langle \psi_k^{\pm}|\psi_{k'}^{\mp}\rangle = 0$ because of the orthogonality of the superposition and Fock states.

Knowing expressions for the eigenstates in the superposition basis means we can now approach our conversion of $\hat{\sigma}_-$ and $\hat{\sigma}_+$. We find the relevant matrix elements of the operators by overlap calculations with the eigenstates:

$$\langle \psi_k^{\pm}|\hat{\sigma}_{+n}|\psi_{k'}^{\pm}\rangle = \langle \psi_k^{\pm}|\hat{\sigma}_{-n}|\psi_{k'}^{\pm}\rangle = 0 \tag{3.26}$$

$$\langle \psi_k^{\pm}|\hat{\sigma}_{\pm n}|\psi_{k'}^{\mp}\rangle = \sum_{\text{even } n} C_{nk}^{\pm}C_{k'n}^{\mp} \tag{3.27}$$

$$\langle \psi_k^{\mp}|\hat{\sigma}_{\pm n}|\psi_{k'}^{\pm}\rangle = \sum_{\text{odd } n} C_{nk}^{\mp}C_{k'n}^{\pm}. \tag{3.28}$$

Notice the subscript reversal of the first $C^{\pm}$ within each pairing compared to the Eq. 3.24 definition; this is intended to signify complex conjugation, $C_{nk}^{\pm} = \left(C_{kn}^{\pm}\right)^*$. Combining our expressions we find the form of our operators

$$\hat{\sigma}_{\pm n} = \sum_{k,k'}\left\{\sum_{\text{even } n} C_{nk}^{\pm}C_{k'n}^{\mp}|\psi_k^{\pm}\rangle\langle\psi_{k'}^{\mp}| + \sum_{\text{odd } n} C_{nk}^{\mp}C_{k'n}^{\pm}|\psi_k^{\mp}\rangle\langle\psi_{k'}^{\pm}|\right\}. \tag{3.29}$$

Summing the two ladder operators together to build $\hat{\sigma}_x$ reduces the complexity of Eq. (3.29) slightly as odd and even n components are combined to leave a single

contiguous summation over n;

$$\hat{\sigma}_{xn} = \sum_{k,k',n} \left\{ C_{nk}^+ C_{k'n}^- \left| \psi_k^+ \right\rangle \left\langle \psi_{k'}^- \right| + C_{nk}^- C_{k'n}^+ \left| \psi_k^- \right\rangle \left\langle \psi_{k'}^+ \right| \right\}. \tag{3.30}$$

3.2.3   Moving to the interaction picture

We can finally convert the system dependent part of H_I in Eq. (3.20) to the interaction picture,

$$\mathrm{e}^{iH_\mathrm{S}t} \hat{\sigma}_{xn} \mathrm{e}^{-iH_\mathrm{S}t} = \sum_{k,k',n} \left\{ C_{nk}^+ C_{k'n}^- \mathrm{e}^{i\Lambda_{kk'}t} \left| \psi_k^+ \right\rangle \left\langle \psi_{k'}^- \right| + C_{nk'}^- C_{kn}^+ \mathrm{e}^{-i\Lambda_{kk'}t} \left| \psi_{k'}^- \right\rangle \left\langle \psi_k^+ \right| \right\}. \tag{3.31}$$

We have swapped the k and k' indices in the second term to facilitate the definition of a constant,

$$\Lambda_{kk'} = E_k^+ - E_{k'}^-, \tag{3.32}$$

the difference between the contributing eigenvalues.

Two identities

$$\mathrm{e}^{\alpha \hat{n}} \hat{b} \mathrm{e}^{-\alpha \hat{n}} = \hat{b} \mathrm{e}^{-\alpha}, \tag{3.33}$$

$$\mathrm{e}^{\alpha \hat{n}} \hat{b}^\dagger \mathrm{e}^{-\alpha \hat{n}} = \hat{b}^\dagger \mathrm{e}^{\alpha}, \tag{3.34}$$

are required to change the bath dependent part of Eq. (3.20) into the interaction picture. Using these we have all that we need to fully convert to an interaction representation,

$$H_\mathrm{I}(t) = \sum_{k,k'} \mathrm{e}^{i\Lambda_{kk'}t} \hat{B}^\dagger(t) \hat{\zeta}_{kk'}^+ + \mathrm{e}^{-i\Lambda_{kk'}t} \hat{B}^\dagger(t) \hat{\zeta}_{k'k}^- + \mathrm{e}^{i\Lambda_{kk'}t} \hat{B}(t) \hat{\zeta}_{kk'}^+ + \mathrm{e}^{-i\Lambda_{kk'}t} \hat{B}(t) \hat{\zeta}_{k'k}^-. \tag{3.35}$$

We have defined some new operators here; the $\hat{B}(t)$ and $\hat{B}^\dagger(t)$ are bath annihilation and creation operators in the interaction picture,

$$\hat{B}(t) = \sum_{\mathbf{q}} h_{\mathbf{q}} \hat{b}_{\mathbf{q}} e^{-i\omega_{\mathbf{q}}t}, \tag{3.36}$$

$$\hat{B}^\dagger(t) = \sum_{\mathbf{q}} h_{\mathbf{q}} \hat{b}_{\mathbf{q}}^\dagger e^{i\omega_{\mathbf{q}}t}, \tag{3.37}$$

and the $\hat{\zeta}$'s switch between Fulton-Gouterman eigenstates,

$$\hat{\zeta}_{kk'}^+ = \sum_n C_{nk}^+ C_{k'n}^- \left| \psi_k^+ \right\rangle \left\langle \psi_{k'}^- \right|, \tag{3.38}$$

$$\hat{\zeta}_{k'k}^- = \sum_n C_{nk'}^- C_{kn}^+ \left| \psi_{k'}^- \right\rangle \left\langle \psi_k^+ \right|. \tag{3.39}$$

3.2.4 Generation of the master equation

Now we can proceed to evaluate the double commutator in Eq. (3.18) which requires combining the various operators we have discussed up until now; noting that $\hat{\zeta}_{kk'}^+ \hat{\zeta}_{ll'}^+ = \hat{\zeta}_{k'k}^- \hat{\zeta}_{l'l}^- = 0$ helps to reduce the number of terms. Due to the separable nature of the formulae presented, the partial trace over the double commutator boils down to a trace over the bath operators in each additive term in the expanded commutators. This again allows for a further reduction of terms as $\langle \hat{B}(t)\hat{B}(t') \rangle = \langle \hat{B}^\dagger(t)\hat{B}^\dagger(t') \rangle = 0$, where the use of angular brackets denotes the trace over a thermal density matrix (the assumed state of the environmental bath). A multi-mode thermal density matrix takes the form

$$\rho_{\mathrm{B}} = N \prod_{\mathbf{p}} e^{-\beta \omega_{\mathbf{p}} \hat{n}_{\mathbf{p}}}, \tag{3.40}$$

with the normalisation constant

$$
\begin{aligned}
N^{-1} &= \sum_{\{n\}} \langle n_0, n_1... | \prod_{\mathbf{p}'} \mathrm{e}^{-\beta\omega_{\mathbf{p}'}\hat{n}_{\mathbf{p}'}} | n_0, n_1... \rangle \\
&= \sum_{\{n\}} \langle n_0, n_1... | \mathrm{e}^{-\beta\omega_0\hat{n}_0} \mathrm{e}^{-\beta\omega_1\hat{n}_1} ... | n_0, n_1... \rangle \\
&= \sum_{\{n\}} \langle n_0 | \mathrm{e}^{-\beta\omega_0\hat{n}_0} | n_0 \rangle \langle n_1 | \mathrm{e}^{-\beta\omega_1\hat{n}_1} | n_1 \rangle ... \\
&= \prod_{\mathbf{p}'} \sum_{n_{\mathbf{p}'}} \mathrm{e}^{-\beta\omega_{\mathbf{p}'}n_{\mathbf{p}'}} \\
N &= \prod_{\mathbf{p}'} 1 - \mathrm{e}^{-\beta\omega_{\mathbf{p}'}}
\end{aligned}
\tag{3.41}
$$

This could also be written as $N = \prod_i N_i$ where $N_i = 1 - \mathrm{e}^{-\beta\omega_i}$.

Now let us take a look at the non-zero bath correlation functions $\langle \hat{B}^\dagger(t)\hat{B}(t') \rangle$ and $\langle \hat{B}(t)\hat{B}^\dagger(t') \rangle$. We shall explicitly evaluate here the first of these:

$$
\begin{aligned}
\langle \hat{B}^\dagger(t)\hat{B}(t') \rangle &= N \sum_{\{n\}} \langle n_0, n_1... | \sum_{\mathbf{q},\mathbf{q}'} h_{\mathbf{q}} \hat{b}_{\mathbf{q}}^\dagger \mathrm{e}^{i\omega_{\mathbf{q}}t} h_{\mathbf{q}'} \hat{b}_{\mathbf{q}'} \mathrm{e}^{-i\omega_{\mathbf{q}'}t'} \prod_{\mathbf{p}} \mathrm{e}^{-\beta\omega_{\mathbf{p}}\hat{n}_{\mathbf{p}}} | n_0, n_1... \rangle \\
&= N \sum_{\{n\}} \langle n_0, n_1... | \sum_{\mathbf{q}} h_{\mathbf{q}}^2 \hat{n}_{\mathbf{q}} \mathrm{e}^{i\omega_{\mathbf{q}}(t-t')} \prod_{\mathbf{p}} \mathrm{e}^{-\beta\omega_{\mathbf{p}}\hat{n}_{\mathbf{p}}} | n_0, n_1... \rangle \\
&= N \sum_{\{n\}} \langle n_0, n_1... | h_0^2 \hat{n}_0 \mathrm{e}^{i\omega_0(t-t')} \prod_{\mathbf{p}} \mathrm{e}^{-\beta\omega_{\mathbf{p}}\hat{n}_{\mathbf{p}}} \\
&\qquad + h_1^2 \hat{n}_1 \mathrm{e}^{i\omega_1(t-t')} \prod_{\mathbf{p}} \mathrm{e}^{-\beta\omega_{\mathbf{p}}\hat{n}_{\mathbf{p}}} + ... | n_0, n_1... \rangle \\
&= N \sum_{\{n\}} \Bigg[\langle n_0, n_1... | h_0^2 \hat{n}_0 \mathrm{e}^{i\omega_0(t-t')} \prod_{\mathbf{p}} \mathrm{e}^{-\beta\omega_{\mathbf{p}}\hat{n}_{\mathbf{p}}} | n_0, n_1... \rangle \\
&\qquad + \langle n_0, n_1... | h_1^2 \hat{n}_1 \mathrm{e}^{i\omega_1(t-t')} \prod_{\mathbf{p}} \mathrm{e}^{-\beta\omega_{\mathbf{p}}\hat{n}_{\mathbf{p}}} | n_0, n_1... \rangle + ... \Bigg] \\
&= \prod_i N_i \sum_{\{n\}} \Bigg[h_0^2 \hat{n}_0 \mathrm{e}^{i\omega_0(t-t')} \prod_{\mathbf{p}} \mathrm{e}^{-\beta\omega_{\mathbf{p}}\hat{n}_{\mathbf{p}}} \\
&\qquad + h_1^2 \hat{n}_1 \mathrm{e}^{i\omega_1(t-t')} \prod_{\mathbf{p}} \mathrm{e}^{-\beta\omega_{\mathbf{p}}\hat{n}_{\mathbf{p}}} + ... \Bigg].
\end{aligned}
\tag{3.42}
$$

In the last line of Eq. (3.42) each instance of the product over $\mathbf{p}$ has all of its elements cancel with the elements in the normalisation product (see the penultimate line in Eq. (3.41)), except when $\mathbf{p}$ equals the index of the term the product is a part of. This

leads to

$$\langle \hat{B}^\dagger(t)\hat{B}(t')\rangle = \sum_{\mathbf{p}} N_{\mathbf{p}} h_{\mathbf{p}}^2 e^{i\omega_{\mathbf{p}}(t-t')} \sum_{n_{\mathbf{p}}} n_{\mathbf{p}} e^{-\beta\omega_{\mathbf{p}} n_{\mathbf{p}}} = \sum_{\mathbf{p}} h_{\mathbf{p}}^2 \frac{e^{i\omega_{\mathbf{p}}(t-t')}}{e^{\beta\omega_{\mathbf{p}}} - 1}. \tag{3.43}$$

The last step in the process of solving the partial trace involves the SD, as defined in Chapter 2,

$$\chi(\omega) = \sum_{\mathbf{q}} |h_{\mathbf{q}}|^2 \delta(\omega - \omega_{\mathbf{q}}), \tag{3.44}$$

which uses the bath coupling factors, $h_{\mathbf{q}}$, to describe the action of the bath and allows the identity (see Eq. (2.21))

$$\int d\omega\, \chi(\omega)\phi(\omega) = \sum_{\mathbf{k}} h_{\mathbf{k}}^2 \phi(\omega_{\mathbf{k}}). \tag{3.45}$$

This is exactly what we see in Eq. (3.43), so finally

$$\langle \hat{B}^\dagger(t)\hat{B}(t')\rangle = \int d\omega\, \chi(\omega) \frac{e^{i\omega(t-t')}}{e^{\beta\omega} - 1}. \tag{3.46}$$

The evaluation of the second bath correlation function features $\hat{a}\hat{a}^\dagger = \hat{n}+1$ as opposed to the $\hat{a}^\dagger\hat{a} = \hat{n}$ we have just seen. This does not alter the derivation too much and leads us to

$$\langle \hat{B}(t)\hat{B}^\dagger(t')\rangle = \int d\omega\, \chi(\omega) \frac{e^{-i\omega(t-t')}}{1 - e^{-\beta\omega}}. \tag{3.47}$$

From the Eq. (3.18) double commutator and the definition in Eq. (3.35), taking into account all permutations of t, $t-s$, daggered and non-daggered bath operators there are four non-zero combinations required from the formulae in Eqs. (3.46) and (3.47).

By employing the identity

$$\int\limits_0^\infty ds\, e^{i(a-b)s} = \pi\delta(a-b) + \frac{P}{i(a-b)} \tag{3.48}$$

(where we neglect the second, principle value, term which would lead to only small Lamb shifts) the integrals over s, in Eq. (3.18), and ω, introduced by the bath correlation functions, can now be performed. Let us look at one of the four terms produced

when expanding the double commutator present in Eq. (3.18):

$$
H_{\mathrm{I}}(t)H_{\mathrm{I}}(t-s)\rho(t) = \sum_{k,k',p,p'} \left[\langle \hat{B}^\dagger(t)\hat{B}(t-s)\rangle + \langle \hat{B}(t)\hat{B}^\dagger(t-s)\rangle \right] \times
$$
$$
\left[\mathrm{e}^{i(\Lambda_{kk'}-\Lambda_{pp'})t}\mathrm{e}^{i\Lambda_{pp'}s}\hat{\zeta}^+_{kk'}\hat{\zeta}^-_{p'p}\rho_{\mathrm{S}}(t) + \mathrm{e}^{-i(\Lambda_{kk'}-\Lambda_{pp'})t}\mathrm{e}^{-i\Lambda_{pp'}s}\hat{\zeta}^-_{k'k}\hat{\zeta}^+_{pp'}\rho_{\mathrm{S}}(t) \right]. \quad (3.49)
$$

We can see here exponentiated s features associated with each of the system operator terms, but when we include the further s exponentials in the explicit form of the bath traces (Eqs. (3.46) and (3.47)) we get something of the form in Eq. 3.48. Accounting for the differing signs between the terms in the system part and the two flavours of bath trace present we have four combinations to evaluate; considering the whole of the double commutator we have eight combinations in total. Again, to proceed we shall explicitly show here one example of how to evaluate these terms with the others being similarly computable:

$$
\int_0^\infty \mathrm{d}s\, \langle \hat{B}^\dagger(t)\hat{B}(t-s)\rangle \mathrm{e}^{\pm i\Lambda_{pp'}s} = \int_0^\infty \mathrm{d}s \int_0^\infty \mathrm{d}\omega\, \chi(\omega)\frac{\mathrm{e}^{i(\omega\pm\Lambda_{pp'})s}}{\mathrm{e}^{\beta\omega}-1}
$$
$$
= \int_0^\infty \mathrm{d}\omega\, \chi(\omega)\frac{\delta(\omega\pm\Lambda_{pp'})}{\mathrm{e}^{\beta\omega}-1}
$$
$$
= \frac{\pi\chi(\mp\Lambda_{pp'})}{\mathrm{e}^{\mp\beta\Lambda_{pp'}}-1} = \Gamma(\mp\Lambda_{pp'}). \quad (3.50)
$$

We have defined Γ (and also shortly Γ') to simplify future equations; it describes the thermal decay rate of the associated transition denoted by Λ. The three remaining terms are:

$$
\int_0^\infty \mathrm{d}s\, \langle \hat{B}^\dagger(t-s)\hat{B}(t)\rangle \mathrm{e}^{\pm i\Lambda_{pp'}s} = \frac{\pi\chi(\pm\Lambda_{pp'})}{\mathrm{e}^{\pm\beta\Lambda_{pp'}}-1} = \Gamma(\pm\Lambda_{pp'}) \quad (3.51)
$$

$$
\int_0^\infty \mathrm{d}s\, \langle \hat{B}(t)\hat{B}^\dagger(t-s)\rangle \mathrm{e}^{\pm i\Lambda_{pp'}s} = \frac{\pi\chi(\pm\Lambda_{pp'})}{1-\mathrm{e}^{\mp\beta\Lambda_{pp'}}} = \Gamma'(\pm\Lambda_{pp'}) \quad (3.52)
$$

$$
\int_0^\infty \mathrm{d}s\, \langle \hat{B}(t-s)\hat{B}^\dagger(t)\rangle \mathrm{e}^{\pm i\Lambda_{pp'}s} = \frac{\pi\chi(\mp\Lambda_{pp'})}{1-\mathrm{e}^{\pm\beta\Lambda_{pp'}}} = \Gamma'(\mp\Lambda_{pp'}). \quad (3.53)
$$

We are now in a position to write out the first form of the differential equation we have been working towards from Eq. (3.18):

$$
\begin{aligned}
\frac{d\rho_S(t)}{dt} = -\sum_{k,k',p,p'} & \left[\Big(\Gamma(-\Lambda_{pp'}) + \Gamma'(\Lambda_{pp'})\Big) e^{i(\Lambda_{kk'}-\Lambda_{pp'})t} \hat{\zeta}^+_{kk'}\hat{\zeta}^-_{p'p}\rho_S(t) \right. \\
& + \Big(\Gamma(\Lambda_{pp'}) + \Gamma'(-\Lambda_{pp'})\Big) e^{-i(\Lambda_{kk'}-\Lambda_{pp'})t} \hat{\zeta}^-_{k'k}\hat{\zeta}^+_{pp'}\rho_S(t) \\
& + \Big(\Gamma(-\Lambda_{kk'}) + \Gamma'(\Lambda_{kk'})\Big) e^{i(\Lambda_{kk'}-\Lambda_{pp'})t} \rho_S(t)\hat{\zeta}^+_{kk'}\hat{\zeta}^-_{p'p} \\
& + \Big(\Gamma(\Lambda_{kk'}) + \Gamma'(-\Lambda_{kk'})\Big) e^{-i(\Lambda_{kk'}-\Lambda_{pp'})t} \rho_S(t)\hat{\zeta}^-_{k'k}\hat{\zeta}^+_{pp'} \\
& - \Big(\Gamma(-\Lambda_{pp'}) + \Gamma'(\Lambda_{pp'})\Big) \Big(e^{i(\Lambda_{kk'}+\Lambda_{pp'})t}\hat{\zeta}^+_{kk'}\rho_S(t)\hat{\zeta}^+_{pp'} + e^{-i(\Lambda_{kk'}-\Lambda_{pp'})t}\hat{\zeta}^-_{k'k}\rho_S(t)\hat{\zeta}^+_{pp'} \Big) \\
& - \Big(\Gamma(\Lambda_{pp'}) + \Gamma'(-\Lambda_{pp'})\Big) \Big(e^{-i(\Lambda_{kk'}+\Lambda_{pp'})t}\hat{\zeta}^-_{k'k}\rho_S(t)\hat{\zeta}^-_{p'p} + e^{i(\Lambda_{kk'}-\Lambda_{pp'})t}\hat{\zeta}^+_{kk'}\rho_S(t)\hat{\zeta}^-_{p'p} \Big) \\
& - \Big(\Gamma(\Lambda_{kk'}) + \Gamma'(-\Lambda_{kk'})\Big) \Big(e^{i(\Lambda_{kk'}+\Lambda_{pp'})t}\hat{\zeta}^+_{kk'}\rho_S(t)\hat{\zeta}^+_{pp'} + e^{i(\Lambda_{kk'}-\Lambda_{pp'})t}\hat{\zeta}^+_{kk'}\rho_S(t)\hat{\zeta}^-_{p'p} \Big) \\
& \left. - \Big(\Gamma(-\Lambda_{kk'}) + \Gamma'(\Lambda_{kk'})\Big) \Big(e^{-i(\Lambda_{kk'}+\Lambda_{pp'})t}\hat{\zeta}^-_{k'k}\rho_S(t)\hat{\zeta}^-_{p'p} + e^{-i(\Lambda_{kk'}-\Lambda_{pp'})t}\hat{\zeta}^-_{k'k}\rho_S(t)\hat{\zeta}^+_{pp'} \Big) \right].
\end{aligned}
$$

(3.54)

In order to simplify Eq. 3.54 we employ the secular approximation which assumes that if the oscillatory exponential factors have a non-zero frequency (i.e. $\Lambda_{kk'} - \Lambda_{pp'} \neq 0 \neq \Lambda_{kk'} + \Lambda_{pp'}$) then they correspond to a rapid oscillation compared to the time scale over which we have assumed ρ_S changes. These terms are neglected. To ensure $\Lambda_{kk'} - \Lambda_{pp'} = 0$ we can insert $\delta_{k,q}\delta_{k',q'}$ into the summation. Now $\Lambda_{kk'} + \Lambda_{pp'} \rightarrow 2\Lambda_{kk'}$ which in general is non-zero so these terms are neglected also (the special case of $2\Lambda_{kk} = 0$ would similarly mean $\Gamma(\pm\Lambda_{kk}) = 0$ and thus would not contribute to the dynamics). This vast simplification is our implementation of the secular approximation (mentioned in Chapter 2). Eq. 3.54 can now be written in Lindblad form giving us

$$
\begin{aligned}
\frac{d\rho_S(t)}{dt} = \sum_{k,k'} & \left[\Big(\Gamma(-\Lambda_{kk'}) + \Gamma'(\Lambda_{kk'})\Big)\Big(2\hat{\zeta}^-_{k'k}\rho_S(t)\hat{\zeta}^+_{kk'} - \hat{\zeta}^+_{kk'}\hat{\zeta}^-_{k'k}\rho_S(t) - \hat{\zeta}^-_{k'k}\hat{\zeta}^+_{kk'}\rho_S(t) \Big) \right. \\
& \left. + \Big(\Gamma(\Lambda_{kk'}) + \Gamma'(-\Lambda_{kk'})\Big)\Big(2\hat{\zeta}^+_{kk'}\rho_S(t)\hat{\zeta}^-_{k'k} - \hat{\zeta}^-_{k'k}\hat{\zeta}^+_{kk'}\rho_S(t) - \hat{\zeta}^+_{kk'}\hat{\zeta}^-_{k'k}\rho_S(t) \Big) \right]. \quad (3.55)
\end{aligned}
$$

3.2.5 Characterising the environment

Clearly the behaviour of our derived Eq. 3.55 depends on the transition rates governed by Γ and Γ' which we defined in Eqs. (3.50)-(3.53). They are results of the bath correlations and as such depend on the form of χ, the SD. We defined this earlier as a discrete function but, as we implied in Chapter 2, in calculations the SD typically takes a physically motivated form in the continuum limit. Before we introduce the forms of χ we used, we will just touch on a subtlety of the definitions and derivations presented so far. Since all bosonic modes have a finite, positive frequency, ω, the SD is unphysical for $\omega < 0$. Therefore it is typical, in a derivation such as this, to neglect terms in which the SD has a negative input. In this instance, however, we cannot say in general if any of the $\Lambda_{kk'}$ (the difference between the k-th even parity and k'-th odd parity eigenvalues) are always negative, so we must continue to include calculation of them and programme our numerical solution to neglect them if negative.

The first continuous SD we use is

$$\chi_m(\omega) = A_m \omega^m e^{-\omega^2/\omega_{m,c}^2}, \tag{3.56}$$

where m controls whether we have an Ohmic form ($m = 1$) or a super-Ohmic form ($m > 1$) [87]. We include a Gaussian cutoff which ensures $\chi \to 0$ for $\omega \gg \omega_{m,c}$, the cutoff frequency, meaning high frequency modes do not contribute to the environmental dynamics. The second continuous SD form we employ is

$$\chi_L(\omega) = \frac{A_L \omega W^2}{(\omega - \omega_{L,c})^2 + W^2}, \tag{3.57}$$

a Lorentzian-like description. The half width at half maximum is W and the cutoff frequency is $\omega_{L,c}$. The normalisation factors A_m and A_L scale each SD and are related to the reorganisation energy, λ. As defined in Chapter 2, λ quantifies the change in energy of the bath in response to the TLS dynamics. Although Eq. (3.57) is modified with an extra factor of ω in order to ensure normalisability for λ, we shall refer to it simply as a Lorentzian for conciseness. Lorentzian forms can be useful for describing structured spectral densities such as the high frequency example in Fig. 2.1.
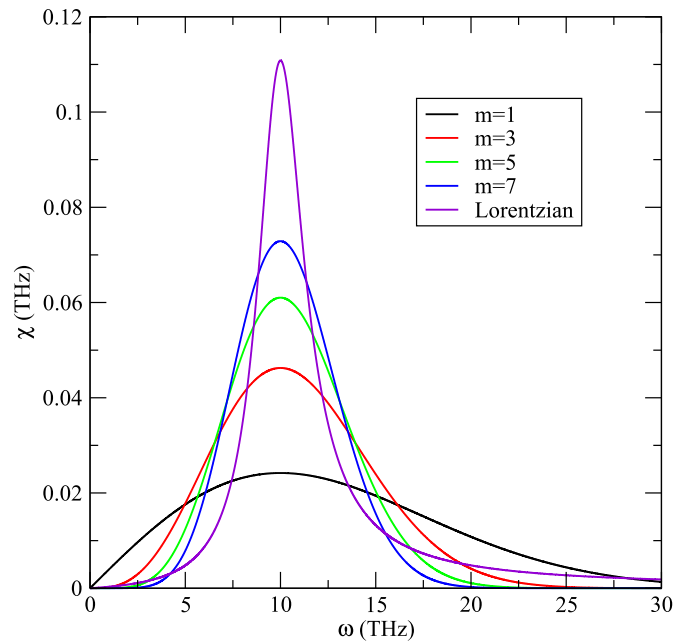
FIGURE 3.3: A comparative plot of the five SDs considered here, with $\lambda = 0.05$ THz and $\omega_p = 10$ THz. The Ohmic SD is given by $m = 1$, while $m = 3, 5, 7$ represent increasingly peaked super-Ohmic SDs. The Lorentzian SD has width $W = 1.5$ THz.

Fixing λ helps to make fair comparisons of the effects of different forms of the SD, but we should also consider fixing the peak location of each form. The frequency at which the peak occurs, ω_{p}, is found through differentiation of Eqs. (3.56) and (3.57). If we formulate a SD to depend on a cutoff frequency determined by a fixed peak frequency we can be confident of comparable SD forms. In Fig. 3.3 we can see examples of the $m = 1, 3, 5, 7$ and Lorentzian SDs for fixed λ and ω_{p}. The tendency for a more peaked SD to have a narrower widths means an enhanced bath interaction at that frequency but decreasing effectiveness for other frequencies. An Ohmic SD is a good description of the environment in surface-surface tunnelling problems and at low temperatures, whereas super-Ohmic SDs are a often used for bulk phonon environments [134, 145].

3.3 Computational implementation

BEFORE we move onto our results sections let us have a brief review of some of the computational aspects of the solution. Python was used to program our numerical solution with the 'Quantum Toolbox in Python' library (QuTiP) providing

a routine for handling the actual solution of Eq. 3.55 [146]. Python was chosen as it is currently a programming language seeing increased usage and provides well maintained libraries and extensions making it a logical choice for reliable code in that respect. It can handle parallelised implementations and in my experience is not severely slower than a more traditional scientific language such as Fortran. QuTiP provides convenient structures for handling quantum entities such as operators and kets, however I found that some of the more intensive linear algebra associated with the basis changes and generation of the Lindblad operators was faster with Python's standard libraries.

What follows is a brief synopsis of the main points of the code. The initial ρ_S is defined in the site-Fock basis with a truncation of the Fock levels of the SM. Next the sub-space Hamiltonians, $H^{\pm}$, are defined and diagonalised, producing the eigenvalues $E^{\pm}$ and the eigenvectors $|\phi_k^{\pm}\rangle$. The eigenvectors are then used to construct $|\psi_k^{\pm}\rangle$, following Eq. 3.15, and to calculate the $C_{kn}^{\pm}$ constants, via the overlap operation. In turn, those constants are used to generate a list of Lindblad operators complete with decay rates (each (k, k') element from the summation in Eq. 3.55 provides two list entries). The final set-up task is to convert the site-Fock initial ρ_S into the FGT basis (this is the same basis in which the Lindblad operators act).

In terms of the number of lines of code the solution step is dwarfed by set up and analysis, however during run time it is here that most processing time is spent. The QuTiP master equation dynamics routine requires the system Hamiltonian ($\hat{H}_S$), initial ρ_S, Lindblad operators and the time over which to solve for. In the FGT basis $\hat{H}_S$ is a diagonal matrix consisting of the list of E^+ eigenvalues followed by the E^- values. The solver produces a ρ_S, in the FGT basis, for each requested time step; this is the processor intensive step.

The analysis phase entails converting the solution density matrices back into the site-Fock basis and partially tracing out the SM to obtain the TLS dynamics. The dynamics are saved in text files so that a plotting tool can then interpret them. Also stored is an error check of sorts: the elements in the right- and bottom-most column and row respectively in each quadrant of each site-Fock ρ_S are summed together. This number helps provide some insight into whether the truncation of the Fock space has

occurred at a suitably high enough level; if it has not then there will be significant population of these elements. This is only an indication however, as I discovered numerical errors build up in the bottom left and top right of each quadrant. Whilst these regions are not pertinent to the partially traced dynamics they certainly affect the error summation. A further error check of the truncation level is obtained by printing a visualisation of the initial and final site-Fock density matrices. The dynamics themselves have also been converged with truncation point and with all of this in mind we can refer to our treatment of this TLS-SM system as exact.

3.4 Results

UNLESS otherwise stated, simulations are carried out with $\Omega = 100$ THz, $T = 300$ K, $J = 5$ THz, $\lambda = 0.05$ THz and $\omega_\mathrm{p} = 2J$. So our SM frequency, Ω, is far off-resonant from the TLS transition frequency of $2J$, whereas the peak of all SDs will be on resonance with it. These parameters have been chosen as they display the interesting off-resonant SM effects quite clearly. The initial state of the TLS is with the exciton localised on site 1. We wish initially for our SM to be in a thermal state and there are two straightforward ways of initialising this: 1) thermalising the SM before 'activating' its interaction with the TLS or 2) thermalising the SM whilst the two subsystems are interacting. The first method can be suitably described by a thermalised distribution of Fock states of the SM. The second leads to a thermal distribution with respect to the appropriately displaced oscillator states of the SM with respect to the initial state of the TLS [147]; this will be discussed in more detail in subsection 3.4.4. If the first case was employed then, as the simulation begins, the SM is not in a 'relaxed' state with reference to the TLS state and this will cause transient dynamics as the SM responds. We choose to focus on the second case so as to minimise this noise in our dynamics.

3.4.1 Preliminary result

An instructive first simulation to discuss is the behaviour of the TLS when coupled to the SM but with no bath (i.e. $\lambda = 0$ THz), as in Fig. 3.4. The curves in Fig. 3.4(a) show

the population of site 1 for four values of g. With the SM decoupled ($g = 0$) the pattern is a simple sinusoid of frequency $f = 2J/2\pi$ THz. The interaction of the SM ($g \neq 0$) introduces two distinct effects: 1) a renormalisation of the oscillation frequency and 2) an extra oscillatory envelope. As g increases, these effects become more prominent; they are also dependent on the ratio J/Ω and the initial conditions. By selecting the displaced oscillator SM initial condition we obtain the displayed simple sinusoidal dynamics. If we had chosen to thermalise the mode in the non-displaced basis, which corresponds to a coherent state in the displaced oscillator basis, we would see a third effect as g increases with the dynamics containing many competing oscillation frequencies superposing presenting as noisier dynamics.
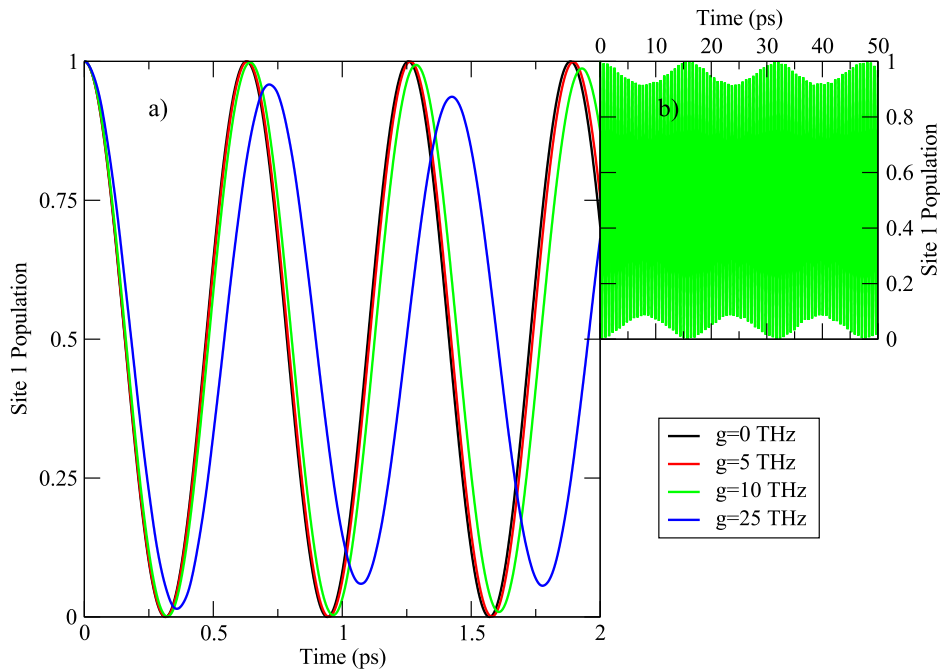
FIGURE 3.4: a) A comparison of the population dynamics for varied SM coupling strength with no bath present and b) longer dynamics of one coupling strength. In a) oscillation frequency renormalisation is clear for $g = 10$ THz and an envelope can be seen for $g = 25$ THz and in b) for the long time $g = 10$ THz dynamics.

The cause of the distinct dynamical effects can be inferred from the simple plot of the eigenenergies in Fig. 3.5. In general the spectrum is a ladder of states with each 'rung' consisting of a split doublet. The $g = 0$ spectrum consists of equally spaced levels according to the SM frequency, Ω, and doublets split J either side (in the regime that Ω is large compared to J). As g increases, the first noticeable change is a narrowing of the doublet gap, this corresponds to a smaller frequency of oscillation hence

the visible increases in period in Fig. 3.4. When the SM is coupled to the TLS there is mixing between the two systems; oscillations between the doublet states at each level in the ladder may evolve with differing phases, hence the oscillatory envelopes in Fig. 3.4.
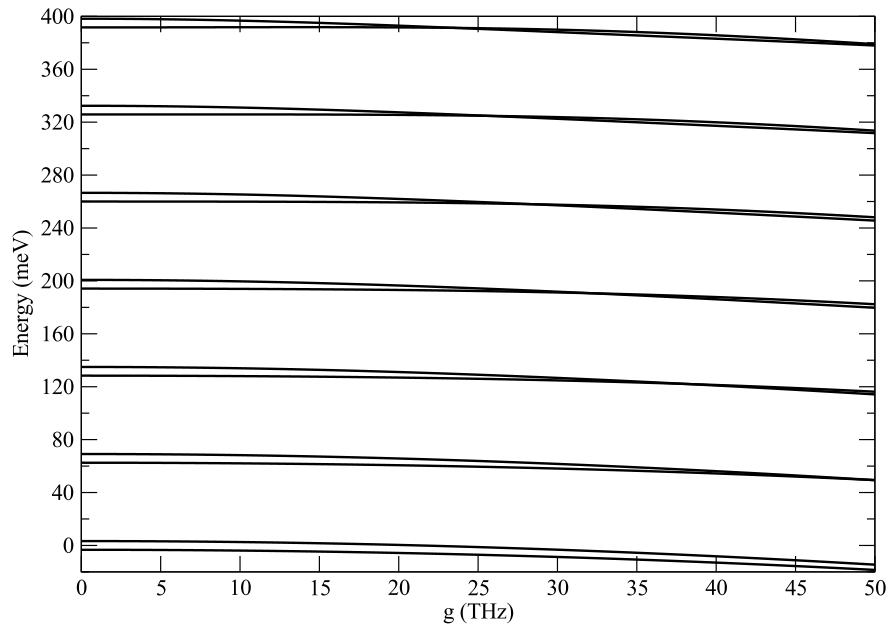

FIGURE 3.5: Truncated energy spectrum of the TLS-SM system for increasing g. Levels crossings are clearly exhibited.

3.4.2 An Ohmic environment

The renormalisation of the oscillation frequency (or effective TLS 'rung' splitting) is the key to the findings to be presented here. However we can start with the result that might naively be expected when a room temperature thermal bath is coupled to the system. Initially characterised with an Ohmic SD, the effect of the bath on the TLS, with no SM coupling ($g = 0$), is to damp the oscillations to a thermal equilibrium. As can be seen in Fig. 3.6, this characteristic remains when introducing the SM ($g > 0$). What can also be observed is that, more than simply remaining, there is actually an enhanced damping effect brought about by a strongly coupled SM. This is likely due to the mixing of different transitions induced by strong-g providing an increased number of decay pathways. The frequency renormalisation is also visible as a subtle curvature in the peak trajectories. One could argue that the effect of increased damping saturates towards the upper limit of the g range explored. This observation

hints at a more interesting behaviour: that a strongly coupled SM can provide some degree of decoherence-robustness.
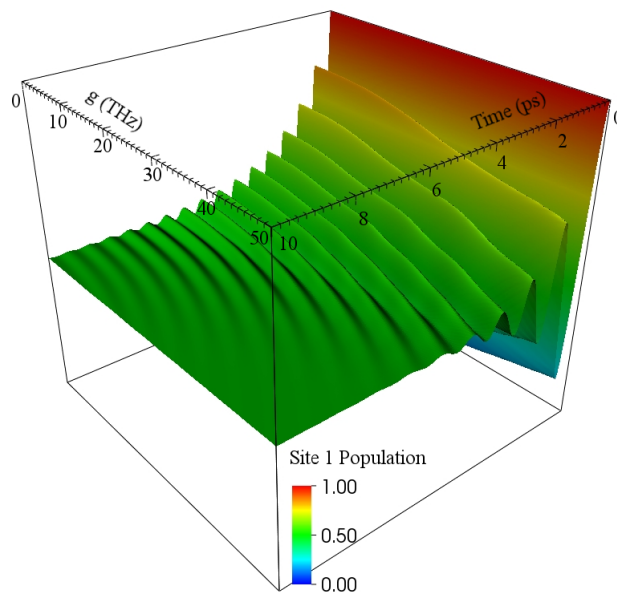

FIGURE 3.6: A 3D plot of the site 1 population dynamics a function of g when coupled to an environment described by an Ohmic ($m = 1$) SD. A frequency renormalisation an enhanced damping effect are observable for strong-g.

3.4.3 Super-Ohmic environments

Let us proceed to display the dynamics of SDs with $m = 3, 5$ and 7 to further explore this effect. The qualitative difference between the dynamics in Fig. 3.6 and Fig. 3.7 is clear: as the SM coupling strength is increased the oscillations are enhanced instead of damped. The behaviour is most easily appreciated when looking in the second half of the simulated time in Fig. 3.7 where the weak-g plateaus are replaced with population oscillations for strong-g. A more peaked SD exhibits these oscillations more strongly.

3.4.4 Analysis

This subsection describes analytic work performed by Elinor K. Irish in understanding these behaviours and was included in our publication of this work (Publication 1); what follows is my interpretation of it.
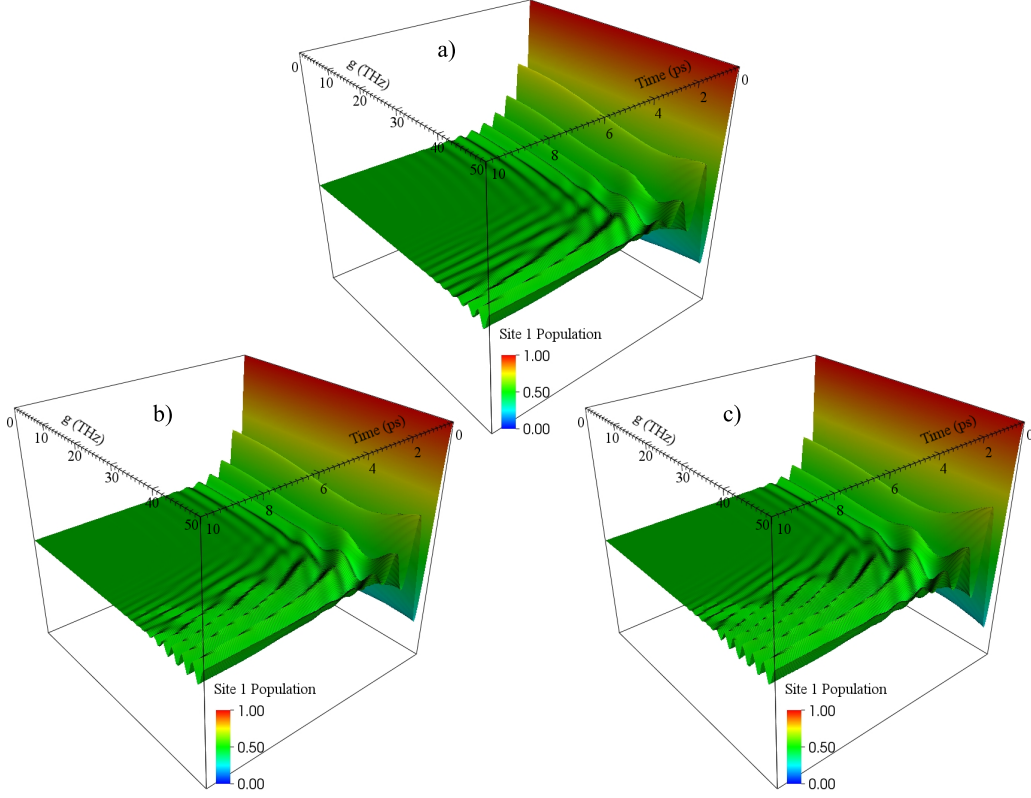
FIGURE 3.7: Site 1 population dynamics as a function of g when coupled to super-Ohmic SDs with a) $m = 3$, b) $m = 5$ and c) $m = 7$. A clear enhancement is seen for strong-g which becomes more pronounced with more peaked SDs.

As seen in Fig. 3.4 the dynamics of the TLS without SM or bath couplings display sinusoidal population oscillations between the sites. In the subsequent figures it can be seen that inclusion of the bath (for $g = 0$) causes these oscillations to be damped. Looking at Figs. 3.6 and 3.7 though we can definitely see that the SM $g > 0$ complicates this behaviour. If we consider the TLS-SM system without a bath, as we did at the start of this results section, we can make use of the approximate displaced oscillator basis of Irish *et al* [147]; this is the initial state we are employing. Provided, as we have here, $J \ll \Omega$ then a valid approximation for the system is two harmonic oscillator potentials, one associated with each of the TLS sites. The displaced oscillator basis gets its name from the fact that, in position space, the potential wells are displaced as the SM and TLS interact.

In this picture the system eigenstates can be represented by

$$|\Psi_n^\pm\rangle = \frac{1}{\sqrt{2}}(|0\rangle \otimes |n_0\rangle \pm |1\rangle \otimes |n_1\rangle), \tag{3.58}$$

where the TLS sites are denoted by $|i\rangle$ and the Fock state of each displaced oscillator is given by $|n_i\rangle$. With respect to the original, undisplaced Fock basis of the SM $|n_0\rangle = \exp[-(g/\Omega)(\hat{a}^\dagger + \hat{a})]|n\rangle$ and $|n_1\rangle = \exp[(g/\Omega)(\hat{a}^\dagger + \hat{a})]|n\rangle$. The approximate eigenenergies of these displaced states,

$$E_{\pm,n} = \Omega\left(n - \frac{g^2}{\Omega^2}\right) \pm Je^{-2g^2/\Omega^2} L_n\left(\frac{4g^2}{\Omega^2}\right), \tag{3.59}$$

form the same doublet-ladder structure as in Fig. 3.5.

If a system is initialised on one TLS site and in a corresponding Fock state of that displaced oscillator and behaves following this approximating theory it should be clear that it will exhibit sinusoidal oscillations between sites of a frequency determined by the doublet splitting

$$\Delta E_n = 2Je^{-2g^2/\Omega^2} L_n(4g^2/\Omega^2). \tag{3.60}$$

We can see first hand now from Eq. (3.60) that an increased g leads to a frequency renormalisation so the frequency reduction for strong-g in Figs. 3.6 and 3.7 can be explained with this approximate analytic approach; also this g dependence is responsible for the oscillations along the g-axis. Further, since the doublet splitting depends on n, an initial state with multiple Fock states will feature dynamics with multiple different frequencies in the TLS population oscillations. In considering $T = 300$ K we find our thermal SM of $\Omega = 100$ THz in $n = 0$ with a probability of $\sim 92\%$ and $n = 1$ with a probability of $\sim 7\%$; all other states are occupied with a probability smaller than 1%. This implies that the dynamics shown in Figs. 3.6 and 3.7 should feature strongly only two oscillation frequencies; we can see these as a function of g in Fig. 3.8(a). There is clearly a renormalisation effect here: both frequencies decrease for increasing g, with the $n = 1$ doublet reducing more rapidly.

The enhanced coherence effects in Fig. 3.7 can also be understood in terms of the frequency renormalisation caused by the SM. These simulations were carried out with a default TLS oscillation frequency $\omega = 2J = 10$ THz which is resonant with the peak of the SDs used. Therefore the system is expected to experience a strong decay effect from the coupled bath and this is indeed observed with all SDs for weak-g and
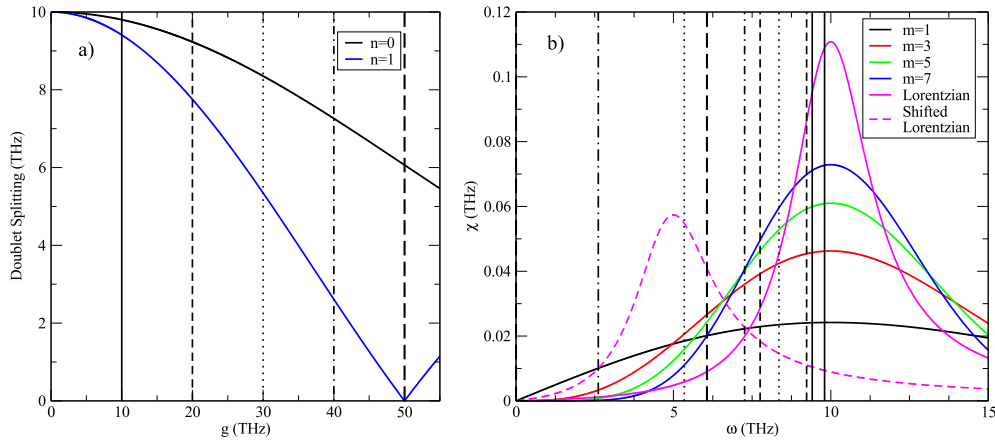
FIGURE 3.8: (a) Energy splittings in the adiabatic approximation as a function of g, for the doublets corresponding to the $n = 0$ (black) and $n = 1$ (blue) states of the displaced SM. Vertical lines indicate the values of g used in (b) below. (b) Comparison of the doublet splittings with the various SDs, showing the frequencies at which the SDs are sampled for various values of g. The vertical lines indicate the $n = 0$ and $n = 1$ splittings for the values of g that have been marked in (a) with the same line style. In each case the higher frequency corresponds to $n = 0$ and the lower to $n = 1$. As g increases, both frequencies decrease but they also move further apart.

the whole range of g for the Ohmic case. However, we see the effectiveness of the bath reduce as we increase g for the super-Ohmic cases because the frequency is adjusted off resonance with the SDs. This tendency is presented in Fig. 3.8(b) where the SDs are plotted, overlayed with the frequencies at which the two doublet splittings that govern the oscillations sample them (taken from Fig. 3.8(a)). We can see here plainly that as the $n = 0$ mode is slower to change its frequency it is always more strongly damped than the $n = 1$ mode.

3.4.5 Long time behaviour

One thing that is not easy to see in the plots in Fig. 3.7 is the apparent asymmetry that is introduced to the population oscillations for strong-g. This is due to that dominant underdamped $n = 1$ mode which introduces a long-time envelope which does eventually decay to the thermal equilibrium population, but over a time-scale much greater than the ps dynamics shown so far. An example of ns dynamics is shown in Fig. 3.9 for an $m = 3$ super-Ohmic SD. As a general review of the situation let it be noted here that even at strong-g the ohmic SD decays the $n = 1$ mode. This is

clearly not the case for the $m = 3$ super-Ohmic SD in Fig. 3.9; it shows no signs of decay even after 5 ns. The steady state value of 0.5 was obtained numerically and is to be expected for a symmetric dimer undergoing dissipative evolution. Although not obvious, this envelope feature is present in Fig. 3.7 as an apparent population equilibrium greater than 0.5 at $t \gtrsim 6$ ps. The time period shown in Fig. 3.7(a) is essentially a transient-dynamics regime which can just be discerned in Fig. 3.9. During this transient period any other higher excited level of the TLS-SM spectrum gets damped away by the SD to leave the single, slowly oscillating, $n = 1$ feature. In terms of our analytic explanation, at $g = 50$ THz the $n = 1$ doublet is almost degenerate and this means a small frequency (long period) and low SD damping which can all be seen in Fig. 3.8.
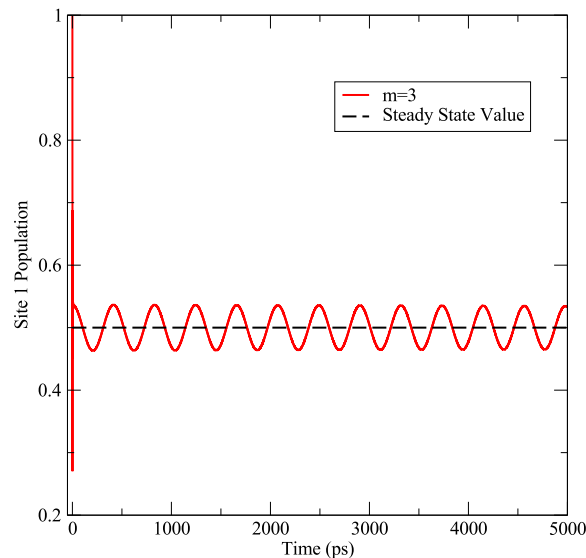
FIGURE 3.9: An example of long time dynamics for strongly coupled TLS-SM system, $g = 50$THz, displaying ns coherent dynamics in an $m = 3$ super-Ohmic environment due to the weakly damped $n = 1$ mode.

3.4.6 A resonant Lorentzian environment

Our analytic understanding allows us to make certain predictions for what we expect from the dynamics when the much more peaked Lorentzian SD is used. It can be seen in Figs. 3.6 and 3.7 that increasing m causes enhanced population damping in the weak-g regime which is due to the SD peak amplitude increasing. The Lorentzian SD shown in Fig. 3.3 is clearly far more peaked than the other curves represented

alongside it. This means we would expect the strongest damping of weak-g oscillations witnessed thus far as our Lorentzian peak is still resonant with our bare TLS oscillation frequency. The dynamics in the presence of a Lorentzian environment are shown in Fig. 3.10 and we can clearly see this prediction is correct. The second thing we expect to see is a larger enhanced coherence region in the strong-g regime since the narrower Lorentzian SD will damp the shifted $n = 0, 1$ modes less (as predicted in Fig. 3.8(b)). It is immediately obvious in Fig. 3.10 that this is indeed the case with the transient dynamics lasting right up to the 10 ps window simulated.
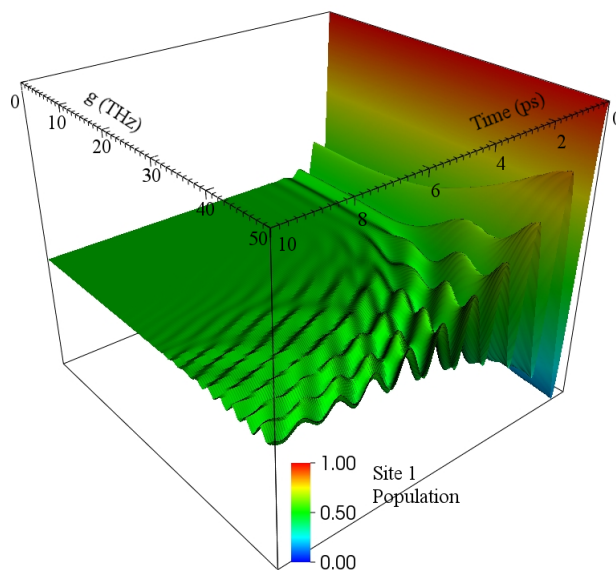
FIGURE 3.10: A 3D plot of the site 1 population dynamics as a function of g when coupled to a Lorentzian SD with $W = 1.5$ THz.

The nature of our Lorentzian can be modified my altering the width parameter, W, to make a more or less peaked SD or possibly a number of them could be combined to represent a more structured environment. However, a much smaller width would cause the Born-Markov approximation employed in our derivation to become of questionable validity; it relies on bath time scales being less than system time scales. In this case the system time scale can be approximated by $\tau_\text{S} = 2J/2\pi \approx 0.6$ ps and the bath time scale is $\tau_\text{B} = 1/2W \approx 0.3$ ps. We see here that we are justified in utilising the Born-Markov approximation with a Lorentzian SD and since the $m = 1, 3, 5, 7$ SDs are all broader (leading to a smaller bath time scale still) then it is justified for these as well.

3.4.7 A sub-resonant Lorentzian environment

Our description of the system's reaction to increasing SM coupling strength has an interesting prediction for the dynamics if ω_p is no longer on resonance with the TLS but is instead below it. Now when g increases and reduces the TLS oscillation frequencies they will no longer be brought away from strong damping but will be moved towards it, and as we can see in Fig. 3.11 this does indeed occur. The shifted Lorentzian in Fig. 3.8(b) is being used as the environment description here, with its $\omega_p = 5$ THz (a fact which, in order to maintain $\lambda = 0.05$ THz normalisation, means its form is modified). With the bare TLS oscillation frequency still $2J = 10$ THz we can see the initially strong oscillations become damped away as g increases due to the $n = 0$ mode component being brought closer to resonance with the SD.
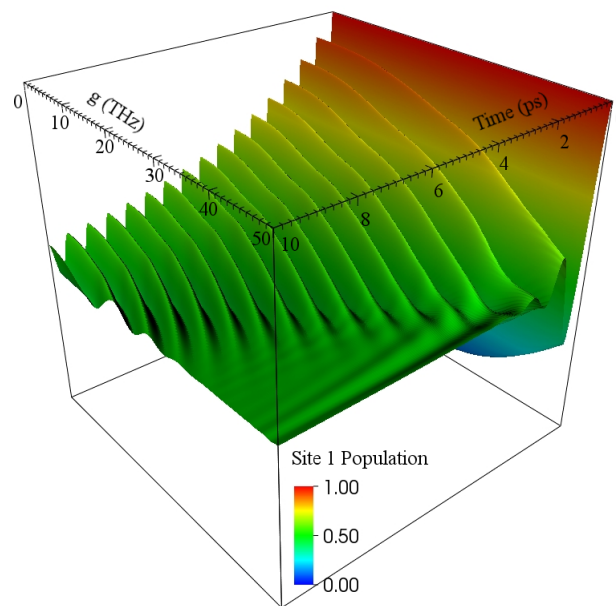
FIGURE 3.11: Site 1 population dynamics of the TLS where the bath SD is given by a Lorentzian with peak frequency $\omega_p = 5$ THz. In this case increasing g pushes the oscillation frequencies of the system toward the peak of the SD rather than away from it, resulting in greater damping.

3.5 Concluding remarks

E have shown that, despite what one may naively expect, the coherent population oscillations between sites of a symmetric TLS can be protected from dissipative environmental decay by strong coupling to a bosonic SM. Interestingly

we have shown this to be possible for a SM that is far from resonant with the TLS and when it is all occurring at room temperature. The effect differs in its strength depending on the form of the SD used to characterise the environment, primarily their peakedness, which determines the strength of the initial decay and what frequency-change region must be traversed to avoid this. It is fair to note that not all of the SDs used exhibit this behaviour, specifically, the Ohmic SD is simply too broad to see any benefit from the oscillation frequency renormalisation caused by the TLS-SM coupling.

It is hoped that our work motivates the continued use and refinement of non-Markovian methods in OQS research towards simple, elegant descriptions of these very complex examples of quantum mechanical systems. If an open TLS is characterised by a SD like the forms displayed here, we hope we have shown that caution should be taken, when constructing such physical systems. Particularly strongly coupled vibrational modes that could cause oscillatory population dynamics to decay faster, or persist for longer, than desired should be taken account of. It should also be obvious that, conversely, such modes could be used as tools to faster equilibrate a system or enhance oscillatory dynamics. Customisation of SD forms with a process of reservoir engineering has been demonstrated [148] and one can imagine this forming a basis for future quantum device manufacturing, alongside our SM results, allowing designs of particular SD structures in order to elicit desired behaviours from a system.

Future work along this avenue will need to incorporate generalisations to allow considerations of non-symmetric and multiple modes. But despite the amount of work that can still be done, the findings in this chapter provide a tantalising look at the possibilities for novel quantum effects in complex open quantum systems and provide insight into their usefulness.

4

Entanglement transfer spin channel geometries

N Chapter 1 we introduced the notions of nitrogen vacancy centres (NVs) as qubits and the possibility of quantum state transfer (QST) through spin chains. We explained that realistic levels of environmental noise in NV implementations of QST processes would make the required fidelities impossible. However, these implementations have been considered for entanglement distribution schemes instead, where imperfect transfer can be dealt with using distillation techniques. Our focus in this chapter will be an investigation into two spin-channel geometries in an NV-diamond based implementation of an entanglement transfer scheme. Comparisons between the two geometries introduced will be motivated by manufacturing imperfections and how they affect the ability of the spin channel to distribute entanglement.

As we said in Chapter 1, entanglement is a vital resource and common theme throughout all quantum frontiers, so progressing our understanding of how to distribute it is of vital import. There has been consideration of entanglement distribution along spin chains [149–151] which has, for example, been extended to consider dual-rail configurations [152, 153]. Ladders of spin-1/2 particles have rarely been looked at in either QST or entanglement distribution contexts [154], possibly due to the fact that more spins for a given length of channel will result in higher decoherence across it. However, one might expect the extra connections between spins in a ladder to make it more robust to design imperfections. Considerations of physical implementations and the limits placed upon theoretical processes by physical constraints have been started, for instance with NV based systems [63]. Modelling of the behaviours of spin channel systems can help design efficient implementations, but the size of dissipative

systems we can simulate is often limited by the rapid computational scaling problem many quantum simulations suffer.

Fabrication of nitrogenic diamond spin-wire structures can be achieved through nitrogen ion implantation followed by an annealing stage to convert some of the nitrogen impurities to NVs [155, 156]. The conversion process is not perfectly efficient and the remaining impurities can be used as the spin channel [157]. Chemical vapour deposition can also be used to incorporate NVs in-situ during the growth process [158, 159]. Learning how the resulting system copes with missing impurities or a distribution of couplings due to position variation is clearly necessary to ensure devices operate as expected.

4.1 Our model

BUILDING on the work of Ping *et al.* with nitrogen impurity spin chains [63] which showed the implementation to be a viable entanglement distribution scheme, we will contrast the performance of spin chains and spin ladders with respect to faulty manufacturing processes. A schematic representation of the spin channel types we consider, chains and ladders, is shown in Fig. 4.1. A chain is a 1D structure, where as a ladder has two chains alongside each other that have adjacent spins coupled; we use 'channel' to refer collectively to chains and ladders. Whilst the figure shows our final, uniform coupling, model we shall start by introducing the fully generalised version.

An overview Hamiltonian of our system can be written,

$$H_{\text{S}} = H_{\text{NV}} + H_{\text{C}} + H_{\text{NV}-\text{C}}, \tag{4.1}$$

comprising NV, channel and interaction terms respectively. The NVs are denoted as sites $i = 0, N + 1$ in Fig. 4.1 and their Hamiltonian takes the form

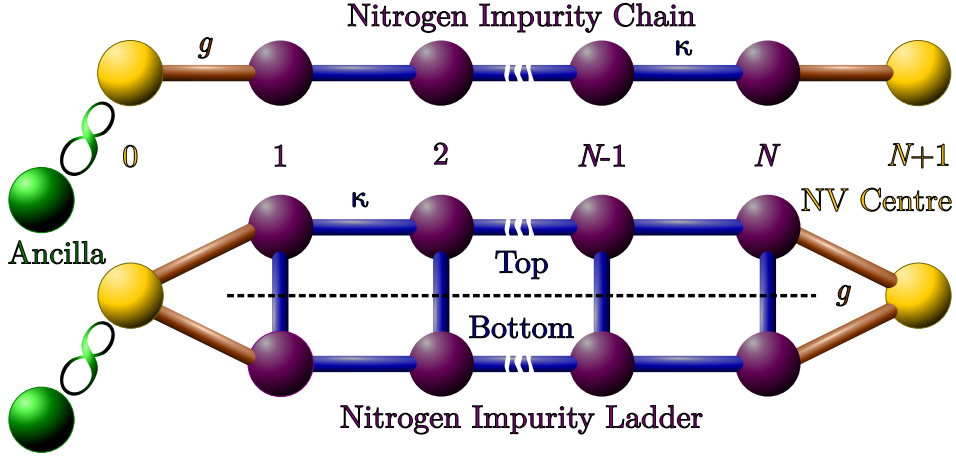$$H_{\text{NV}} = \frac{\varepsilon}{2} \left(\sigma_0^z + \sigma_{N+1}^z \right), \tag{4.2}$$

FIGURE 4.1: A schematic diagram of N-site nitrogen impurity chain and ladder channels connecting left and right NVs with the indicated couplings. An ancilla spin is initially entangled with the left NV. Intra-channel couplings are of strength κ and the NV-channel coupling strength is g. The index for the ladder spins (and operators) has both a site label $i \in \{1 \dots N\}$ and a top or bottom label as indicated.

where we have assumed an experimental method as described in Chapter 1 is being carried out to address two of the three electronic ground state levels as $|\uparrow\rangle$ and $|\downarrow\rangle$ leading to a Pauli matrix description of the Zeeman splitting, ε, with $\hat{\sigma}_z$. The nitrogen impurities forming the channel are present here as spin-1/2 electrons and their horizontal and vertical Hamiltonian components $\left(H_C = H_H + H_V\right)$ are

$$H_H = \sum_{i=1}^{N-1} \sum_{j \in \{B,T\}} \kappa_{i,j} \left(\sigma_{i,j}^+ \sigma_{i+1,j}^- + \text{H.c.} \right), \tag{4.3}$$

$$H_V = \sum_{i=1}^{N} \alpha_i \left(\sigma_{i,B}^+ \sigma_{i,T}^- + \text{H.c.} \right), \tag{4.4}$$

where i and j are the horizontal and vertical coordinates of the channel; i is a numerical index and j is B or T to the denote bottom and top sections of a channel. The intra-channel spin flip interactions are acted by the raising and lowering operators $\sigma^\pm$ and occur with coupling strengths of κ and α in the horizontal and vertical directions respectively. Finally the NV-channel interaction Hamiltonian,

$$H_{\text{NV-C}} = \sum_{j \in \{B,T\}} g_{0,j} \left(\sigma_0^+ \sigma_{1,j}^- + \text{H.c.} \right) + g_{N+1,j} \left(\sigma_{N+1}^+ \sigma_{N,j}^- + \text{H.c.} \right), \tag{4.5}$$

has a coupling strength between the NVs and the impurity channel of g which in general can be different at each end (and rail) of the channel, hence the subscripts.

All couplings are dipole-dipole in nature. These fully general Hamiltonian terms explicitly describe a ladder of N sites; to treat a chain we can simply omit H_{V} and truncate the summations over j in $H_{\mathrm{NV-C}}$ and H_{H}.

4.1.1 Our method

The ancilla present in the system does not interact with any other part of it and is present to enable us to initialise the Bell state $|\Psi^-\rangle = \frac{1}{\sqrt{2}}\left(|\uparrow\downarrow\rangle - |\downarrow\uparrow\rangle\right)$ with the left-most NV. All channel spins and the right-most NV are initialised $|\downarrow\rangle$. We then evolve the system through time and calculate the entanglement of formation, E, between the right-most NV and the ancilla to ascertain the degree to which the channel facilitates entanglement distribution [122]. As was introduced in Chapter 2, the entanglement of formation is a measure of the number of Bell pairs required for creation of a given state. Our goal is to assess which channel allows a maximal E under considerations of missing or randomly placed spins as would occur when manufacturing such a device.

To predict the behaviour of a physical implementation of this model we need to include the system's interaction with its environment. To do this we chose to employ a phenomenological Markovian master equation [63],

$$\frac{\mathrm{d}\rho(t)}{\mathrm{d}t} = -i\left[H_{\mathrm{S}}, \rho\right] + \gamma_{\mathrm{NV}}\left(\mathcal{D}[\sigma_0^x] + \mathcal{D}[\sigma_{N+1}^x]\right)\rho + \gamma_{\mathrm{C}}\sum_{i=1}^{N}\sum_{j\in\{B,T\}}\mathcal{D}[\sigma_{i,j}^x]\rho, \qquad (4.6)$$

as opposed to the form derived using a microscopic system-bath Hamiltonian in the previous chapter. The form in Eq. (4.6) is the same as defined in Chapter 2 for a Lindblad master equation with $\mathcal{D}[X]\rho = X\rho X^\dagger - \frac{1}{2}\{X^\dagger X, \rho\}$ dissipator terms; in this case we choose σ^x-type noise which will be justified in the next subsection. The Lindblad operators are present to describe dissipation acting on both NVs and all channel spins with associated decay rates, γ; the ancilla in our model does not undergo dissipation. The density matrix, ρ, in Eq. (4.6) is the density matrix of the full NV-ancilla-channel system and H_{S} is our Hamiltonian from Eq. (4.1).

4.1.2 Implementation

The process through which our model can be implemented in experiment is well documented [60, 61, 63, 160]. In this subsection we give a brief overview for a chain of impurities although it readily generalises to 2D [61]. If we consider a z-aligned magnetic field, B, where this direction is given by the axis of symmetry of the NV we can write Hamiltonians describing an NV or N defect in diamond

$$\widetilde{H}_{\mathrm{NV}} = D \left(\hat{S}^z \right)^2 + B \left(\mu_B g_e \hat{S}^z - \mu_n g_n \hat{I}^z \right) + A_{\mathrm{NV}} \hat{\mathbf{I}} \cdot \hat{\mathbf{S}}, \tag{4.7}$$

$$\widetilde{H}_{\mathrm{N}} = B \left(\mu_B g_e \hat{S}^z - \mu_n g_n \hat{I}^z \right) + \hat{\mathbf{S}} \cdot \mathbf{A}_{\mathrm{N}} \cdot \hat{\mathbf{I}}. \tag{4.8}$$

These are in terms of electronic, $\hat{\mathbf{S}}$, and nuclear, $\hat{\mathbf{I}}$, spin operators. For a nitrogen defect these spin operators interact via the hyperfine coupling tensor $\mathbf{A}_{\mathrm{N}}$ whereas for the NV they interact via the constant A_{NV}; interaction with the B field is along the z axis. The zero-field splitting of the NV is given by D, μ_B and μ_n are the Bohr and nuclear magnetons and the electron and nuclear g-factors are g_e and g_n.

Making the restrictions we explained in Chapter 1 to describe the NV in an $\{|\uparrow\rangle, |\downarrow\rangle\}$ basis we can approximate Eq. (4.7) as

$$\widetilde{H}_{\mathrm{NV}} \approx \frac{1}{2} \left(\omega_{\mathrm{NV}} \hat{\sigma}^z + A_{\mathrm{NV}} \hat{I}^z \hat{\sigma}^z \right), \tag{4.9}$$

where we have defined $\omega_{\mathrm{NV}} = D + \mu_B g_e B$ as the electronic Zeeman energy acting with a Pauli spin operator $\hat{\sigma}^z$. We have one hyperfine term, but the spin flip component of this has been neglected, along with a nuclear Zeeman splitting, because $A, \mu_n g_n B \ll \omega_{\mathrm{NV}}$. Similarly the spin-1/2 nitrogen impurity of Eq. (4.8) can be approximated,

$$\widetilde{H}_{\mathrm{N}} \approx \frac{1}{2} \left(\omega_{\mathrm{N}} \hat{\sigma}^z + A_{\mathrm{N}}^{\parallel} \hat{I}^z \hat{\sigma}^z \right), \tag{4.10}$$

this time defining $\omega_{\mathrm{N}} = \mu_B g_e B$ and picking out the parallel hyperfine component.

The dipolar coupling between neighbouring electron spins of each flavour is

$$\widetilde{H}_{\mathrm{NV,N}} = J_{\mathrm{NV,N}}\hat{\sigma}^z_{\mathrm{NV}}\hat{\sigma}^z_{\mathrm{N}} + \frac{1}{4}\left((2\omega_{\mathrm{NV}} \pm A_{\mathrm{NV}})\hat{\sigma}^z_{\mathrm{NV}} + \left(2\omega_{\mathrm{N}} \pm A^{\|}_{\mathrm{N}}\right)\hat{\sigma}^z_{\mathrm{N}}\right), \qquad (4.11)$$

$$\widetilde{H}_{\mathrm{N,N}} = J_{\mathrm{N,N}}\hat{\sigma}^z_{\mathrm{N}_1}\hat{\sigma}^z_{\mathrm{N}_2} + \frac{1}{4}\left(\left(2\omega_{\mathrm{N}} \pm A^{\|}_{\mathrm{N}_1}\right)\hat{\sigma}^z_{\mathrm{N}_1} + \left(2\omega_{\mathrm{N}} \pm A^{\|}_{\mathrm{N}_2}\right)\hat{\sigma}^z_{\mathrm{N}_2}\right), \qquad (4.12)$$

having assumed a linear chain along the z-axis which is a constraint that easily generalises to a 2D structure. We now acknowledge the relative orientations of the $I = 1/2$ nuclear spin with the inclusion of the $\pm$ hyperfine terms. Nitrogen impurities are not uniformly oriented in general and can take on one of four, tetrahedral symmetry-restricted, orientations. We have also defined the dipole coupling strength generally as

$$J_{\beta,\beta'} = \frac{\mu_0 g_e^2 \mu_B^2}{8\pi r_{\beta,\beta'}^3}, \qquad (4.13)$$

where $r_{\beta,\beta'}$ is the distance between spins β and β' and in which we have neglected that J should be negative as the global phase introduced by this is irrelevant. The system is subsequently driven globally with resonant fields,

$$\widetilde{H}_{\mathrm{fields}} = \sum_{i=0,N+1}\Omega_{\mathrm{NV}}\hat{\sigma}^x_i \cos\left[\left(\omega_{\mathrm{NV}} \pm \frac{A_{\mathrm{NV}}}{2}\right)t\right] + \sum_{i=1}^{N}\Omega_{\mathrm{N}}\hat{\sigma}^x_i \cos\left[\left(\omega_{\mathrm{N}} \pm \frac{A^{\|}_{\mathrm{N}_i}}{2}\right)t\right],$$
$$(4.14)$$

at all possible frequencies for the impurities, determined by nuclear orientation and hyperfine coupling. Our implementation Hamiltonian is now $\widetilde{H} = \widetilde{H}_{\mathrm{NV,N}} + \widetilde{H}_{\mathrm{N,N}} + \widetilde{H}_{\mathrm{fields}}$. Constants are chosen to ensure $|J_{\mathrm{N,N}}| \ll \Omega_{\mathrm{NV}}, \Omega_{\mathrm{N}} \ll \omega \pm \frac{A}{2}$. The driving term enables us to enter a rotating frame of $\widetilde{H}$ and perform a rotating wave approximation which eliminates the frequency, hyperfine and time dependent terms. We can then also rotate the basis such that $(x, y, z) \to (z, -y, x)$ and finally the system Hamiltonian described in this implementation becomes

$$\widetilde{H} = \sum_{i=0,N+1}J_{\mathrm{NV,N}}\hat{\sigma}^+_i\hat{\sigma}^-_{i+1} + \sum_{i=0,N+1}J_{\mathrm{N,N}}\hat{\sigma}^+_i\hat{\sigma}^-_{i+1} + \mathrm{H.c.}, \qquad (4.15)$$

with spin flip operators $\hat{\sigma}^{\pm} = \hat{\sigma}^x \pm i\hat{\sigma}^y/2$. The couplings $J_{\beta,\beta'}$ in general vary with the index of their associated summation; a labelling index is explicitly omitted although its position within the sum is intended to imply it. Tuning of the driving magnitude

Ω_{NV} allows control of the coupling $J_{\mathrm{NV,N}}$.

The basis rotation $(x, y, z) \rightarrow (z, -y, x)$ means modelling of physical spin-flip (phase-flip) noise, characterised by a T_1 (T_2) coherence lifetime, requires $\hat{\sigma}^z$ ($\hat{\sigma}^x$) Lindblad operators. It has been shown, for these spin channel entanglement distribution systems, that T_2 processes are the more destructive type of noise [63] and so it is on these we focus; hence our definition in Eq (4.6). The $\hat{\sigma}^x$ Lindblad operators we use lead to spin flips in the computation basis, but correspond to T_2 phase flip processes on the physical spins.

4.2   Computational solution

DESPITE using a spin conserving Hamiltonian and introducing only one spin in our initial condition in order to study the full dissipative dynamics we are required to include the full Hilbert space as $\mathcal{D}[\sigma^x]$ causes transitions beyond a single excitation subspace. This necessitates two computational methods: 1) direct solution of the differential equation in Eq. 4.6 [146] and 2) a matrix product operator (MPO) formulation [108, 110]. For $N < 5$ a powerful desktop machine can satisfy the memory requirements of the direct solution, integrating the full-matrix differential equation system. Again, as with the previous chapter, QuTiP is employed, making use of its specifically designed structures for handling quantum objects and operations.

For $N \geq 5$ an MPO based high performance cluster implementation enables more efficient solution but which for $N < 5$ is slower than direct solution. In Chapter 2 we detailed the definition and evolution of MPOs in terms of spin-1/2 chains, in this work an extension was required in order to deal with our spin-1/2 ladders. The Pauli levels for one spin, $\uparrow$ and $\downarrow$, generalise to $\uparrow\uparrow$, $\uparrow\downarrow$, $\downarrow\uparrow$ and $\downarrow\downarrow$ for two spins on one site which is represented in Fig. 4.2. Our state, including the NV centres and ancilla, is described by

$$\rho = \sum_{\{n_i\}} D_{n_0, \ldots n_{N+1}} n_0 \otimes \ldots \otimes n_{N+1}. \tag{4.16}$$

The complete basis describing each two spin site $\{n_i\}$ contains fifteen matrices:

$$
n_1 = \begin{pmatrix} 0 & 1 & 0 & 0 \\ 1 & 0 & 0 & 0 \\ 0 & 0 & 0 & 0 \\ 0 & 0 & 0 & 0 \end{pmatrix}, n_2 = \begin{pmatrix} 0 & -i & 0 & 0 \\ i & 0 & 0 & 0 \\ 0 & 0 & 0 & 0 \\ 0 & 0 & 0 & 0 \end{pmatrix}, n_3 = \begin{pmatrix} 1 & 0 & 0 & 0 \\ 0 & -1 & 0 & 0 \\ 0 & 0 & 0 & 0 \\ 0 & 0 & 0 & 0 \end{pmatrix},
$$

$$
n_4 = \begin{pmatrix} 0 & 0 & 1 & 0 \\ 0 & 0 & 0 & 0 \\ 1 & 0 & 0 & 0 \\ 0 & 0 & 0 & 0 \end{pmatrix}, n_5 = \begin{pmatrix} 0 & 0 & -i & 0 \\ 0 & 0 & 0 & 0 \\ i & 0 & 0 & 0 \\ 0 & 0 & 0 & 0 \end{pmatrix}, n_6 = \begin{pmatrix} 0 & 0 & 0 & 0 \\ 0 & 0 & 1 & 0 \\ 0 & 1 & 0 & 0 \\ 0 & 0 & 0 & 0 \end{pmatrix},
$$

$$
n_7 = \begin{pmatrix} 0 & 0 & 0 & 0 \\ 0 & 0 & -i & 0 \\ 0 & i & 0 & 0 \\ 0 & 0 & 0 & 0 \end{pmatrix}, n_8 = \begin{pmatrix} 0 & 0 & 0 & 1 \\ 0 & 0 & 0 & 0 \\ 0 & 0 & 0 & 0 \\ 1 & 0 & 0 & 0 \end{pmatrix}, n_9 = \begin{pmatrix} 0 & 0 & 0 & -i \\ 0 & 0 & 0 & 0 \\ 0 & 0 & 0 & 0 \\ i & 0 & 0 & 0 \end{pmatrix}, \qquad (4.17)
$$

$$
n_{10} = \begin{pmatrix} 0 & 0 & 0 & 0 \\ 0 & 0 & 0 & 1 \\ 0 & 0 & 0 & 0 \\ 0 & 1 & 0 & 0 \end{pmatrix}, n_{11} = \begin{pmatrix} 0 & 0 & 0 & 0 \\ 0 & 0 & 0 & -i \\ 0 & 0 & 0 & 0 \\ 0 & i & 0 & 0 \end{pmatrix}, n_{12} = \begin{pmatrix} 0 & 0 & 0 & 0 \\ 0 & 0 & 0 & 0 \\ 0 & 0 & 0 & 1 \\ 0 & 0 & 1 & 0 \end{pmatrix},
$$

$$
n_{13} = \begin{pmatrix} 0 & 0 & 0 & 0 \\ 0 & 0 & 0 & 0 \\ 0 & 0 & 0 & -i \\ 0 & 0 & i & 0 \end{pmatrix}, n_{14} = \frac{1}{\sqrt{3}} \begin{pmatrix} 1 & 0 & 0 & 0 \\ 0 & 1 & 0 & 0 \\ 0 & 0 & -2 & 0 \\ 0 & 0 & 0 & 0 \end{pmatrix}, n_{15} = \frac{1}{\sqrt{6}} \begin{pmatrix} 1 & 0 & 0 & 0 \\ 0 & 1 & 0 & 0 \\ 0 & 0 & 1 & 0 \\ 0 & 0 & 0 & -3 \end{pmatrix},
$$

plus the identity matrix. This matrix basis is a generalisation from the Pauli matrices (three matrices plus the identity) for a one spin system to a two spin, four level, system [119]. They allow for a complete description of such a four level system in the same way that the Pauli matrices form a complete basis for a two level system and the Gell-Mann matrices can completely describe a three level system [118]. This is represented schematically in Fig. 4.2(a) for an $N = 3$ example case where the colours have the same meaning as they did in Fig. 4.1. The final NV centre is paired with a dummy, non-interacting spin in order for basis-size consistency. The diagram in Fig. 4.2(b) is

a visualisation of the same ladder, now a chain of four level systems as per our basis description. As MPO solutions for the ladder are the computational upper limit we use the same description in Eq. 4.16 for a chain, but we use the relevant reduced Hamiltonian and effectively treat each site as a chain spin and an uncoupled dummy spin.
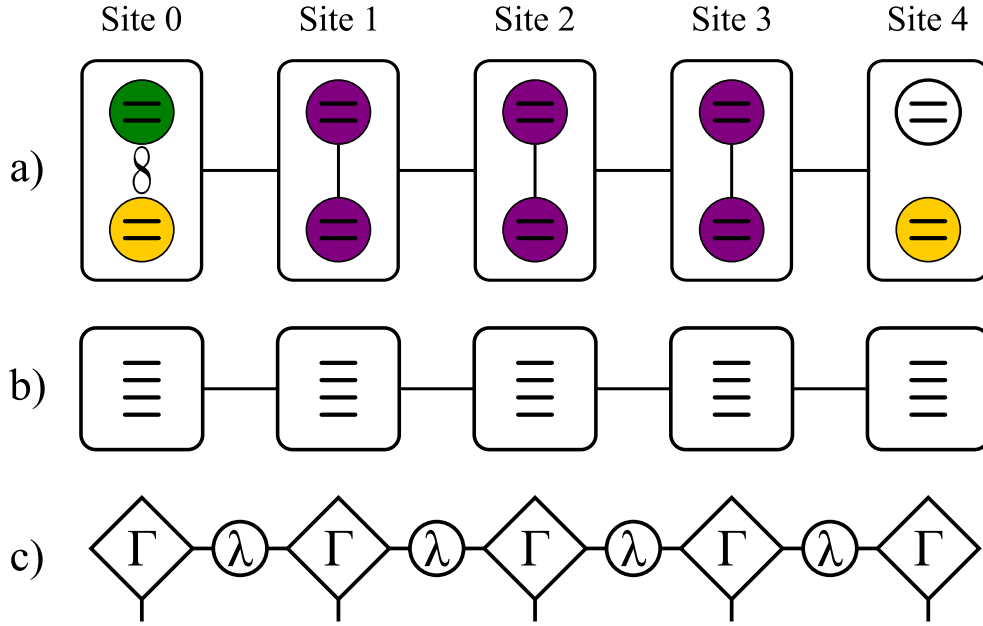

FIGURE 4.2: Schematic representations of an $N = 3$ system for solution with an MPO method in terms of four level sites. a) Colour labelling is the same as in Fig. 4.1; ancilla green, NVs yellow, nitrogen impurities purple. The white spin represents a computational dummy spin required to describe the final NV as a four level site. b) Considering the effective sites as containing a single four level spin with energy levels and transition rates determined by the two level spin definitions. c) The MPO formulation of the system shown, as can be described by Eq. (4.18).

The MPO methodology that has been explained previously in Chapter 2 can be applied directly to our problem. For instance, the on-site H_V and H_{NV} components could be thought of as describing transitions between levels rather than a hopping between spins and the inter-site H_H and H_{NV-C} can be thought of as interactions between a pair of four level spins. We still can decompose our state into

$$D_{n_0,\dots n_{N+1}} = \sum_{\{\nu_k\}} \Gamma^{[0]n_0}_{\nu_0} \lambda^{[0]}_{\nu_0} \Gamma^{[1]n_1}_{\nu_0\nu_1} \lambda^{[1]}_{\nu_1} \times \dots \times \Gamma^{[N]n_N}_{\nu_{N-1}\nu_N} \lambda^{[N+1]}_{\nu_N} \Gamma^{[N+1]n_{N+1}}_{\nu_N} \qquad (4.18)$$

(shown diagrammatically in Fig. 4.2c) and we can still evolve this in time with the time evolving block decimation (TEBD) method. The code used for this work was

built on and modified from already tested TEBD MPO code [161, 162]. It required adaptation to incorporate our four level site master equation and our required flexibility to define a non-uniform array of sites to consider the possibility of a missing spin.

4.3 Results

E have so far presented a theoretical Hamiltonian we will study and a physically implemented Hamiltonian but we have not quite unified these two descriptions yet. We will initially employ a uniform coupling model which allows us to define $g_{0,j} = g_{N+1,j} = g_j = g = J_{\mathrm{NV,N}}$ and $\alpha_i = \kappa_{i,j} = \kappa = J_{\mathrm{N,N}}$. Now we can go from a statement about physical spin separations and J to a numerical value of the parameters g and κ. This results section starts with a look at what effect the ratio and value of these parameters has on transferred entanglement followed by a discussion of the interplay between decay rate and spin separation. Those starting points allow us to find what parameter values are physically appropriate and will provide good entanglement transfer in our nitrogen spin channel systems. We then move to considering two types of manufacturing induced imperfections in these channels and how they affect their entanglement transfer capability.

4.3.1 Spin coupling and NV splitting

In Fig. 4.3 we show what effect different values of the NV energy splitting, ε, have on the maximum entanglement of formation, E_{Max}, transferred for various values of the ratio g/κ. The system from which the results in this figure were obtained is an $N = 3$ ladder (like that shown in Fig. 4.2) where the NVs are isolated from the environment, $\gamma_{\mathrm{NV}} = 0$, and the ladder spins are subjected to a decay rate of $\gamma_{\mathrm{C}} = 0.01$ kHz. These rates are not motivated by experiment, rather they allow the demonstration of the results in Fig. 4.3; realistic rates are larger and would serve to reduce E_{Max}. The eigenvalues depicted are those of the $N = 3$ ladder and it is clear for low values of g/κ that these provide the best route for entanglement transfer. However it is also clear that as the ratio increases the magnitude of the transferred entanglement improves

and the dependence of E_{Max} on ε becomes much less well defined until by $g/\kappa \sim 1$ there is very little dependence left. The jagged, noisy nature of the curves is partly due to the coarse graining of the simulations in terms of both time and ε.
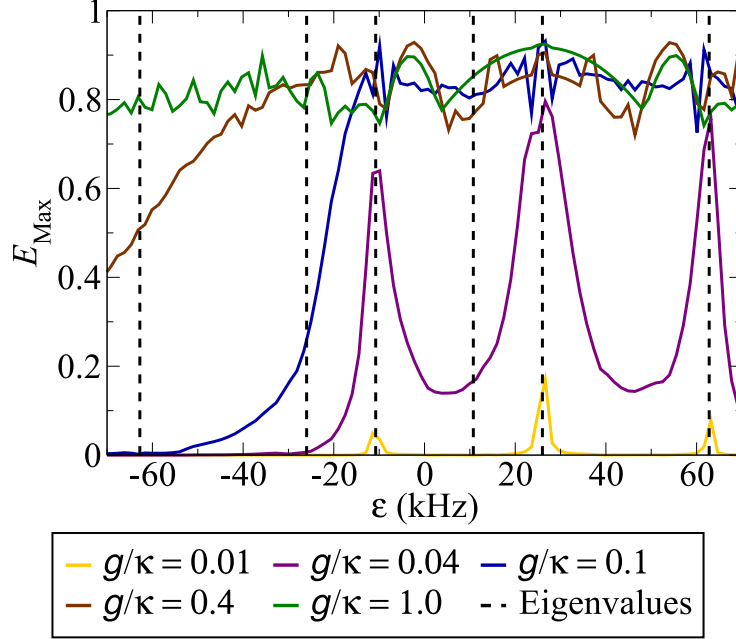

FIGURE 4.3: Entanglement of formation maxima obtained from simulations sweeping ε at various values of g/κ; for an $N = 3$ ladder with no NV environmental decay and $\gamma_{\text{C}} = 0.01$ kHz. The tendency for a weak coupling ratio to enhance eigenmode transfer is clear, with eigenvalues included as dashed lines. There is a near performance independence with respect to ε for a strong coupling ratio.

As we said in Chapter 1, dark spin chain QST schemes benefit from weak coupling between NVs and the spin chain as stronger coupling leads to interference effects from multiple eigenmode transmission reducing the fidelity of transfer. A QST plot for similar circumstances as Fig. 4.3 (with maximum fidelity as its measure of success) would show poor results for large g/κ as competing eigenmode pathways interfered. This means for entanglement transfer our optimal values of ε, g and κ are different compared to if we were trying to optimise QST. We are free of the need for high fidelity transfer as we are already performing dissipative transfer which will require subsequent distillation. Therefore a large coupling ratio is beneficial as it results in a higher transfer speed. We choose $g/\kappa = 1$ and at this value, due to the nature of the dependence between ε and E_{Max} we arbitrarily choose to set $\varepsilon = 0$. We also now fix the NV decay rate as $\gamma_{\text{NV}} = 1/T_2 = 0.1$ kHz [58]; channel decay rate is to be studied further in the next subsection.

4.3.2 Channel length

The actual values of g and κ depend on spin separation and so, if we fixed total channel length, varying the number of spins present would change them. In Fig 4.4 we present E dynamics illustrating the effect of varying N for one value of the channel decay (a restriction which will be lifted in the next subsection); the number of spins in a channel increases from right to left. The NV separation is fixed at $40\,\text{nm}$ which we believe to be physically reasonable [163, 164] in terms of the placement accuracy and optical resolution limits. We chose to stop at $N = 12$ due to physical limitations of consistently placing impurities with $r < 3$ nm. Also at this point we already have 27 spins (a Hilbert space with dimensionality greater than 10^8) and we are approaching computational limits; solutions with more spins in a channel require smaller time steps and increased MPO bond dimension to achieve convergence.
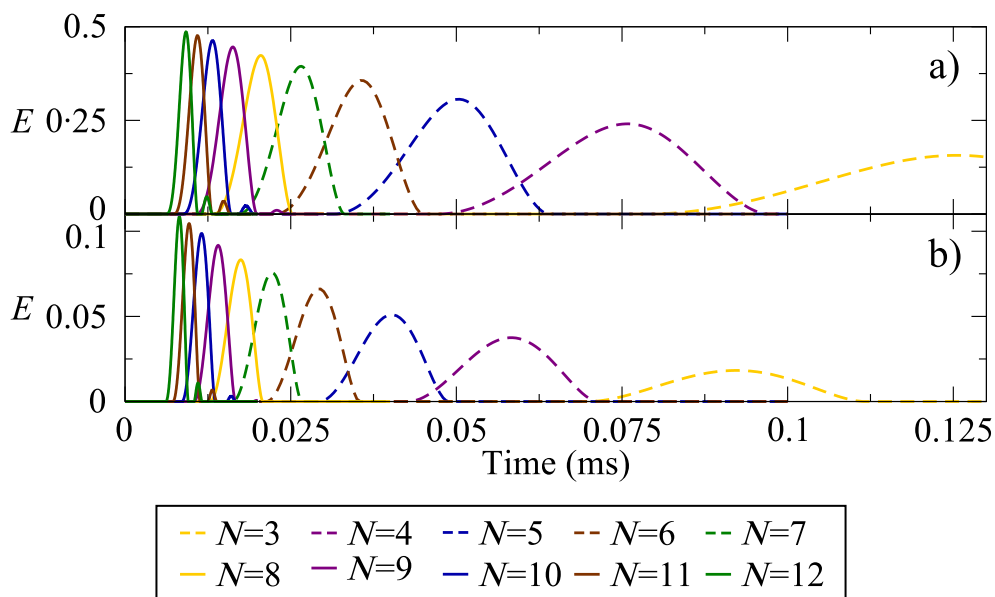
FIGURE 4.4: Dynamics of the entanglement of formation, E, for increasing number of spins in the channel N (right to left) in (a) chains and (b) ladders between NVs spaced 40 nm apart, and channel decay rate $\gamma_{\text{C}} = 2$ kHz.

A fixed NV separation means an increasing impurity density which in turn implies g and κ must also increase and in Fig. 4.4(a) and (b) it is clear this increases the speed of entanglement distribution. Further, for this value of $\gamma_{\text{C}} = 2$ kHz, the long transfer time for few-spin channels is clearly seen to negate the benefits of fewer

spins undergoing decay, whereas the many-spin channels are more robust exhibiting increased entanglement transferral. The ladders in Fig. 4.4(b) do experience more decay pathways due to having twice as many spins for any given N and therefore have a smaller magnitude of E compared to the chains in Fig. 4.4(a). There is a speed advantage of using ladders though when comparing site number; a given coupling strength (as this is varying with number of spins) elicits faster entanglement transfer through a ladder than a chain.

4.3.3 Channel decay rate

The behaviours in Fig. 4.4 are however not global, they depend quite strongly on γ_C and in an interesting way. In Fig. 4.5 we extract the maxima for the chain and ladder E dynamics for a range of γ_C, with strongest decay at the top, and highlight the N-site channel that performs the best at each strength. There is a clear interplay between spin number and decay rate with a transition present whereby increasing noise changes the optimal N; this is due to competition between the spin-number dependent total decay rate and the transfer rate.
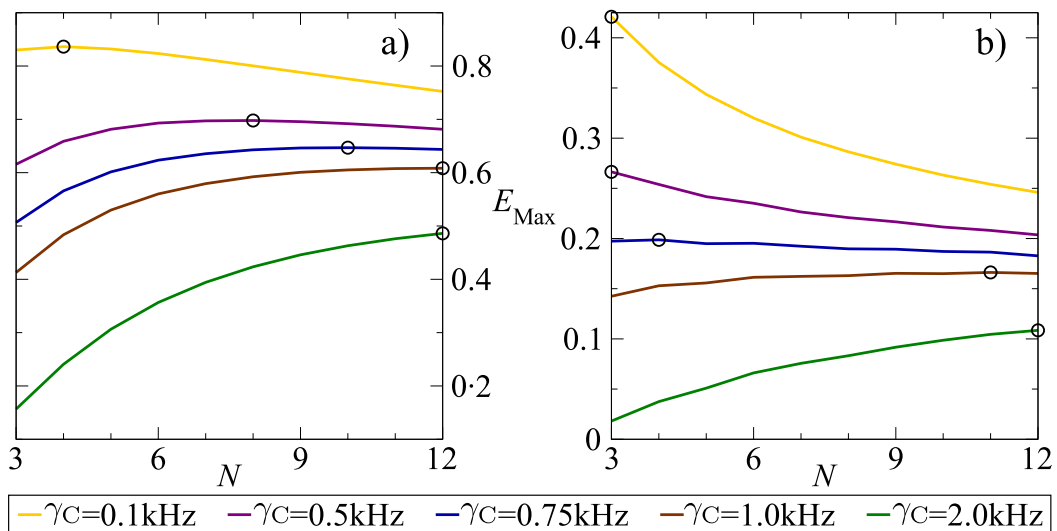
FIGURE 4.5: The maximum E, for (a) chains and (b) ladders, with different γ_C values (increasing from top to bottom) as a function of N between 40 nm spaced NVs. The circles denote the N that maximizes E_{Max}.

A large decay rate means that the few-spin channels, which have slower transfer rates (as shown in Fig. 4.4), are subject to decay for longer before the transfer can

complete thus reducing its fidelity. Conversely, smaller γ_C leads to few-spin channels being superior as their slow transfer is not as adversely affected as the many-spin channels undergoing small but numerous decay processes. The difference between what constitutes a many- or few-spin channel and weak or strong decay for the two channel types is seen between the two panels in Fig. 4.5 as the different pattern of maximal Ns for the γ_C simulated; again we see the weaker E for ladder systems.

For subsequent results we choose the experimentally motivated value of $\gamma_C = 2$ kHz [165, 166] which allows us to demonstrate interesting results. We have also shown in Figs. 4.4 and 4.5 that at this decay rate the couplings associated with $N = 12$ provide an optimal distribution of entanglement considering a much smaller spin separation begins to go beyond physical placement limits. With this in mind we relax our restriction of fixed NV separation and instead fix the spin separation at the $N = 12$ value of $r = 40/13$ nm and hence $g = \kappa \sim 0.9$ MHz from Eq. (4.13). However the tasks we report in the coming sections would be impossible to simulate with $N = 12$ channels; we do use the $N = 12$ coupling parameters but with shorter channels.

4.3.4 Missing spins

We now consider the idea that a manufactured channel may have spins missing as a result of the processes for placing the nitrogen impurities. To do this we imagine a process has associated with it a probability P per spin that said spin will be missing. It is immediately obvious one spin missing from a nearest neighbour interacting chain constitutes a catastrophic break, rendering distribution impossible. As one can see from the selection of configurations present in Fig. 4.6 this is not generally the case for a ladder.

In Fig. 4.6 we clearly have revivals where before, in Fig. 4.4, we see none. Actually there were revivals in the results in Fig. 4.4 but the curves were truncated past the first peak to enable clear comparisons. The discarded parts of Fig. 4.4 contained no revival peaks that rivalled the initial peak whereas we can see in Fig. 4.6 that the $N = 3$, 4 and 6 configurations actually have their maxima occur as a revival. The strong revivals are in part due to the configurations themselves; the NV coupling into and out
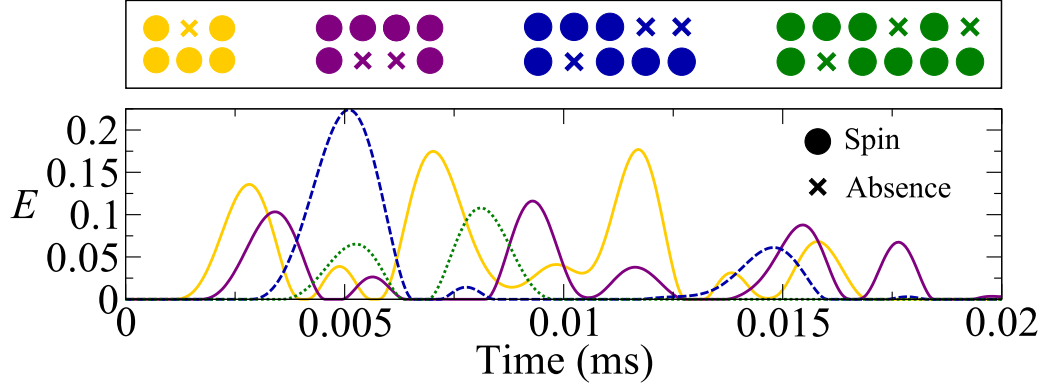
FIGURE 4.6: Dynamics of E for various impurity ladder configurations with some spins absent. The simulated configurations are schematically illustrated above with crosses to denote missing spins.

of the channel is presumably now not as symmetric as it was with perfect channels due to the nature of the channel's eigenstates, hence there are competing oscillatory transport processes which lead to complex dynamics. The coupling strength-decay rate regime we are in also plays a part in causing revivals; complex dynamics can occur before the decay processes have destroyed the entangled state. For fixed coupling strength, as we have here now, the transfer time of longer channels increases and this is seen in the behaviours of the first peak position in Fig. 4.6. While this is in contrast to what we observed earlier it is understandable now that we are not increasing the coupling strength with the number of spins in a channel, which is what was driving the speed increase in Fig. 4.4.

It should be clear though that looking at a handful of isolated configurations does not a conclusion make, we need to assess the behaviour of a given channel length based on all of the possible configurations. To do this we must calculate the average maximum entanglement of formation

$$\langle E_{\text{Max}}\rangle(P) = \sum_{\text{c}} P^{m_{\text{c}}}(1-P)^{M-m_{\text{c}}} E_{\text{Max,c}}, \tag{4.19}$$

which includes a sum over all configurations, c, of their maximum E, taking into account a weighting based on the number of missing spins, m_{c}. This is a function of the probability per spin, P, of an absence which we introduced earlier and M is the total number of possible spins (so N or $2N$ depending on channel geometry). For any given channel length we can reduce the number of configurations we have to calculate

by taking advantage of symmetry and the presence of catastrophic breaks. Obviously if we can diagnose a catastrophic break in a configuration we can automatically have it contribute an $E_{\text{Max}} = 0$; to this end for any chain we only need calculate the perfect case. For ladders, keeping track of any configuration that is symmetric about the length axis means we can attribute the result of that previously simulated symmetry partner to the calculation of Eq. (4.19).

A graph showing the results of Eq. (4.19) for channels $N = 3$ to 6 can be seen in Fig 4.7(a) where we can see the intuitive result that a higher P causes a reduction in $\langle E_{\text{Max}} \rangle$. What is immediately noticeable is the more severe gradient which occurs for the chain geometry at low probabilities showing that indeed chains are affected strongly by the chance of spins being missing. It appears that ladders are more robust to increasing P, but we do still have the feature that ladders are more strongly affected by environmental noise meaning their low-P $\langle E_{\text{Max}} \rangle$ are reduced compared with the chains.

To help ascertain which channel geometry performs best for a given length and P Fig 4.7(b) shows the ladder:chain ratio of $\langle E_{\text{Max}} \rangle(P)$. On this figure we have marked the value of 1 which corresponds to equal performance and above which is a region where P enables ladders to outperform chains of the same length. There is clearly a regime then in which it would be sensible to construct ladders if your manufacturing process was suitably poor at guaranteeing spin presence. It is also fair to state that this regime occurs at a fairly high P which is a surprising result as one might reasonably expect the multiple transfer routes through a ladder to allow for better resilience. Different coupling strength regimes were investigated for an improvement here and although stronger couplings do show increased environmental decay robustness for the ladder, the chain similarly exhibits less decay so the P cross over does not show much improvement.

It would obviously be interesting to carry on to larger N but we are somewhat restricted by the computational resources required to simulate the increasing number of configurations that are present, even after considering symmetries and catastrophic breaks. The trend in Fig 4.7 appears to show (apart from the very short $N = 3$ case) larger N ladders outperforming their chain counterparts earlier; a promising result,
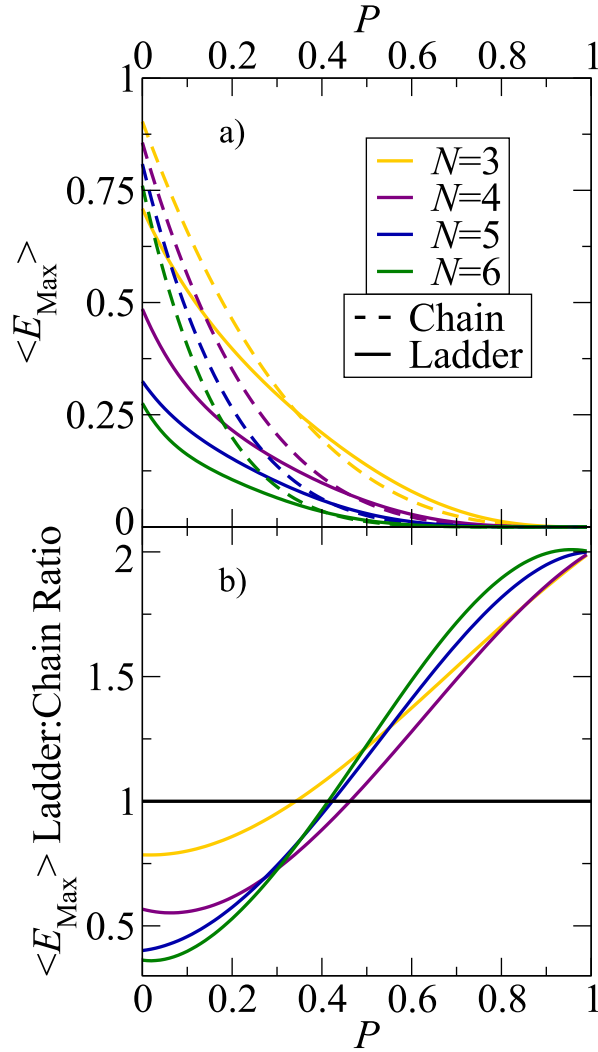
FIGURE 4.7: a) The actual values of $\langle E_{\text{Max}} \rangle$ with increasing channel length from top to bottom. b) The ratio of the values of $\langle E_{\text{Max}} \rangle$ for the ladder and chain as a function of the probability for each spin to be missing, P, for a variety of channel lengths N.

but there clearly will come a point at which the channel is too long to distribute a finite amount of entanglement. The $N = 3$ ladder appears to benefit from some short channel effect, but the required NV separation to achieve the same coupling used here is approximately 12 nm which is not far enough to ensure the NVs are well resolved qubits.

Although the large P requirement for superior ladders means low $\langle E_{\text{Max}} \rangle$ when comparing like-Ns, if we look more generally at Fig 4.7(a) we can see an $N = 6$ chain is outperformed by an $N = 4$ ladder at relatively low-P. This has an interesting implication: rather than manufacturing an $N = 6$ chain, an 8 spin, $N = 4$ ladder device would give more reliable entanglement generation for these modest P values.

As we saw earlier, for a given coupling strength ladders facilitated faster transfer, this observation reinforces the argument for choosing an $N = 4$ ladder over an $N = 6$ chain. We must of course be careful with such a comparison for as it currently stands the spatial distance between the $N = 4$ ladder-connected qubits is less than the $N = 6$ chain-connected case (as we have fixed impurity separation).

4.3.5 Placement disorder

One other way that a channel can deviate from perfection is variation in the impurity position. We investigate this effect by introducing random couplings about our ideal $\kappa_0 = \kappa(r = 40/13 \text{ nm})$ following a log-normal distribution [167]. The log-normal distribution was chosen as it has a long tail for $\kappa > \kappa_0$ and goes to zero at $\kappa = 0$ which describes the variation in coupling associated with an uncertainty in a spin's placement. In Fig. 4.8 we sketch the form of the log-norm distribution for three example standard deviations, σ. A $\sigma = 0$ case would correspond to a discrete line at $\kappa = \kappa_0$.
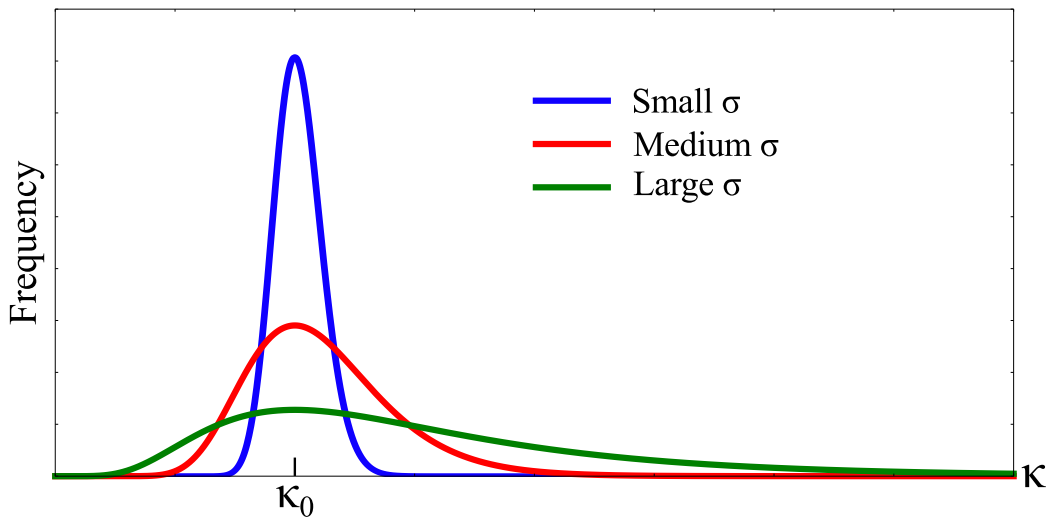
FIGURE 4.8: A sketch showing three instances of a log-normal distribution for differing standard deviation, σ. The frequency axis refers to the frequency with which a value of κ would be generated.

In Fig. 4.9(a) the converged arithmetic mean of E maxima from the sampled coupling dynamics, $\overline{E_{\text{Max}}}$, is shown for increasing σ of the log-normal distribution. Channel lengths of 3 and 4 are used as bigger channels, although requiring fewer disorder samples, do take longer to simulate per sample and thus present a computational restriction. A broader distribution of couplings can be seen, in Fig. 4.9(a), to lead to a

reduction in $\overline{E_{\mathrm{Max}}}$ and this correlation is repeated across both lengths and geometries. This type of manufacturing error however does not show a region where a chain is outperformed by a ladder of the same length. There is an interesting outcome though which is presented in Fig. 4.9(b) where we plot the deviation of $\overline{E_{\mathrm{Max}}}$ from its 'best case' uniform coupling value. Here we see the response to a broadening distribution is remarkably similar for both geometries of a given length and the longer, $N = 4$ channels seem more robust.
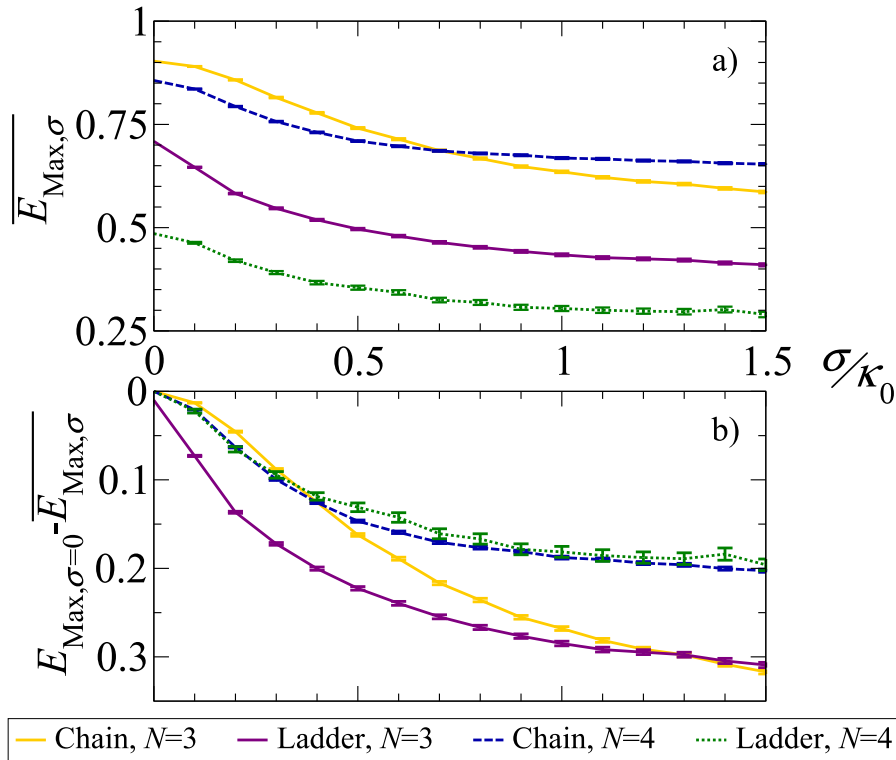
FIGURE 4.9: a) Disorder averaged $\overline{E_{\mathrm{Max},\sigma}}$ for randomly assigned intra-channel coupling strengths generated using a log-normal distribution of standard deviation σ in units of the ideal coupling κ_0. The standard error of the mean was used to calculate the error bars. b) The difference between the ideal $\sigma = 0$ case and its disordered equivalent. Each point was averaged over k disorder realisations where $k = 12000$ for the $N = 3$ chain, $k = 10000$ for the $N = 4$ chain, $k = 4000$ for the $N = 3$ ladder and $k = 600$ for the $N = 4$ ladder.

4.4 Concluding remarks

PON first consideration one would imagine that a ladder of spins, when compared with a chain, would be a more robust entanglement distribution channel due to them having inherently more transfer routes. Indeed, we have shown regimes

and scenarios in which ladders can outperform chains. In considerations of missing spins and imperfect placement we can see ladders might be as, or even more robust than chains to increasing error rates, but often the reduced fidelity associated with more decay pathways often makes ladder geometries appear to perform worse than their chain counterparts. However, given a sufficiently high missing spin rate, ladders do become the better candidate. It would be very interesting to combine studies of missing spin rates and positioning accuracy. This sort of study is especially compelling since longer channels seem more robust against coupling variation and there was the observation of ladders outperforming longer chains when spins are (possibly) absent. Unfortunately the current computation limitations make any study into combining these effects impossible; vast resources would be required to consider all configurations of missing spins and sample each of them hundreds or thousands of times to converge distributed coupling dynamics.

We have however already pushed computational limits with this work; our MPO implementation of a four level site has allowed solution of much larger Hilbert spaces than is possible with direct solution. An interesting next step would be to consider beyond nearest neighbour only interactions. Whilst this should make both kinds of channel more robust against defects it would also allow chains to function when catastrophic breaks are present, possibly causing them to improve in the strong imperfection limit. One could also consider how correlated noise or the introduction of non-Markovian effects of the environment might affect these sort of spin channel entanglement transfer systems. As ladders have more spins for any given N the dephasing processes have more of an effect on them than chains and the concept of the environment resupplying a channel with information rather than simply destroying it is an interesting one.

It is clear from this work that ladders and chains both exhibit interesting behaviours and have their own strengths and weakness when used in an NV-impurity entanglement distribution scheme. We have also shown that the interplay between dephasing and channel length doesn't necessarily make a higher decay rate a bad

thing. There are clear choices that can be made based on the interplay between environmental decay, manufacturing efficacy and channel parameters when implementing these entanglement distribution architectures.

5

Entanglement routing

AFTER thinking about nitrogen vacancy entanglement distribution implementations in the last chapter we will now look at an extension of the distribution concept but without direct consideration of an implementation scheme. In this chapter we present our exploration of the idea of routing entanglement. First it is important to be clear about the terminology of quantum routing. Much like classical information routing which allows the Internet to function, quantum routing in general describes the process of directing information along different channels. It is however a reasonably new concept and as such has not had a formal definition accepted *en masse*. Currently there are two main schools of thought when it comes to what is meant by a quantum router.

The first can be thought of as a full quantum conversion of the classical routing procedure. In classical routing an input piece of information enters the routing device and is output to a desired destination based upon the instructions from some control signal. Lemr *et al.* considered quantum routing in terms of a single photon, linear optics implementation with two output channels [168]. They argue that a router can only be fully quantum if it satisfies five criteria:

1. The control signal (as well as the input) must be a quantum entity.

2. The input state must be unchanged by the routing process upon output.

3. However, the output state must exist in a superposition of the possible output channels.

4. The router must not rely on postselection of the output and if the process is probabilistic in nature, measurement via the control state should be employed to judge success.

5. For resource efficiency there should be a need for only one control qubit per routing operation.

There are schemes that exist which satisfy all criteria in this list [169–171].

The other idea about what quantum routing is focusses on the distribution of a particular quantum state to one of multiple locations, i.e. no superposition across all output locations. The most common instances of this interpretation are in single photon routing [172–174] or abstract theoretical network models [175–177]. There are also some spin network proposals [82, 178] which consider chains or rings exploiting eigenmode tunnelling [179, 180] (which we introduced in Chapter 1.2.2) and pulses, buffering or other coupling manipulation to control state propagation [178, 179, 181]. Our proposal is to use a rectangular spin network for entanglement routing where, beyond initial positioning controls, all that is required for destination selection is a modification of the sending spin's energy splitting. We will show here that, with this minimal control scheme, routing of a single entanglement state is possible as is routing multiple states simultaneously.

5.1 Spin network router

HE problem we wish to investigate in general is illustrated in Fig. 5.1: a 2D Cartesian network of spin-1/2 sites form the functional basis of our routing device and we couple to this network a sender (or senders) and multiple receivers at positions to be specified later. The sender is initially entangled with an ancilla that (like in the last chapter) is decoupled from the dynamical evolution of the system and allows us to judge the success of routing. We choose for the network coordinates (1,1) to describe the bottom left site and (N_x, N_y) the top right site.

We impose uniform nearest neighbour couplings within the network and assume the same form for the external sender and receiver spins coupling to the network. This
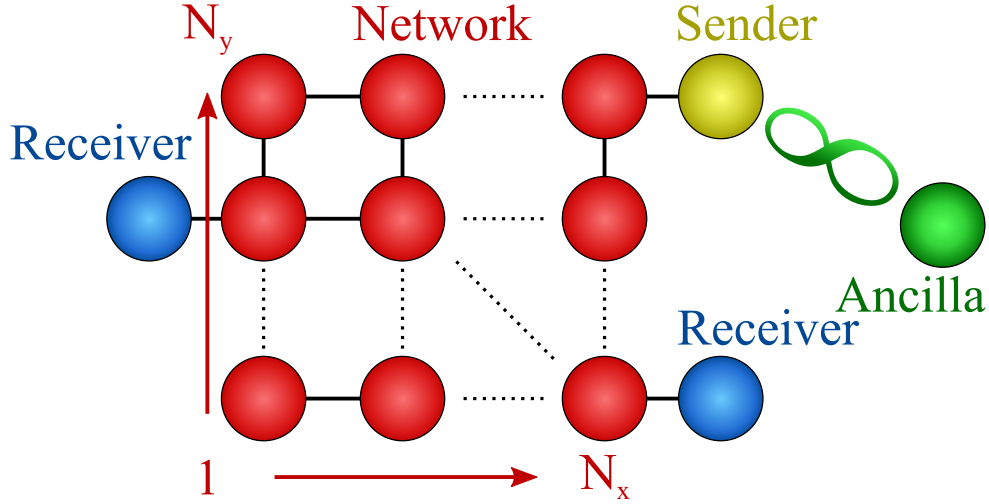
FIGURE 5.1: A representation of the model we are considering where a network of $N_{xy} = N_x \times N_y$ spin-1/2 spins allows transport of entanglement from a sender to one of multiple receivers.

allows us to write the Hamiltonian

$$H = H_\text{N} + H_\text{S} + H_\text{R}, \tag{5.1}$$

where the first term describes the network and last two describe the sender(s) and receivers and their interaction with the network. The network Hamiltonian is given by

$$H_\text{N} = \kappa \sum_{n,j} \left(\sigma_n^+ \sigma_j^- + \text{H.c.} \right), \tag{5.2}$$

with the n subscript selecting each site and the j summation covering that site's nearest neighbours within the network. The interaction strength is given by κ and we have neglected any spin splitting terms. We present the sender term for a general number of spins (however will restrict our investigation to one or two senders):

$$H_\text{S} = g \sum_s \left(\sigma_s^+ \sigma_{n_s}^- + \text{H.c.} \right) + \sum_s \varepsilon_s^\text{S} \sigma_s^Z, \tag{5.3}$$

where s is an index labelling the sender and the n_s subscript references the network coordinate to which the sender couples. Here we do include a spin splitting term with energy ε_s^S and this will be the only thing we need to vary in a defined system to achieve routing. To be clear, by a defined system (or system definition) we mean a fixed network size, sender-receiver placements, coupling strengths and receiver spin

splittings. Finally the receivers are described by the similar Hamiltonian

$$H_{\mathrm{R}} = g \sum_r \left(\sigma_r^+ \sigma_{n_r}^- + \mathrm{H.c.} \right) + \sum_r \varepsilon_r^{\mathrm{R}} \sigma_r^Z; \tag{5.4}$$

the $\varepsilon_r^{\mathrm{R}}$ would remain fixed for a defined system and n_r denotes the coordinates in the network to which each receiver couples.

We define a Lindblad form master equation to obtain dynamics for all spins

$$\frac{\mathrm{d}\rho(t)}{\mathrm{d}t} = -i\,[H, \rho] + \gamma \sum_d \mathcal{D}[L_d]\rho, \tag{5.5}$$

where having $d \in \{n, s, r\}$ gives us the dissipator $\mathcal{D}[L_d]\rho = L_d \rho L_d^\dagger - \frac{1}{2}\{L_d^\dagger L_d, \rho\}$ acting on all but the ancilla with the same phenomenological decay rate γ, with $L = \sigma^-$ or σ^Z giving spin decay and dephasing noise respectively. As with the last chapter, we need to use a measure of entanglement to study how well it is distributed across the network and we use E, the entanglement of formation [122] introduced in Sec. 2.4.2.

There are several factors that might affect routing ability that we wish to investigate. One family of factors are the values or ratios of system parameters which will determine whether the correct receiver was routed to. We will also look at two different methods of exploiting the eigenspectrum of the network. We have already mentioned in Sec. 1.2.2 the ability to tunnel through specific eigenstates in a spectrum if coupling into the system is weak compared to the internal couplings (see Fig. 1.6). The intent with this coupling ratio is to ensure that the rate of tunnelling into (from) levels other than the intended is small meaning minimal phase interference in the transferred state. In our case we will want to ensure addressability of receivers so using eigenspectrum tunnelling seems a promising avenue. Practically, using this method requires resonantly tuning the sender and the target receiver to the selected eigenstate energy to take advantage of the low interference tunnelling process.

There is another possible effect we could exploit when trying to influence which receiver is targeted; we present this diagrammatically in Fig. 5.2. We propose taking advantage of the contrasting population amplitude profiles (PAPs) of network

eigenstates to enhance the distinguishability of routing. If we imagine two eigenstates with similar energies then the eigenspectrum tunnelling method may not be perfectly interference-free as the tunnelling rate into the nearby levels will be higher in general. However, the receivers could be positioned to couple to regions of low population amplitude in the opposing eigenstate and high in the target eigenstate. This theoretically could reduce the tunnelling rate and hopefully provide some interference protection as it will reduce the overlap with the undesired eigenstate while maintaining a high overlap with the target pathway.
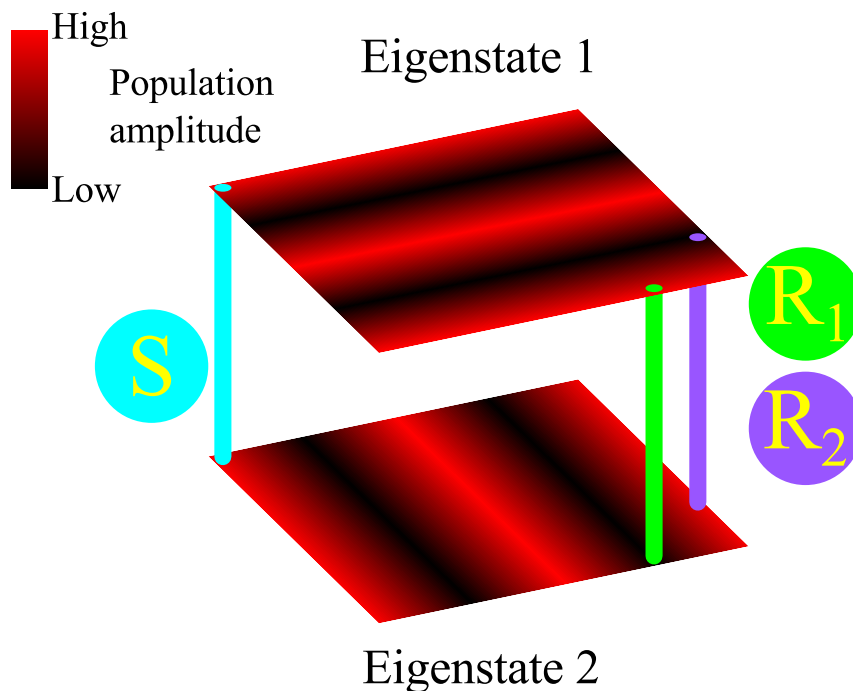
FIGURE 5.2: A conceptual example of how one might exploit regions of contrasting population amplitude between eigenstates of a network for enhanced routing effectiveness.

Our Hamiltonian and $L = \sigma^Z$ conserves spin number; in order to investigate routing over large networks efficiently we restrict our single (double) sender studies to the single (double) excitation subspace of H. The single excitation subspace can be represented in a basis of states $\{|\phi_k\rangle\}$ with $|\phi_k\rangle$ depicting the state with the k-th site spin up and all other sites down; so $k \in \{[1, N_{xy}], S_s, R_r, A_a\}$ where S, R and A are the senders, receivers and ancillae. This basis would have $N_{xy} + (2s_{\mathrm{max}}) + r_{\mathrm{max}}$ states where s_{max} and r_{max} are the total number of senders and receivers and the factor of two accounts for the ancilla associated with each sender. The case of $L = \sigma^-$ requires

the inclusion of a ground state when studying single sender routing, i.e. $|\phi_0\rangle$. This is because σ^- dissipation corresponds to a down spin flip process only.

The double excitation subspace extends this basis notion to $\{|\phi_{kk'}\rangle\}$ containing states with the k-th and k'-th sites spin up and the remaining sites down. The extra excitation means the basis span is slightly more complicated to present. We start with the number of states comprising only excitations in the network: $N_{xy}(N_{xy}-1)/2$. Then to this we need to add the number of states with only one excitation on the network: $N_{xy}(2s_{\max}+r_{\max})$. We next include the possibility of two excitations present only the ancillae, or only on the senders, or only on the receivers which contributes $s_{\max}(s_{\max}-1)+r_{\max}(r_{\max}-1)/2$ states to the basis span. Finally there are the number of states due to excitations being present on combinations of ancillae, senders and receivers: $s_{\max}^2 + 2s_{\max}r_{\max}$. In total then the basis span is

$$N_{xy}\frac{N_{xy}-1}{2} + s_{\max}(2s_{\max} + 2N_{xy} + 2r_{\max} - 1) + \frac{r_{\max}}{2}(r_{\max} + 2N_{xy} - 1). \quad (5.6)$$

For a double excitation solution and $L = \sigma^-$ a ground state and the single excitation subspace would need to be included, but we do not consider such a situation here.

Our method for obtaining dynamics is a numerical Python solution employing methods from the 'Quantum Toolbox in Python' (QuTiP) library [146] following a procedure we shall now overview. Firstly we find the single excitation eigenspectrum of the network in order to allow us to choose which eigenstates and network coordinates we are going to use for our routing process. This allows us to then set the values of the ε^{S} and the ε^{R} that are resonant with these targeted routing eigenstates. Next we define the full network-ancilla-sender-receiver system and evolve the system until some maximum time, then resetting and repeating for a given number of ε^{S}. Each evolution we initialise the ancilla and sender in a Bell $|\Psi^-\rangle$ state with all other spins down. Proceeding in this way we can obtain E dynamics for different routing process (different ε^{S} in a defined system) and compare the behaviours. Unlike in the last chapter where we performed scans over the configuration sets, with the type of system definitions we have here it would be impractical to scan all sender and receiver coupling coordinates across all eigenstates. Our assessment has been

restricted to a subset of system definitions and from these we present demonstrative cases.

5.2 Single sender routing

ET us start a discussion of what is possible in the routing of a single entangled pair with an introductory example. Consider a 3x2 network, which we referred to in the last chapter as a ladder: we can obtain its single excitation subspace eigenstates as shown in Fig. 5.3. The eigenstates are obtained from diagonalisation of the single excitation subspace of H_{N} in Eq. (5.2) which is clearly governed by κ. In this figure we have $\kappa = 900$ kHz which is one intra-channel coupling strength used in Chapter 4. The layout of the each eigenstate is designed to inform about the coefficient of the single excitation basis states $\{|\phi_k\rangle\}$.
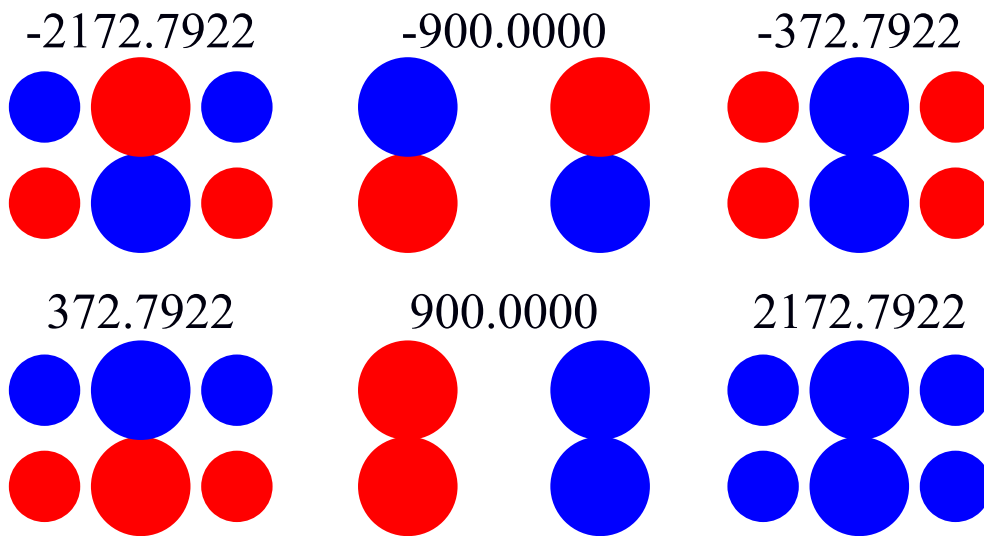
FIGURE 5.3: The 6 single excitation eigenvalues (in kHz) and eigenstates (numbered from 0) for an $N_x = 3$, $N_y = 2$ network. The circle size represents the single excitation basis state coefficient magnitude and the colour its phase: red⇒positive, blue⇒negative.

The diameter of circles in Fig. 5.3 and subsequent eigenstate figures are normalised to the largest coefficient in an eigensystem to allow visual comparison between eigenstates in an eigensystem. For clarity, the set of eigenstates for a system $\{|\psi_j\rangle\}$ can be written $|\psi_j\rangle = \sum_k C_{jk}|\phi_k\rangle$ where $\{|\phi_k\rangle\}$ is the single excitation basis of the network; mathematically it is of course possible for the C_{jk} to be complex but for our systems $C_{jk} \in \mathbb{R}$. This leads to the diameters $d_{jk} = |C_{jk}/C_{\mathrm{Max}}|$ where C_{Max} is

obtained from the whole $\{|\psi_j\rangle\}$. The phase of C determines the colour of a circle in an eigenstate figure: red is positive, blue is negative.

This eigenspectrum features levels that are well spaced and choosing external spin coupling $g = \kappa/10$ allows us to demonstrate eigenspectrum tunnelling. We can select the ±900 kHz eigenstates and define a system where $\varepsilon_1^{\mathrm{R}} = 900$ kHz and $\varepsilon_2^{\mathrm{R}} = -900$ kHz with the network coupling coordinates (3,1) and (3,2). To complete the definition of the system we choose to couple our sender to network position (1,1). Choosing $\varepsilon^{\mathrm{S}} = \pm900$ kHz we display solutions for $\gamma = 0$ and $\gamma = 2$ kHz with $L = \sigma^Z$ in Fig. 5.4.
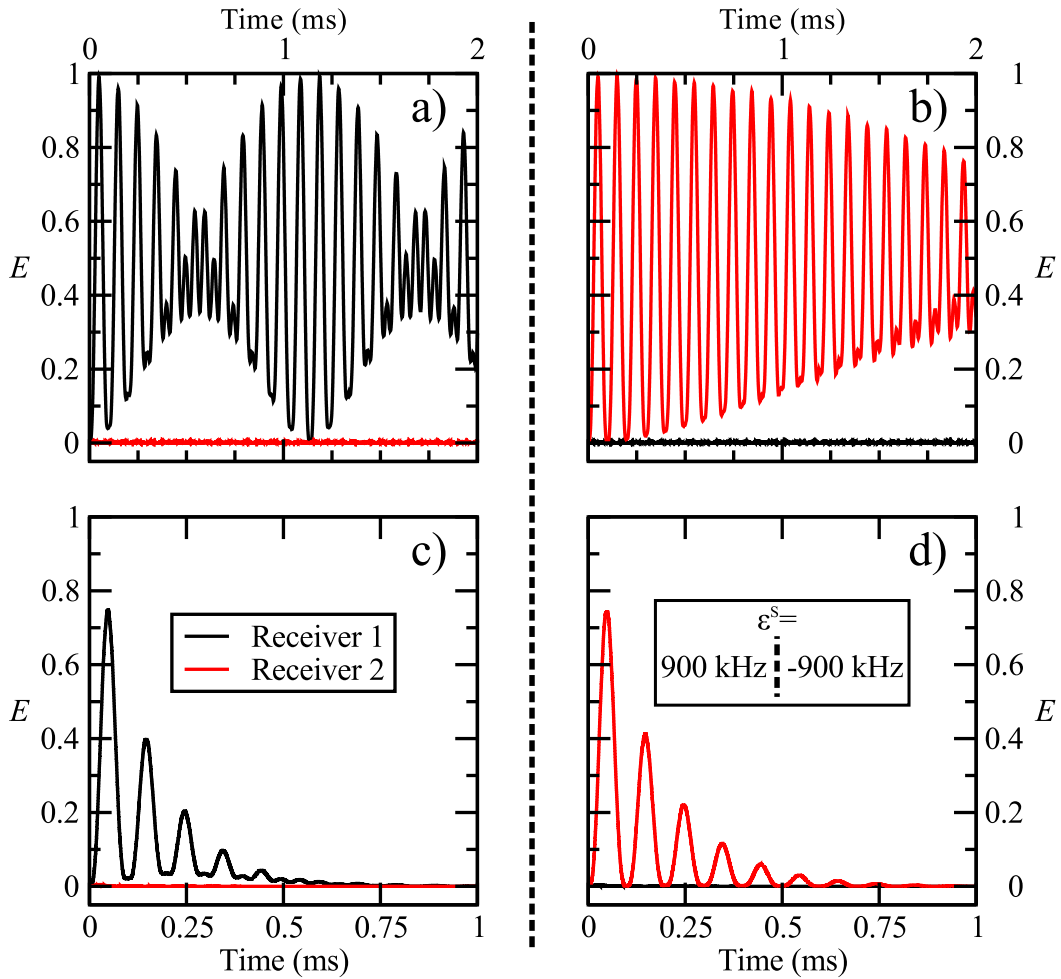
FIGURE 5.4: Entanglement of formation dynamics showing distinguishable routing processes in an $N_x = 3$, $N_y = 2$ network tunnelling through the ±900kHz eigenstates with $\varepsilon_1^{\mathrm{R}} = 900$ kHz and $\varepsilon_2^{\mathrm{R}} = -900$ kHz. a) and b) have $\gamma = 0$, c) and d) have $\gamma = 2$kHz. a) and c) have $\varepsilon^{\mathrm{S}} = 900$ kHz, b) and d) have $\varepsilon^{\mathrm{S}} = -900$ kHz

All four frames in Fig. 5.4 display good examples of distinguishable routing occurring; only the desired receiver ($\varepsilon^{\mathrm{S}} = \varepsilon^{\mathrm{R}_r}$) has significant E. The dissipationless examples in a) and b) show oscillatory beating and near perfect transfer whereas the presence of the bath in c) and d) damps away the dynamics leading to sub-perfect transfer of entanglement. The interesting difference between left and right panels is not due to the phase difference in the eigenstates and connection locations of the receivers, but the difference in 'distance' from sender to receiver. This can be shown running simulations (not shown here) with both receivers connected to network location (3,1) or (3,2): the dynamics for both receivers are the same despite being connected to network locations which exhibit a different phase coefficient for the two eigenstates. Incidentally this check exposes another property: having the receivers connected to the same spin does not appreciably increase 'bleeding' onto the incorrect receiver. The zero-lines in Fig. 5.4 show that there is no appreciable bleeding here either.

5.2.1 Eigenstate population amplitude exploitation

We need to move beyond the example of the $N_x = 3$, $N_y = 2$ network used so far in order to explore the possibility of taking advantage of eigenstates with interesting PAPs. We argued initially that this exploit would be good for dealing with closely spaced levels where the eigenstate tunnelling method used so far may not be interference free. With this in mind consider the two eigenstates with contiguous eigenvalues shown in Fig. 5.5 with a separation of ~ 16.5 kHz generated for an $N_x = 11$, $N_y = 7$ network where we are now using $\kappa = 200$ kHz. The highlighted 9th and 10th columns are perfect examples of where a PAP could be exploited with only one column having non-zero amplitude in each eigenstate; these columns are where the receivers can be coupled. The central row provides consistently high amplitudes and so along here is where we should couple. The fact that the central row sites in column 1 in both eigenstates have significant amplitude similar in size to the sender and receiver coupling locations makes it an ideal column for the sender coupling coordinate.
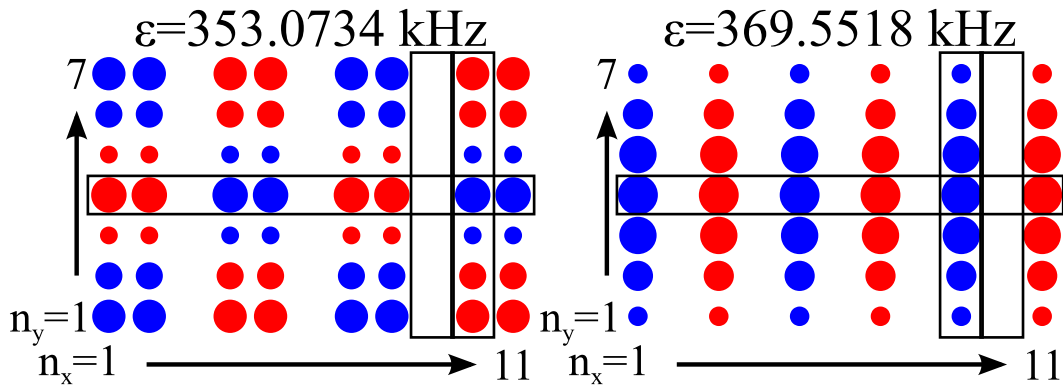
FIGURE 5.5: Two of seventy-seven single excitation eigenstates of an $N_x = 11$, $N_y = 7$ network with $\kappa = 200$ kHz. The 10th and 9th columns provide locations to couple receivers that correspond to regions of contrasting probability amplitude. The central row contains high amplitude coordinates in convenient locations for sender and receivers.

So, choosing the sender coupling coordinate (1,4) and the receiver coupling coordinates (10,4) and (9,4) we can generate the dynamics in Fig. 5.6, where again $g = \kappa/10$ but this time with $\gamma = 0.1$ kHz dephasing. There was no physical motivation for changing the values of γ, κ; this set was found to produce results comparable and consistent with the different parameters that were trialled numerically in the early stages of the investigation. The lower value of g (because κ is lower) means that tunnelling into and out of the network is at a slower rate which has the effect of causing slower transfer compared with Fig. 5.4. If we compare the two frames in Fig. 5.6 we can see similar (but not identical) amplitude and transfer speeds for the two routing process. For any route independent subsequent actions one would presumably ideally want perfect symmetry between routing process which we do not have here. However it is also reasonable to propose differences between routed outcomes can be handled by some post-processing step. It is also possible that a subsequent action would not require routed entanglement levels to be identical.

The amount of bleeding into the incorrect receiver in Fig. 5.6 is definitely greater than in Fig. 5.4. A comprehensive explanation for this is hard to find due to the differences between system definitions, but the fact that the energy levels being used are much closer together is definitely an important factor. Logically we want to minimise bleeding between receivers to ensure routing processes result in distinguishable
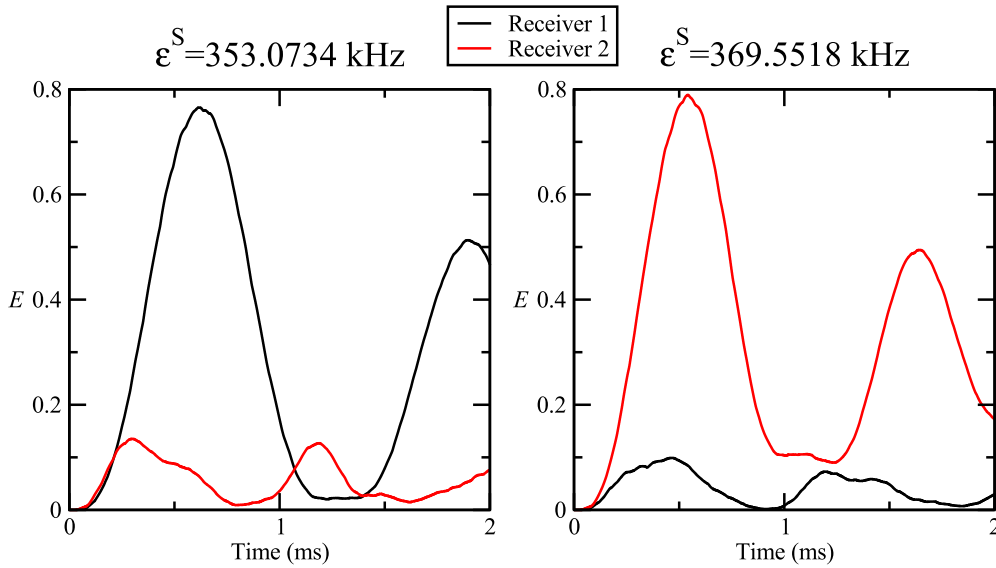
FIGURE 5.6: Routing dynamics utilising a receiver coupling configuration that takes advantage of the PAP to minimise coupling to the undesirable eigenstate. The network used has $N_x = 11$, $N_y = 7$ with couplings $g = \kappa/10 = 20$ kHz and dephasing with $\gamma = 0.1$ kHz.

transfer, although it is possible again post-routing process could be controlled externally based on user expectation rather than global manipulation. We argued that our PAP exploitation would protect against bleeding between closely spaced eigenstates more effectively than relying on tunnelling. This is not a straightforward comparison to make as we must use a different site(s) to couple receivers to test each exploit method or use different energy levels which are similarly spaced but allow fixed receiver coupling coordinates.

In Fig. 5.7 we present results for the same eigenstates as our PAP results but with both receivers coupled to (11,4). The bleeding levels are very similar, which is somewhat unexpected. Further, transfer rates stay roughly the same but we can immediately see the lower energy routed amplitude is reduced here compared to the PAP exploited result. This is a positive result for using PAP exploitation, but it isn't conclusive proof it is always better.

The value of the the sender and receiver coupling to the network, which has so far been $g = \kappa/10$, is a factor that influences the amount of undesired eigenstate tunnelling; the larger g is, the higher the tunnelling rate into eigenstates around the targeted level. Let us see if there is a clear value of g which allows the PAP exploitation to provide a significant benefit in this $N_x = 11$, $N_y = 7$ network compared to simple
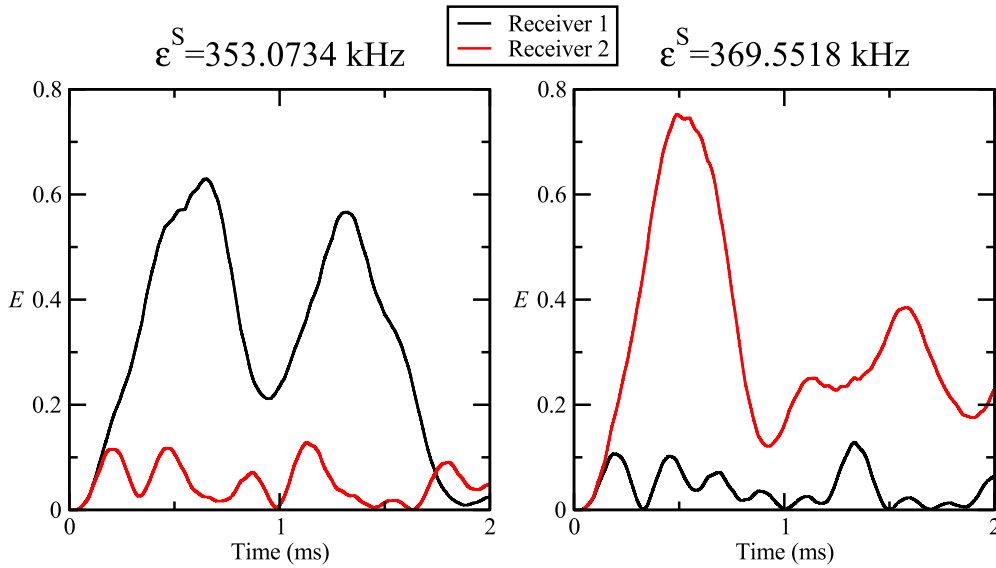
FIGURE 5.7: Routing dynamics contrasting those in Fig. 5.6 relying on eigenstate tunnelling alone with both receivers coupled to (11,4). We see similar bleeding levels and slightly reduced maximum transfer peak with the lower energy eigenstate.

tunnelling. In Fig. 5.8 we show results of a scan over g as a fraction of κ for the PAP and tunnelling setups used in Figs. 5.6 and 5.7; we produce dynamics for each ε^S and g/κ, taking the maximum E on the desired receiver and, at the same time, the value of E from the incorrect receiver. This is in order to assess the transferred and bleeding entanglement as the sender and receiver coupling increases.

In the top panels of Fig. 5.8 we can see the scan results for the maximum entanglement transferred to the desired receiver (receiver 1 in the left case and receiver 2 in the right case) and the bleeding to the undesired receiver (vice versa) for a PAP setup (black and red) and a basic tunnelling setup (green and blue). There is a region around $g/\kappa = 0.1$ where the PAP scheme receivers outperform the simple tunnelling scheme, albeit only slightly. The bottom panels are to aid in analysis of the comparison between the PAP and tunnelling schemes by plotting the difference between the performance of each receiver under the schemes; i.e. a positive difference indicates the PAP value of E is larger for that particular receiver at that value of g/κ. On the left, purple is the desirable receiver difference whereas on the right it is cyan. Both panels display the region around $g/\kappa = 0.1$ where the PAP provides a higher transfer, following this there is a small cross-over where the undesirable receiver difference becomes
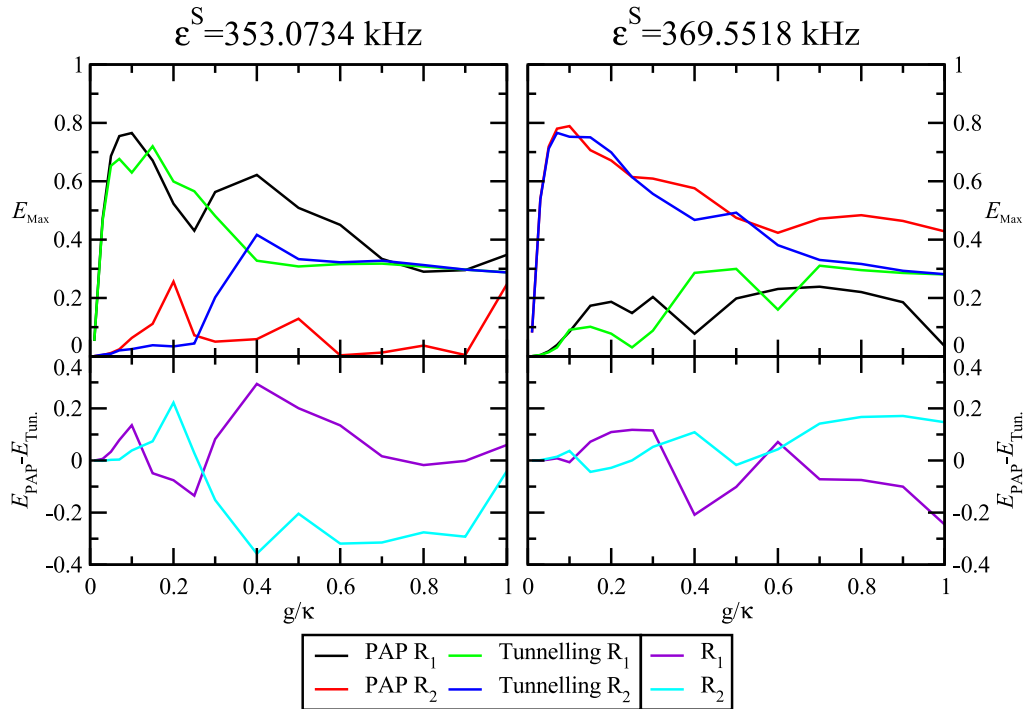
FIGURE 5.8: Top: Results from a scan over g showing maximum desirable transferred entanglement and the corresponding value of the undesirable bleeding for PAP and tunnelling implementations. Bottom: Difference between the PAP and tunnelling results for desired transfer and the transfer bleeding. From both plots there is an indication that the PAP scheme performs slightly better.

positive and the desirable negative. This implies that the bleeding in the PAP case becomes larger than the tunnelling case at the same point as the desirable transfer in the tunnelling case beats the PAP case. Increasing the g/κ ratio further then undoes this change and looking at the top panels again, exploiting the PAP appears to generally lead to less bleeding and more desirable transfer compared with a simple tunnelling approach which clearly tends to an equal amount of desirable and undesirable E. Ideally though the high transfer, low bleeding region around $g/\kappa = 0.1$ provides the optimal choice as the desirable-to-undesirable E ratio is much more favourable than at higher g/κ values.

The PAP method was suggested for eigenstates close together, but let us look at a situation where the spacing is much greater to see what might be inferred about routing operations. In the top of Fig. 5.9 we can see two distant eigenstates in the $N_x = 11$, $N_y = 7$ network we have been using throughout this section. We indicate on those diagrams the sender coordinate (2,2) as well as the coordinates for the two receivers

in the PAP case, (8,6) and (6,6), and the location of both senders in the tunnelling-alone case (10,6). Below the eigenstates in Fig. 5.9 we can see the routing dynamics for both cases and immediately it is obvious that with distant eigenstates there is virtually no bleeding in either exploitation method. It is also apparent that tunnelling-alone consistently transfers better through the second eigenstate and at its optimal $g/\kappa \approx 0.2$ it is also the better performer in the first eigenstate, although in general here the two cases perform similarly.
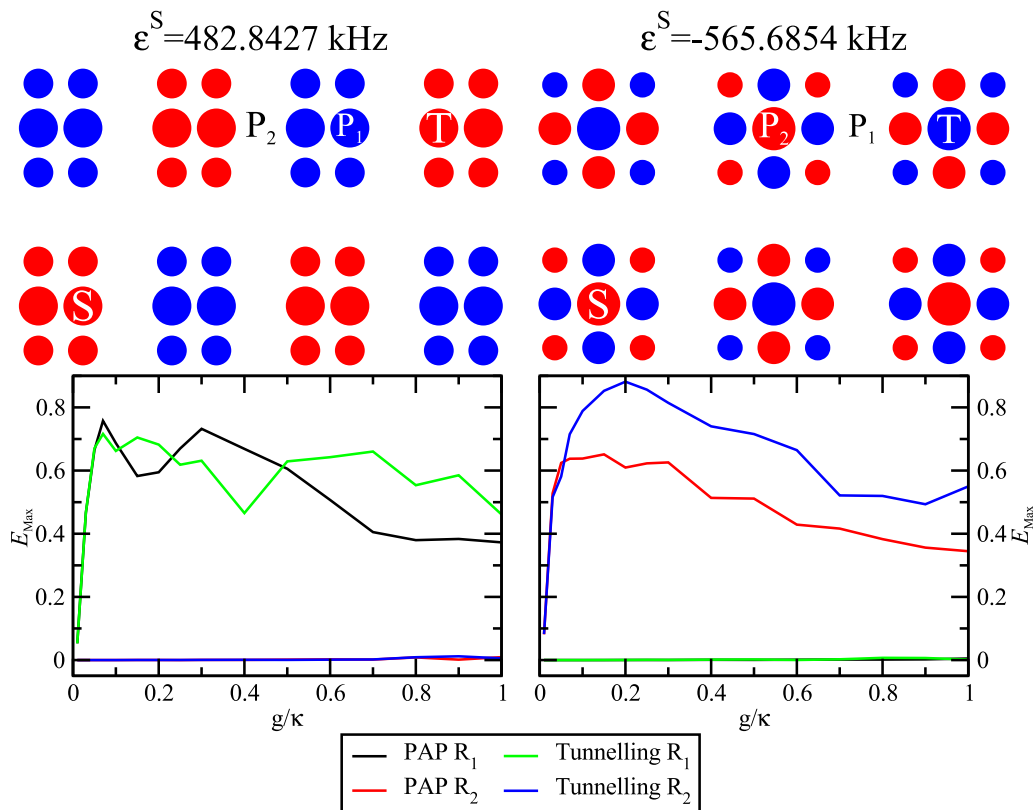
FIGURE 5.9: Top: Eigenstate diagrams depicting two distant states that can be used for routing processes in the $\kappa = 200$ kHz $N_x = 11$, $N_y = 7$ network we have been discussing. Indications of the coupling coordinates for the sender, PAP receivers and tunnelling-alone receivers. Bottom: Routing dynamics for the two exploitation schemes using the above eigenstates. Due to the distant nature of the states bleeding is effectively prohibited.

We looked at many of these sorts of outputs for different sized networks, coupling coordinates and energy levels for the differences between the results obtained from a PAP scheme and a simple eigenstate tunnelling scheme. The PAP scheme can be shown to allow higher amplitude and more distinguishable transfer in some cases (as we can see in the figures within this section). Clearly though the reduction in

bleeding provided by using distant eigenstates makes those particularly appealing. We believe that the 'best' choice of coupling coordinates relies very strongly on the system definition and as such no global statement can be made on which scheme should be used. Given time and a particular system definition one may be able to find a particularly effective PAP scheme set-up but, for an initial impression of what is possible, the use of simple tunnelling through distant eigenstates proves effective.

We have found that it is important to match the magnitude of the site probability that the sender and receiver couple to if efficient transfer is to be achieved; a difference leads to competing oscillations in the E dynamics as tunnelling in to and out of the network is occurring at different rates. Another consideration is the effect of ε^{S} and ε^{R} deviating from their target eigenstates. Recalling Fig. 4.3 and our reasoning for using $g/\kappa = 1$ in the last chapter, we can infer that a deviation from the target eigenstate at the low coupling ratios used in this chapter will results in reduced transfer.

5.3   Two-sender routing

NE obvious and interesting extension of this work is to imagine we now have two senders that wish to route through a network to particular receivers. We now need to modify our computational solution to handle the double excitation subspace of the system. During the design of this modified program we chose to no longer consider dissipation. As we do not have a physical implementation specifically in mind to lend quantitative decay information and based on the observations of the last section and chapter, we adopted the view that we could still obtain meaningful results without an environment (i.e. $\gamma = 0$). A dissipative environment acts to reduce the effectiveness of entanglement transfer as can be seen in Fig. 5.4, so this is what we must bear in mind when considering results here.

The other thing to consider when shifting to routing two entanglement pairs is how the dynamics proceed. In the last section we followed a process like

$$|\phi_{\mathrm{S}}\rangle \to |\psi_{\varepsilon_n}\rangle \to |\phi_{\mathrm{R}_r}\rangle \,, \tag{5.7}$$

using the single excitation subspace notation we introduced in Sec. 5.1, where $|\psi_{\varepsilon_n}\rangle$ is a network eigenstate $H_N |\psi_{\varepsilon_n}\rangle = \varepsilon_n |\psi_{\varepsilon_n}\rangle$. It is implicit above that $\varepsilon^S = \varepsilon_r^R = \varepsilon_n$. In the two-sender case there are a few process that we could think of, remembering that the form of our Hamiltonian restricts us to single spin flip process. Three eigenstate tunnelling examples are

$$|\phi_{S_s S_{s'}}\rangle \rightarrow |\psi_{\varepsilon_n S_{s'}}\rangle \rightarrow |\Psi_{\varepsilon_m}\rangle \rightarrow |\psi_{\varepsilon_n R_{r'}}\rangle \rightarrow |\phi_{R_r R_{r'}}\rangle, \tag{5.8}$$

$$|\phi_{S_s S_{s'}}\rangle \rightarrow |\psi_{\varepsilon_n S_{s'}}\rangle \rightarrow |\psi_{\varepsilon_n \varepsilon_{n'}}\rangle \rightarrow |\psi_{\varepsilon_n R_{r'}}\rangle \rightarrow |\phi_{R_r R_{r'}}\rangle, \tag{5.9}$$

$$|\phi_{S_s S_{s'}}\rangle \rightarrow |\psi_{\varepsilon_n S_{s'}}\rangle \rightarrow |\phi_{R_r S_{s'}}\rangle \rightarrow |\psi_{R_r \varepsilon_{n'}}\rangle \rightarrow |\phi_{R_r R_{r'}}\rangle, \tag{5.10}$$

where we consider using a double excitation eigenstate $|\Psi_{\varepsilon_m}\rangle$, a superposition of double excitation eigenstates which can be thought of as representing two single excitation states $|\psi_{\varepsilon_n \varepsilon_{n'}}\rangle$, or simply two single excitation processes. Of course it is possible to change the ordering of sender (receiver) transfers and as we are dealing with a quantum system it is possible for these process channels to occur in superposition. Our study of two-sender routing will mostly focus on understanding implementation in terms of these processes.

5.3.1 Two site toy model and parabolic coupling

The first step we made towards two-sender routing was to think about a toy model test case, an exact solution for a two spin network to be precise. An exact computational solution for a two spin network is simple and quick to code using the QuTiP library and can be used to assess if two-sender routing can work, further it can be used as a comparison for the subsequent, more general, double excitation code. A two spin-1/2 network defined by our Hamiltonian in Eq. (5.2) has 4 eigenstates which are depicted graphically in Fig. 5.10 along with a schematic of the system. We have written sender and receiver couplings generally rather than the uniform coupling scheme used thus far ($g_{S_1} = g_{S_2} = g_{R_1} = g_{R_2} = g$) because shortly we shall investigate an alternative.

Initially though let us consider our tunnelling approach with uniform g for our first attempt at sending two entanglement pairs simultaneously with this two spin toy
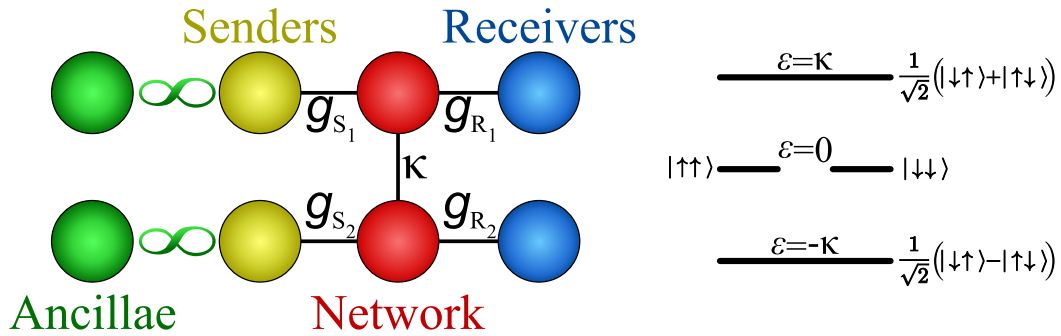
FIGURE 5.10: Left: Our toy model schematic for two-sender routing on a 2-network where we have highlighted the possibility to have non-uniform sender and receiver couplings. Right: The eigenspectrum for the network assuming (as we defined initially in Eq. (5.2)) that there is no on-site energy splitting.

network. If we set up the eigenstate tunnelling such that the energy splitting of the first sender and receiver is resonant with the superposition state $|+\rangle = \frac{1}{\sqrt{2}} (|0\rangle + |1\rangle)$ and the second are resonant with the $|-\rangle = \frac{1}{\sqrt{2}} (|0\rangle - |1\rangle)$ state we can think of the process as going 'straight through' the network as we have drawn it in Fig. 5.10. The eigenenergy of the superposition states $|\pm\rangle$ is $\pm\kappa$ and in this model if both senders have given their excitation to the network it will be in the $|\uparrow\uparrow\rangle$. In the left frame of Fig. 5.11 we display entanglement of formation dynamics for such a set up. The entanglement created between the first ancilla and receiver is identical to that created between the second ancilla and receiver, hence the use of circles at points along the obscured lines; there is also effectively no bleeding of entanglement between the undesired pairs. However, the right panel shows what happens when we swap the energy splittings of the senders. This does have the desired effect of having the first sender targeting the second receiver and vice versa however the magnitude and oscillatory components present are vastly different compared to the 'straight through' set-up; we do still maintain simultaneous transfer rates and avoid bleeding though.

It is possible there is some blocking effect with such a small network that is inhibiting the routing process when we desire two pieces of information to travel through each other, which is the case here when the bottom (top) sender is targeting the top (bottom) receiver. In the next section we look at larger networks in an effort to (quite literally) get around this issue, however in the remainder of this section we
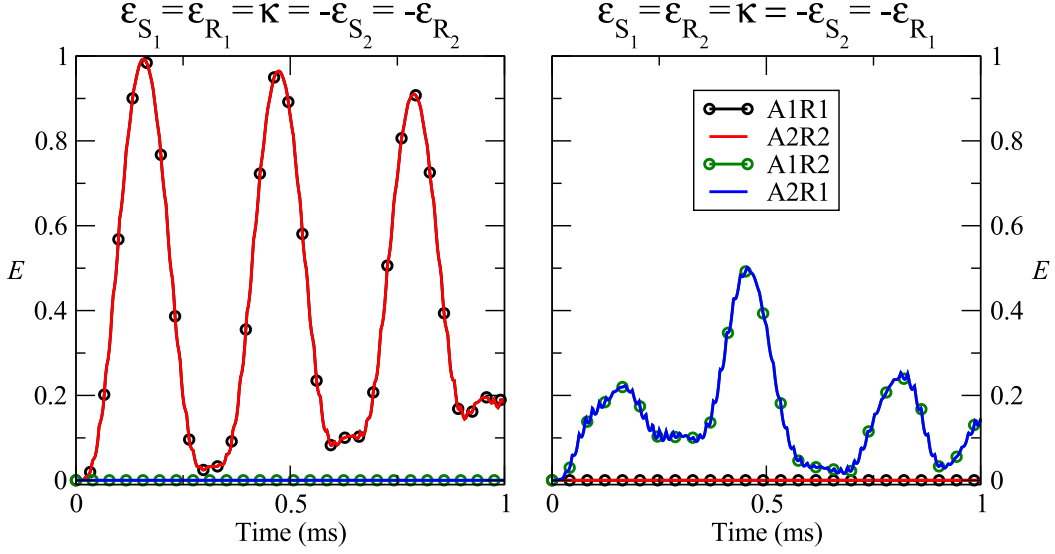
FIGURE 5.11: Entanglement of formation dynamics from our toy two spin network with uniform sender and receiver couplings. Left: The first (second) sender targets the first (second) receiver via the $\varepsilon = \kappa$ ($\varepsilon = -\kappa$) eigenstate. Right: The energy splittings of the sender spins is now swapped to have them route to the different receivers.

will consider different sender and receiver coupling parameters. The parabolic coupling scheme was used by Christandl *et al.* to illicit perfect quantum state transfer along a (dissipationless) 1D chain [50] and gets its name from the profile of the couplings between spins. The n and $n + 1$ spins in an N-spin chain have a coupling $\kappa_n \propto \sqrt{n(N-n)}$. Given an initially populated first spin state, the effect on the dynamics of this profile is to sequentially (although not maximally) populate the spins in the chain until at some time later the state recombines, maximally, on the final spin. Recognising that our process in Eq. (5.8) resembles dynamics along a chain, with each stage taking the place of a spin, we can engineer a Hamiltonian that incorporates parabolic coupling between intermediate steps to illicit perfect transfer.

In our toy model, the way of encoding parabolic coupling into our decidedly un-chainlike system is by picking the relevant values of g_{S_s} and g_{R_r} (as defined in Fig. 5.10) such that they couple correctly to the network eigenvalues to ensure the right ordering of the process. Until we find a suitable parabolic chain we will use state expectation values and spin population as measures of state transfer using an initial state where both senders are up and everything else is down. This can give us insight into how effectively our parabolic system is preforming, but does not tell us

about arbitrary initial states. Our desired double excitation states in this toy system approximating a parabolic chain are

$$|SS\rangle \xrightarrow{\sqrt{4}} |+S\rangle \xrightarrow{\sqrt{6}} |\uparrow\uparrow\rangle \xrightarrow{\sqrt{6}} |+R\rangle \xrightarrow{\sqrt{4}} |RR\rangle , \tag{5.11}$$

where above the arrows we have written the required coupling between states.

In Eq. (5.11) we propose tunnelling through the $|+\rangle$ eigenstate of the network, the $|\uparrow\uparrow\rangle$ state corresponds to both network spins excited and the S and R components refer to senders and receivers with ordering in a ket denoting whether it is first or second. In Fig. 5.12 we display results for transfer through our toy system. The left panel is the expectation value of each constituent in our process in Eq. (5.11) along with the sum of these values. Clearly this sum is not always 1 meaning there are other states participating in the transfer process; this means we do not get perfect recombination into $|RR\rangle$. Although, as we can see in the right panel, the two receivers do receive their full excitation just not at the same time, something a parabolic coupling scheme should be capable of ensuring.

The issue here is that the eigenspectrum presented in Fig. 5.10 and our exploitation of it are highly symmetric, meaning terms other than those in our Eq. (5.11) process participate and there are directionality problems. To combat this and obtain what the parabolic coupling scheme promises we can insert an extra $\sigma^Z \sigma^Z$ coupling term to our network Hamiltonian making this new toy version

$$H'_\mathrm{N} = \kappa \left(\sigma_1^+ \sigma_2^- + \sigma_1^- \sigma_2^+ \right) + J \sigma_1^Z \sigma_2^Z \tag{5.12}$$

which now resembles a Heisenberg Hamiltonian. This extra term lifts some of the symmetry of the eigenspectrum which now has the form in Fig. 5.13 for $J > \kappa$. We can further aid in avoiding symmetry if we modify the process to

$$|SS\rangle \xrightarrow{\sqrt{4}} |+S\rangle \xrightarrow{\sqrt{6}} |\uparrow\uparrow\rangle \xrightarrow{\sqrt{6}} |-R\rangle \xrightarrow{\sqrt{4}} |RR\rangle , \tag{5.13}$$

where we now make use of the negative superposition state to exit from the network.

Ensuring our sender and receiver energies are set to target the corresponding
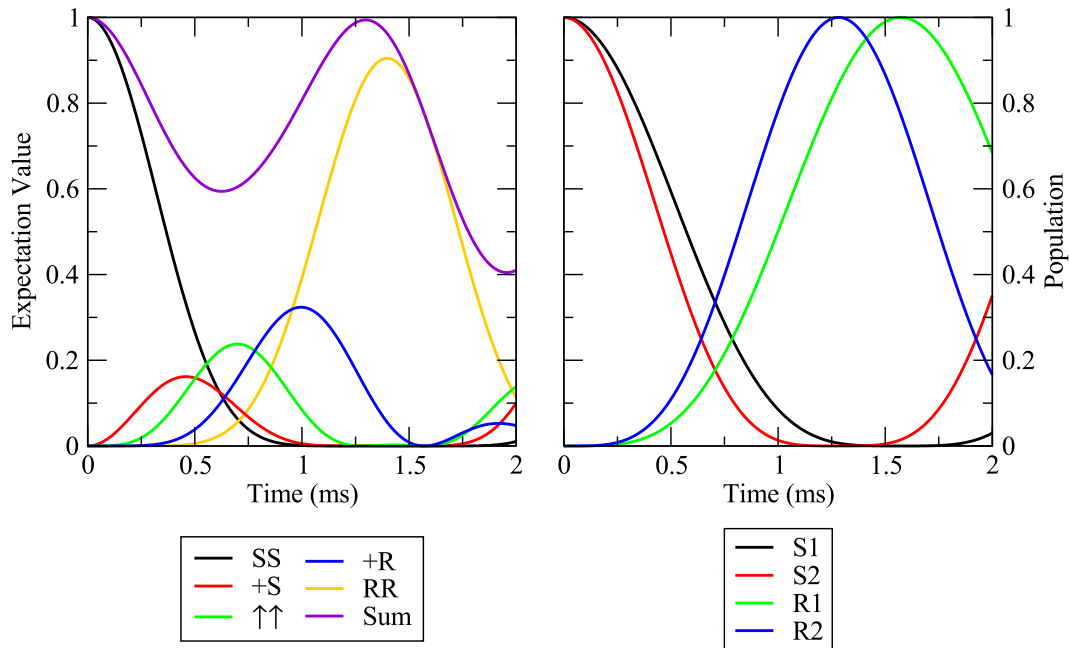
FIGURE 5.12: Left: Expectation values (and sum of) for the states in our parabolic coupling state transfer process through our toy system. There is definite participation from other states meaning the state does not perfectly recombine at the end of the effective chain. Right: Probability of excitation for the senders and receivers where clearly the full excitation does transfer through albeit not peaking simultaneously as desired from this scheme.

FIGURE 5.13: The new eigenspectrum for the two spin toy network when adding a $\sigma^Z \sigma^Z$ term to the network Hamiltonian. This is for the case $J > \kappa$.

eigenstates described in Eq. (5.13) ensures that undesired process are off-resonant with any eigenspectrum transitions and are excluded from the dynamics. So with these modifications and with setting $J = 500$ kHz, we can obtain the successful parabolic transfer displayed in Fig. 5.14. The sum line is fixed at 1 showing that we have indeed isolated the process states and we can see the state recombines maximally at 2.25 ms. The probability plot complements this with the information that at this time both receivers are maximally excited.

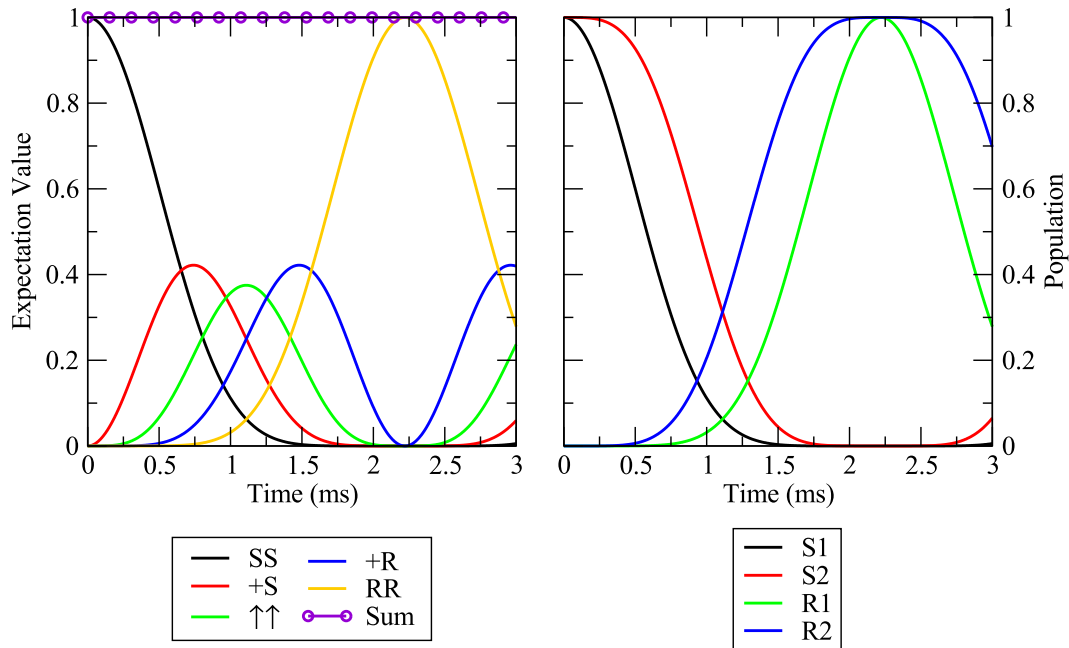There is however a problem, for when we move to entanglement routing via

FIGURE 5.14: Left: Expectation values (and sum of) for our process and toy system now with the $\sigma^Z \sigma^Z$ network term. The state successfully recombines and we have no participation from states out-with the intended process. Right: Receiver excitation probability maximises simultaneously showing the initial state to have transferred.

this set up we are unable to transfer any entanglement despite seeing the states sequentially populate as one expects. Rather then a plot of $E = 0$, we illustrate this in Fig. 5.15 by showing the dynamics for an initial sender 1 state $\sqrt{0.8}\,|\!\uparrow\rangle + \sqrt{0.2}\,|\!\downarrow\rangle$ and initial sender 2 state $\sqrt{0.65}\,|\!\uparrow\rangle + \sqrt{0.35}\,|\!\downarrow\rangle$ and all other spins are down. We see the summation of the process expectation values remains fixed showing us we have a working parabolic process with recombination on the final state, but as we can see in the right panel with the probabilities, its not the state we wish. The initial state allows for single excitation initial state components beyond $|SS\rangle$, as would the Bell $|\Psi^-\rangle$ state we would use to demonstrate entanglement routing. The dynamics of these extra states are not accounted for in the parabolic control scheme and so their evolution is part of the reason why the state (and hence entanglement) transfer is not as we desire. Another part is the phase changing action of the $\sigma^Z \sigma^Z$ term we added to enable us to encode a parabolic chain.
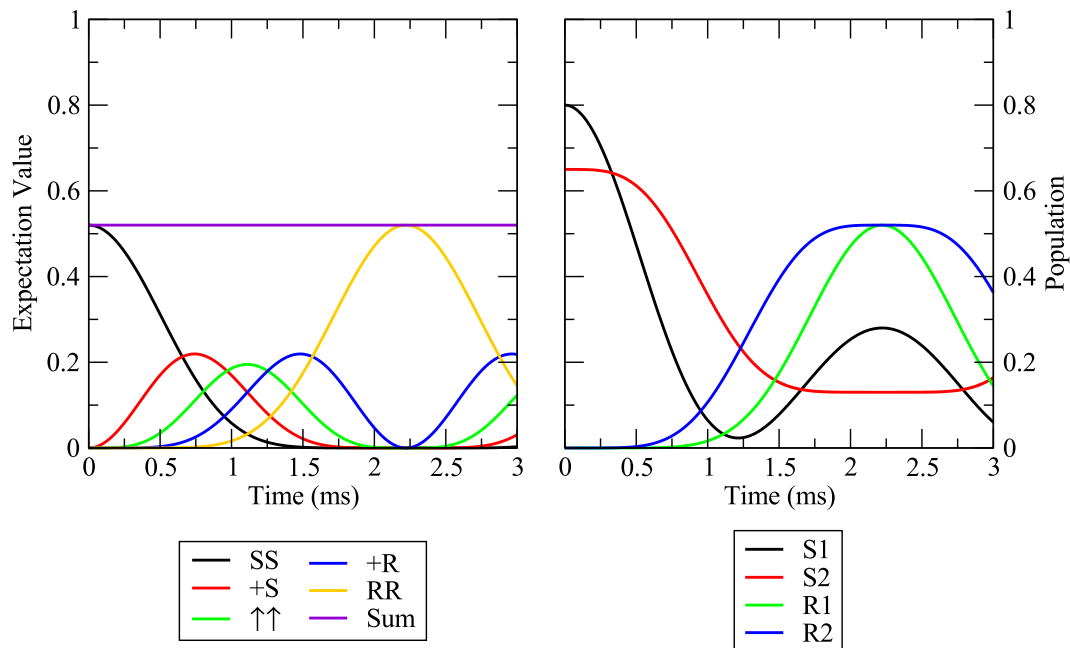
FIGURE 5.15: Left: Expectation values of the parabolic chain states for the dynamics of a coherent initial state where sender one is 80% excited, sender two is 65% excited and all remaining spins are spin down. Right: The failures of the parabolic scheme encoding for this system are made apparent with this probability plot showing the initial state to be incorrectly transported upon recombination.

5.3.2 Uniform coupling network routing

As we saw in Fig. 5.11 routing two entanglement pairs is possible in a two site network with uniform sender and receiver coupling, but changing the targeted receivers greatly affected the outcome. In the last section we tried to get around this using parabolic coupling and we found that did not provide an appropriate solution. Here we shall return to our original Hamiltonian and idea of uniform sender and receiver couplings with $g = \kappa/10 = 20$ kHz. We will now be using a computational solution in the double excitation subspace allowing us to produce dynamics for larger networks than a full-space solution would allow.

From our two site toy results it seemed that there was some sort of blocking issue when the process required transfer to cross over in a confined network. One possible solution, if we are restricted to a 1D network (chain), is to change the sender and receiver placements such that the senders are at one end of the chain and the receivers are at the other such that the transfer happens down the chain. Each process should now be symmetric and switching targets should produce the same transfer. As we

can see in Fig. 5.16 this is indeed the behaviour observed for both a 2-length chain (top) and an 11-length chain (bottom) with the legend denoting for which receiver and ancilla E is reported. The left and right sides of the figure present the results with the different sender-receiver targeting: on the left $\varepsilon_{S_1} = \varepsilon_{R_1} = 200$ kHz, on the right $\varepsilon_{S_1} = \varepsilon_{R_2} = 200$ kHz with the other pair in each circumstance resonant with the -200 kHz eigenstate. We see no bleeding and perfect symmetry between processes and targets.

Whilst this new result that spin chains are capable of multiple entanglement routing is a nice compliment to the results of last chapter it would be interesting to explore other geometries as our computational method now allows it. We would like to reiterate though that the great number of possible network, sender, receiver, eigenstate and parameter configurations is impossible to scan entirely and this work should be treated as a sampling of some of the possibilities. With that in mind let us take a look at an $N_x = 4$, $N_y = 3$ network. We will use the two eigenstates shown in Fig. 5.17. To be clear, we are aware that the interpretation of using two single excitation eigenstates to transport both double and single excitation components of some arbitrary initial state is a simplification. A rigorous definition of the transport of these two components is a very difficult problem and, as we hope one can see from our results, our interpretation does produce useful routing processes.

In Fig. 5.18 we present routing dynamics for two different sender and receiver coupling coordinates. The left frames have sender 1 targeting receiver 1 using the positive eigenvalue and the right frames have sender 1 targeting receiver 2 also with the positive eigenvalue; the other pairs in each situation use the negative eigenvalue. In the top frames the first sender and receiver are coupled to the bottom row at the left and right extremes of the network with the second sender and receiver doing the same but on the top row. The bottom frames have the senders placed along the bottom row at the left and right extremes with the receivers at the top. We can see we again have simultaneous transfer and no bleeding for a given set-up because the 'distance' through the network in each frame is the same. However we see that the increase in 'distance' between senders and receivers when cross-pairs target each other (in the right frames) results in lower amplitude transfer. What is interesting is the fact that

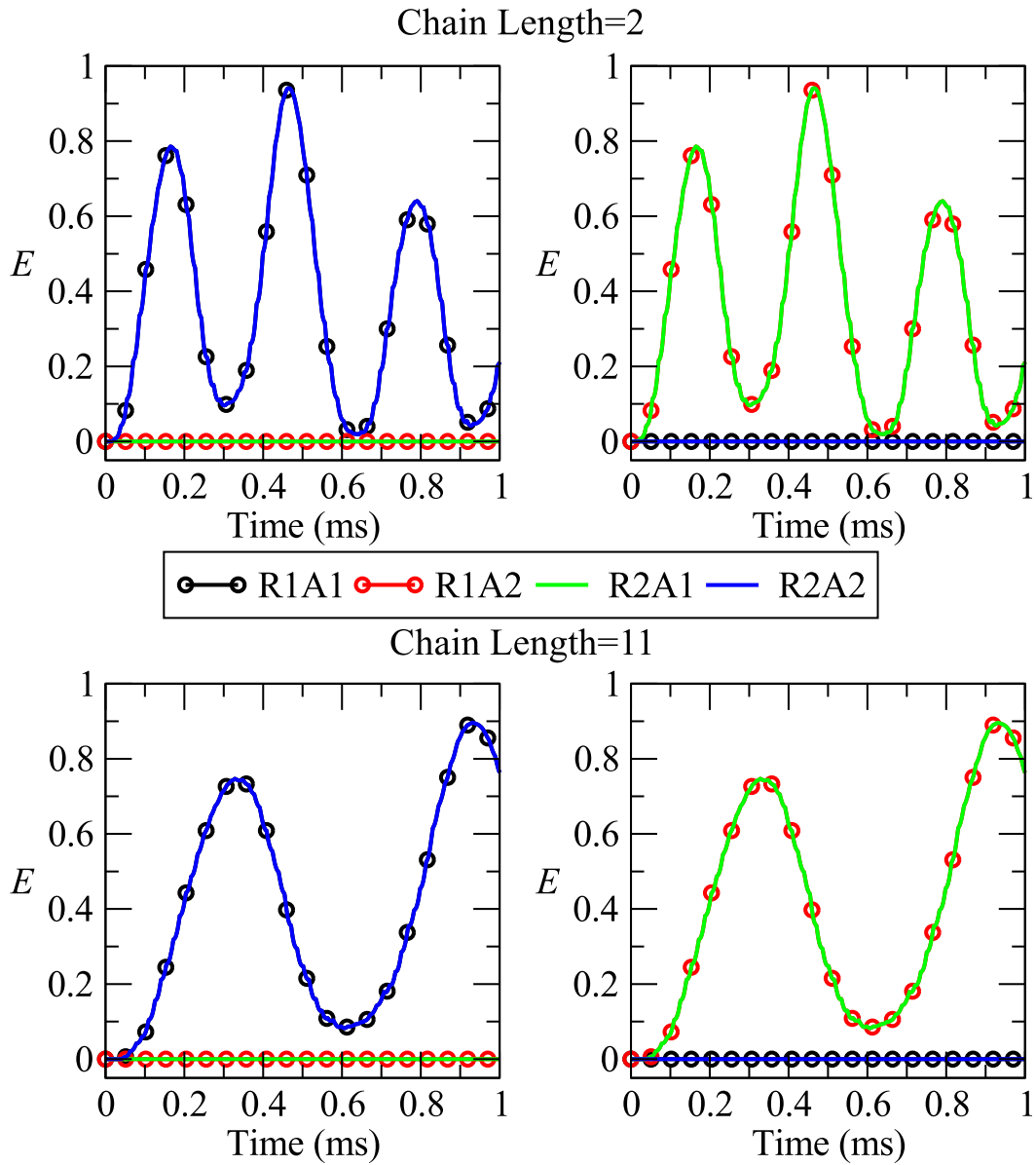Chain Length=2

Chain Length=11

FIGURE 5.16: Dynamics showing the successful routing of two entanglement pairs down a chain-network of length top) 2 and bottom) 11. Both lengths have the eigenstates $\varepsilon = \pm 200$. Left: We have the first sender and receiver using the positive channel with the second using the negative. Right: The first sender and second receiver use the positive channel with the remaining pair using the negative channel.
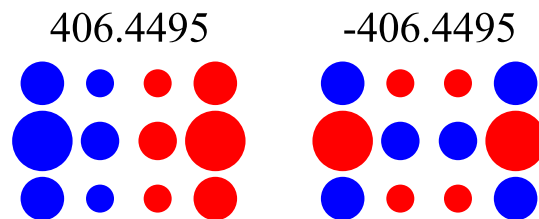
406.4495   -406.4495

FIGURE 5.17: Two single excitation eigenstates for a $N_x = 4$, $N_y = 3$ network.

the right frames are different to each other despite the 'distance' across the network between target pairs being the same. It is possible that the phase differences in the network and the different sender/receiver locations is the reason for this as the location the excitation begins to enter the network is changed; future work could explore this possibility.
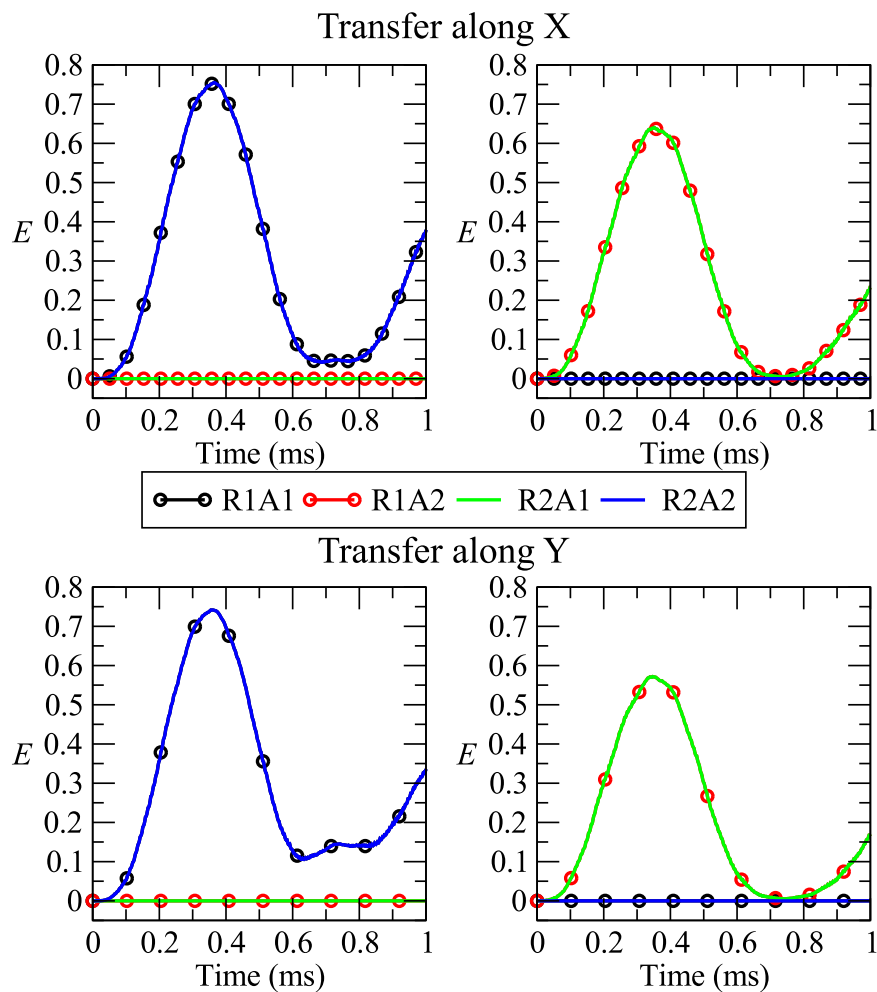

FIGURE 5.18: Routing dynamics using the eigenstates in Fig. 5.17 from a $N_x = 4$, $N_y = 3$ network. Top: The senders are coupled at the bottom left and top left corners of the network with receivers at the bottom and top right; x-axis transfer. Bottom: The senders are coupled to the bottom left and right with receivers at the top left and right; y-axis transfer. The target receivers are left) along the network edge and right) across the network.

We put 'distance' in inverted commas as it is a difficult concept to define in this quantum transport process. We are not populating each site in turn like some classical hopping process, we are tunnelling through an eigenstate. Our usage is meant to

encapsulate the number of spins involved in an eigenstate, and the length of a classical path between a sender and receiver. In our chains of Fig. 5.16 the senders can swap targets and still have to travel the same 'distance'. Although, going from 2 to 11 sites we can see the increased 'distance' leads to a longer transfer time. For the configurations in Fig. 5.18 changing the target receivers does change the classical hopping distance although we don't see any dramatic changes in transfer time.

It is possible to configure a same-'distance' set-up in the $N_x = 4$, $N_y = 3$ network. The results displayed in Fig. 5.19 come from having the senders at the bottom left and top right and both receivers connected to the mid-row at the far end of the x-axis. This triangular set-up now clearly performs equally well no matter which receiver is targeted.
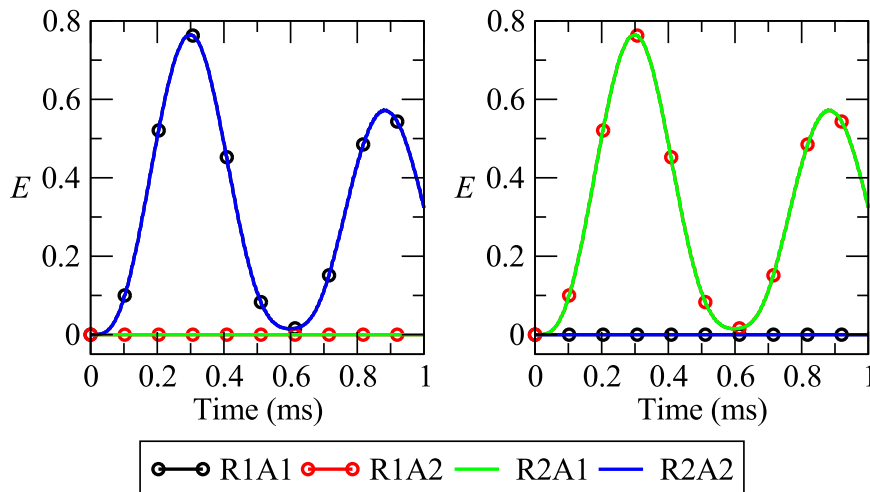

FIGURE 5.19: Results showing a symmetric routing process in a $N_x = 4$, $N_y = 3$ network using the eigenstates in Fig. 5.17. The senders are at the top and bottom of the left side of the network with both receivers coupled to the middle site at the far right end of the network.

There is one final thing we found using this $N_x = 4$, $N_y = 3$ network in a triangular configuration that we would like to show. We added a third receiver to the coupling location targeting a different eigenstate with probability amplitude at that site: $\varepsilon = -159.2359$ kHz. The effect this has can be seen in Fig. 5.20 where the left panel shows the senders targeting the old eigenstates and the right shows the second sender tuned to the new eigenstate. Interestingly, the left panel here differs slightly from the left panel of Fig. 5.19, with only subtly more bleeding present here; the other

curves (such as R2A1) are not shown here to avoid clutter, but were as low as in previous plots. It seems as though the presence of this new sender, despite only having a small amount of bleed from the system (entangling it with the sister-ancilla of the closer -406.4496 kHz-targeting sender), does change the dynamics and affects the entanglement transferred. However we note that routing is clearly still possible.
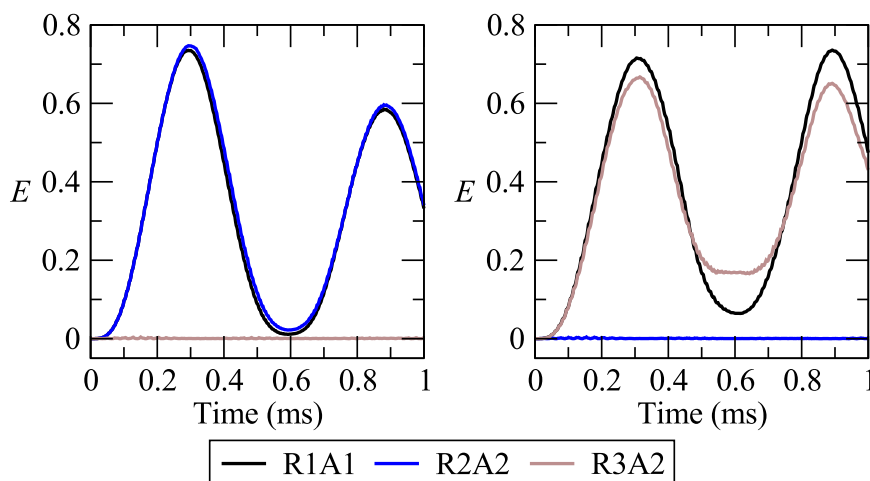

FIGURE 5.20: Results adding a third receiver to the set-up in Fig. 5.19, again to the right of the network at the middle site. It is resonant with a different eigenvalue and we show it (left) not targeted and (right) targeted by a sender. Its presence in the system does disrupt the transfer even when it is not targeted itself.

The $N_x = 4$, $N_y = 3$ network does not have any degenerate eigenstates, but if we move to a 5x5 network, for example, we can illustrate a nice feature of degenerate eigenstates. In this case there is a 5-fold degenerate 0 kHz eigenstate which we illustrate to the left in Fig. 5.21; we have put squares (circles) around the locations of the two sender (receiver) couplings. All senders and receivers target the zero eigenvalue and we can see from the routing dynamics on the right of the figure that these degenerate states are remarkably well protected from bleeding through each other. The behaviour is presumably due to the largely diagonal nature of the states with the two configurations above and below the legend in Fig. 5.21 forming the primary channels. Obviously this type of routing is not amenable to switching target receivers, but this network could be used as a multi-channel: one channel, but with multiple transport processes. It would be interesting to see whether this protection decayed more rapidly than the protection afforded by choosing different eigenvalues when an environment was present. Also, it is not immediately obvious if this degenerate eigenstate effect

would break down if the transport was anything other than perfectly simultaneous.
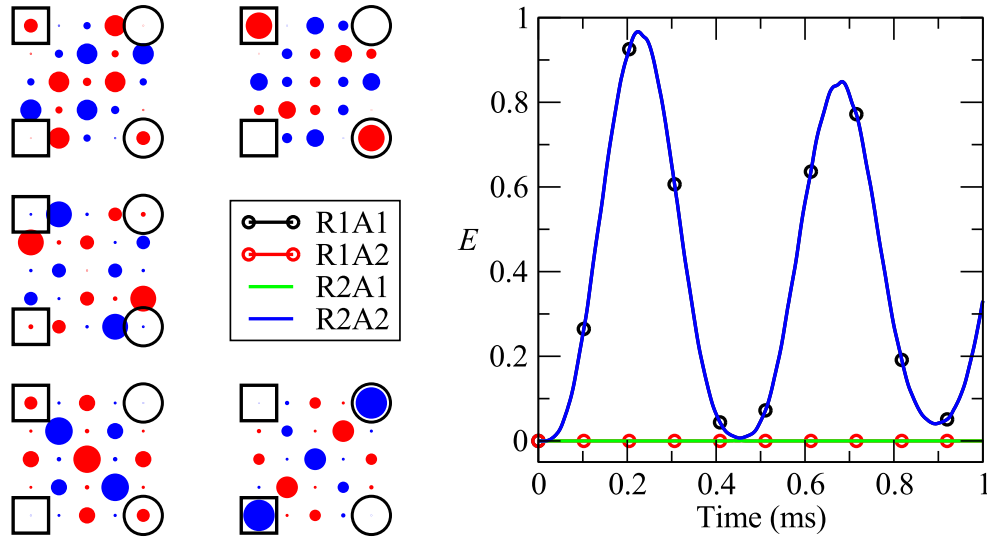

FIGURE 5.21: Left: The 5-fold degenerate $0\,$kHz eigenstates of the $N_x = N_y = 5$ network. Right: Successfully address simultaneous routing dynamics through these degenerate eigenstates.

The final thing we have to say concerning our small time spent exploring the vast parameter space of the double entanglement router is with regards to the processes in Eqs. (5.8)-(5.10). So far we have been targeting single excitation eigenstates and essentially using only the last two processes. To see if the first process is a viable option we need to find a double excitation eigenstate.

We will use an $N_x = 3$, $N_y = 2$ network for this discussion. The eigenstate structure in Fig. 5.3 remains, but our $\kappa = 200\,$kHz means $\varepsilon \in (\pm 482.8427, \pm 200, \pm 82.8427)\,$kHz. There are fourteen double excitation eigenstates with the highest energy two having eigenvalues 784.9363 and 489.8979 kHz. So, if we want to implement a process as in Eq. (5.8) with $\varepsilon_{R_1} = 482.8427\,$kHz we can try $\varepsilon_{R_2} \in (302.0936, 7.0552)\,$kHz. Both of the double excitation energy values are reasonably far from any single excitation value combination.

As we can see in Fig. 5.22 similar amplitude transfer across the network is possible for both pairs albeit with different time scales. This is understandable as in order to transfer to the second receiver an excitation must already be present in the network so as this excitation is transferred to its receiver the transfer of the second pair cannot proceed. There is a step-like structure to the second receiver's E dynamics that can

be seen (several instances are indicated with arrows) in the top panels that indicates this sort of dynamics. The 489.8979 kHz double excitation eigenstate would seem to not have a suitable PAP for the sender and receiver coupling locations used here. This can be seen in the bottom left panel of Fig. 5.22 where the entanglement between the second receiver and ancilla is weak.
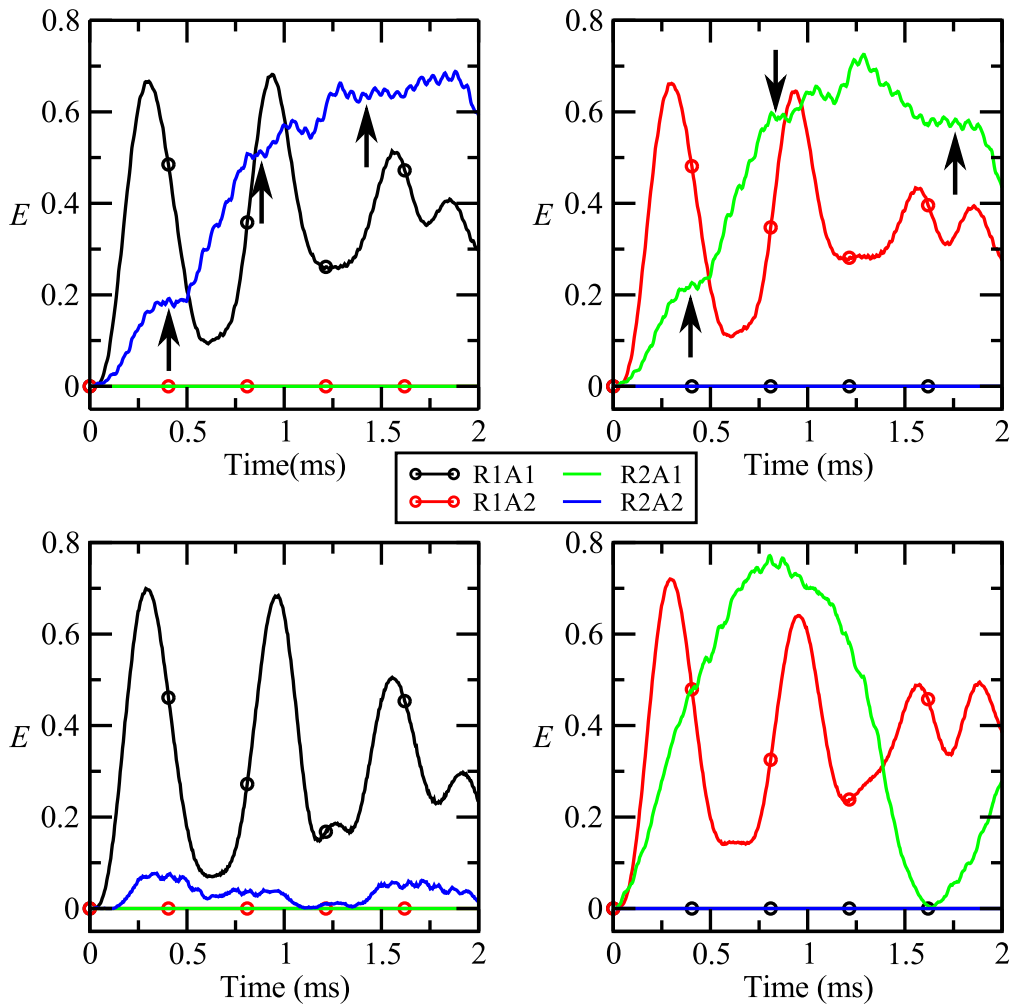

FIGURE 5.22: Routing dynamics implementing a double excitation pathway through our $\kappa = 200$ kHz $N_x = 3$, $N_y = 2$ network with top) $\varepsilon_{R_2} = 302.0936$ kHz and bottom) $\varepsilon_{R_2} = 7.0552$ kHz. On the left we have the first sender targeting the single excitation first receiver whereas on the right it targets the double excitation-bridging second receiver. It would appear that the 489.8979 kHz double excitation eigenstate (bottom) does not have a PAP that compliments our selection of sender and receiver coupling locations. Arrows indicate step-like structures corresponding to the blocked dynamics afforded by requiring the presence of the double excitation eigenstate.

5.4 Concluding remarks

WE have shown that it is undoubtedly possible to route one or two entanglement pairs through a network of spin-1/2 sites using eigenspectrum tunnelling. The presence of a dissipative environment both here and in the previous chapter has been shown to reduce the performance of such transfer but it does not prevent operation completely. The great number of configurations and parameters available for study mean that the work here has but scratched the surface of all possibilities however we have found systems that perform well.

There are a number of points we discovered and presented here that bear further investigation. Firstly, adding a third receiver to a well functioning two receiver, single sender routing set-up, with the intention of preserving the behaviour but adding another routing channel, has a small but noticeable disruptive effect. Understanding the extent of this phenomenon with different networks and eigenstates could lead to protection against such disruption.

Secondly the use of degenerate eigenstates seems to be remarkably robust and it would be interesting to find ways in which this can be exploited and indeed broken. Finally we have the use of the double excitation pathway: there are many double-single excitation eigenstate processes that can be implemented. A thorough search through them might unveil better matched transfer of both entanglement pairs for instance.

Adding more senders would be another route to explore: how many entanglement pairs can be transferred through one network? Each extra sender requires extension of the excitation subspace though which begins to limit the size of network which can be efficiently simulated. Another equally rewarding but simpler pathway would be to look at deviation from the simultaneous transfer studies present here; starting transfer of one pair and then sometime later activating the coupling of the second sender. We do not believe this would prevent routing processes and the single excitation transfer schemes should behave much the same and carry on in parallel with each other. So while we have presented an investigation and proof that routing is possible, this clearly not a completed area of research.

6

In closing

6.1 An overview

THE chapters of this thesis have covered many aspects of the diverse field of open quantum systems (OQS). We started in Chapter 1 with an introduction to the field, taking time to familiarise the reader with some of the areas work has been focussed. Firstly we explored how photosynthesis is expanding beyond the domains of biologists and chemists and into the realm of the physicist. Advances in measurement and theory have allowed us to probe the nature of the energy transfer in the light harvesting complexes that mediate an absorbed photon's excitonic transfer to the chemical centre of the process. Discoveries that such transfer may be quantum mechanical in nature, with long lived coherences, has led to a fervent discussion as to what exactly the source of the coherence protection is in a quantum photosynthetic system or indeed what its functional role might be. Part of this discussion turns its attention to the interplay between the protein environment and the molecular exciton transfer sites; a perfect topic to frame in OQS language.

We also introduced quantum state transfer in the context of spin-1/2 chains and while that may sound specific it is still a rich area of investigation. The theoretical approach of tunnelling through an eigenstate of such chains to achieve high fidelity transfer in dissipationless systems was reviewed. Further, a physical implementation was discussed, nitrogen-vacancy centre qubits and nitrogen impurity chains, a system in which the dissipation, mediated by the surrounding crystalline environment, has been shown to prohibitively lower state transfer fidelity. However, the notions of

entanglement distillation from weakly entangled pairs have been demonstrated to be a good fit for such a system where dissipative transfer of entanglement can be achieved. The question arises as to whether the spin chain geometry can be improved upon: clearly here we have another OQS ripe for further investigation.

In Chapter 2 we introduced the mathematical techniques and formalisms that make the work in the subsequent chapters possible. Density matrices allow us to go beyond pure state descriptions, moving to systems that incorporate mixing, an invaluable tool when dealing with the environmental effects of OQS. Equations of motion for density matrices were presented, as was the matrix product formalism: a tool for their efficient solution. We also described our simulation and measurement processes.

The next three chapters were accounts of the research carried out over the course of this period of study. Rather than give a review of these chapters, which all three feature in their respective 'Concluding remarks' sections, we here seek to tie them to each other and the broader scope of OQS. The common thread of course throughout the chapters is our use of OQS methods, even at the end of Chapter 5 where we neglect dissipation. But more than this, from the simple system of Chapter 3, through the grounded physical implementation of Chapter 4, to the theoretical proposal of Chapter 5, we are considering the behaviour of information: the persistence of 'quantumness' and the mechanisms for transferring it, hence the thesis title.

Whilst not a direct enquiry, the work of Chapter 3 was initially motivated by the role of quantum mechanics in photosynthesis: what can we still learn from simple models that can inform our understanding of realisations of OQSs? That question sums up the motivation behind all three chapters, to a varying degree. Featuring possibly the simplest model of a two level system, single mode and environment, following a decidedly not simple master equation derivation, our investigation in Chapter 3 produced the very interesting result that the interaction of the environment and the single mode can enhance the coherence of the two level system. Arguably still a simple model, the spin-1/2 channels of Chapter 4 and their nitrogen vacancy qubits were treated with the ever evolving matrix product formalism providing an informative study beyond traditional limits for realistic systems and traditional applications of

the formalism. Finally the routing investigation in Chapter 5 features a simple, albeit non-trivial to code, approach which offers an interesting extension of the concept of entanglement transfer. The three chapters successfully contribute new discoveries, complementing old, using and pushing OQS techniques to obtain answers to questions asked simply but, by no means answered trivially or with trivial answers.

6.2   Impact

IT is a rarity in science that a piece of work leaves all questions answered in a field or investigates all lines of inquiry. What is documented here is no exception to this trend. The work in Chapter 3 exists in an area where there is a wide amount of work on similar models and so proposals to extend the number of bosonic modes included must bear this body of previous work in mind. In general it can be said that our work should provide further reason to continue along the paths of using simple models to investigate complex phenomena and of investigating environmental-system interplay. Specifically, working closely with a physical implementation, perhaps along the lines of the reservoir engineering mentioned in Sec. 3.5, to consider a specific environment structure and system would be a nice application of the theory put forward in this work.

Physical implementation is the motivation behind the study in Chapter 4, but obviously concerning a different problem than in the previous chapter. Extensions of the work here could entail other channel structures, for example the direction taken in Chapter 5, or the application of other matrix product-type formalisms. For example, the projected entangled pair states (PEPS) formalism allows state approximation in a similar way to the matrix product methods we used, however they allow generalisation to higher dimension systems [109]. Alternatively one could think of tackling another system with similar schemes, such as DNA and its electrical conductivity [182] or ideas of carbon nanotubes as quantum wires [183].

Following our look, in Chapter 5, at what is possible with entanglement routing through spin-1/2 networks, one possible next step would be to introduce coupling variation and the idea of imperfect networks, as we did in the chapter preceding it.

A necessary consideration then would be obtaining the eigenspectrum of a 'broken' network which is so important for the routing processes. Another path to follow would be, again, the route of finding an implementation. The choice of the parameter values at the start of Sec. 5.2 were meant to put one in mind of a nitrogenic diamond implementation similar to Chapter 4. One other promising system for this sort of quantum routing is optical lattice quantum systems [184] which are robust to several forms of decoherence [185] and can be manipulated using sophisticated control of potentials [186].

Importantly though we hope this body of work holds together as a cohesive testament to what is achievable with OQS thinking, is approachable for those who wish to learn and informative for those who wish to build upon it.

Bibliography

[1] H. Breuer and F. Petruccione, *The Theory of Open Quantum Systems* (OUP Oxford, 2007).

[2] Á. Rivas and S. Huelga, *Open Quantum Systems: An Introduction*, SpringerBriefs in Physics (Springer Berlin Heidelberg, 2011).

[3] G. S. Engel, T. R. Calhoun, E. L. Read, T.-K. Ahn, T. Mancal, Y.-C. Cheng, R. E. Blankenship, and G. R. Fleming, Nature **446**, 782 (2007).

[4] Y.-C. Cheng and G. R. Fleming, Annual Review of Physical Chemistry **60**, 241 (2009).

[5] E. Collini, C. Y. Wong, K. E. Wilk, P. M. G. Curmi, P. Brumer, and G. D. Scholes, Nature **463**, 644 (2010).

[6] F. D. Fuller, J. Pan, A. Gelzinis, V. Butkus, S. S. Senlik, D. E. Wilcox, C. F. Yocum, L. Valkunas, D. Abramavicius, and J. P. Ogilvie, Nat Chem **6**, 706 (2014).

[7] E. Romero, R. Augulis, V. I. Novoderezhkin, M. Ferretti, J. Thieme, D. Zigmantas, and R. van Grondelle, Nat Phys **10**, 676 (2014), article.

[8] J. Lim, D. Palecek, F. Caycedo-Soler, C. N. Lincoln, J. Prior, H. von Berlepsch, S. F. Huelga, M. B. Plenio, D. Zigmantas, and J. Hauer, Nat Commun **6** (2015), article.

[9] F. Novelli, A. Nazir, G. H. Richards, A. Roozbeh, K. E. Wilk, P. M. G. Curmi, and J. A. Davis, The Journal of Physical Chemistry Letters **6**, 4573 (2015), pMID: 26528956, http://dx.doi.org/10.1021/acs.jpclett.5b02058 .

[10] G. Ritschel, J. Roden, W. T. Strunz, and A. Eisfeld, New Journal of Physics **13**, 113034 (2011).

[11] C. Kreisbeck and T. Kramer, The Journal of Physical Chemistry Letters **3**, 2828 (2012), http://dx.doi.org/10.1021/jz3012029 .

[12] M. del Rey, A. W. Chin, S. F. Huelga, and M. B. Plenio, The Journal of Physical Chemistry Letters **4**, 903 (2013), pMID: 26291354, http://dx.doi.org/10.1021/jz400058a .

[13] A. W. Chin, J. Prior, R. Rosenbach, F. Caycedo-Soler, S. F. Huelga, and M. B. Plenio, Nat Phys **9**, 113 (2013).

[14] E. K. Irish, R. Gómez-Bombarelli, and B. W. Lovett, Phys. Rev. A **90**, 012510 (2014).

[15] N. Killoran, S. F. Huelga, and M. B. Plenio, The Journal of Chemical Physics **143**, 155102 (2015), http://dx.doi.org/10.1063/1.4932307.

[16] A. G. Dijkstra, C. Wang, J. Cao, and G. R. Fleming, The Journal of Physical Chemistry Letters **6**, 627 (2015), pMID: 26262477, http://dx.doi.org/10.1021/jz502701u .

[17] P. Nalbach, C. A. Mujica-Martinez, and M. Thorwart, Phys. Rev. E **91**, 022706 (2015).

[18] A. Shabani, M. Mohseni, H. Rabitz, and S. Lloyd, Phys. Rev. E **89**, 042706 (2014).

[19] D. A. Mazziotti, The Journal of Chemical Physics **137**, 074117 (2012).

[20] F. Fassioli, R. Dinshaw, P. C. Arpin, and G. D. Scholes, Journal of The Royal Society Interface **11** (2014).

[21] G. D. Scholes and C. Smyth, The Journal of Chemical Physics **140**, 110901 (2014).

[22] A. Ishizaki and G. R. Fleming, Annual Review of Condensed Matter Physics **3**, 333 (2012), http://www.annualreviews.org/doi/pdf/10.1146/annurev-conmatphys-020911-125126 .

[23] I. Kassal, J. Yuen-Zhou, and S. Rahimi-Keshari, The Journal of Physical Chemistry Letters **4**, 362 (2013), http://pubs.acs.org/doi/pdf/10.1021/jz301872b .

[24] A. C. Han, M. Shapiro, and P. Brumer, The Journal of Physical Chemistry A **117**, 8199 (2013), http://dx.doi.org/10.1021/jp4023986 .

[25] A. Chenu, P. Malý, and T. Mančal, Chemical Physics **439**, 100 (2014).

[26] M. B. Plenio, J. Almeida, and S. F. Huelga, The Journal of Chemical Physics **139**, 235102 (2013).

[27] L. Viani, M. Corbella, C. Curutchet, E. J. O'Reilly, A. Olaya-Castro, and B. Mennucci, Phys. Chem. Chem. Phys. **16**, 16302 (2014).

[28] V. Butkus, L. Valkunas, and D. Abramavicius, The Journal of Chemical Physics **137**, 044513 (2012).

[29] G. D. Scholes, Nat Phys **7**, 448 (2011).

[30] M. Archer and J. Barber, *Molecular to global photosynthesis*, Series on photoconversion of solar energy (Imperial College Press, 2004).

[31] G. E. Bartley and P. A. Scolnik, The Plant Cell Online **7**, 1027 (1995), http://www.plantcell.org/content/7/7/1027.full.pdf+html .

[32] E. Gudowska-Nowak, M. D. Newton, and J. Fajer, The Journal of Physical Chemistry **94**, 5795 (1990), http://pubs.acs.org/doi/pdf/10.1021/j100378a036 .

[33] G. Oostergetel, H. Amerongen, and E. Boekema, Photosynthesis Research **104**, 245 (2010).

[34] G. S. Engel, Procedia Chemistry **3**, 222 (2011).

[35] G. S. Schlau-Cohen, A. Ishizaki, and G. R. Fleming, Chemical Physics **386**, 1 (2011).

[36] G. D. Scholes, Annual Review of Physical Chemistry **54**, 57 (2003), pMID: 12471171, http://www.annualreviews.org/doi/pdf/10.1146/annurev.physchem.54.011002.103746 .

[37] M. Yang and G. R. Fleming, Chemical Physics **275**, 355 (2002).

[38] H. E. Brandt, Proc. SPIE **5115**, 308 (2003).

[39] W. H. Zurek, Rev. Mod. Phys. **75**, 715 (2003).

[40] M. Schlosshauer, Rev. Mod. Phys. **76**, 1267 (2005).

[41] J. N. Eckstein and J. Levy, MRS Bulletin **38**, 783 (2013).

[42] S. Fortin, O. Lombardi, and M. Castagnino, Brazilian Journal of Physics **44**, 138 (2014).

[43] S. Fortin and L. Vanni, Foundations of Physics , 1 (2014).

[44] Y. Yao, L. Duan, Z. Lü, C.-Q. Wu, and Y. Zhao, Phys. Rev. E **88**, 023303 (2013).

[45] A. Kay, International Journal of Quantum Information **08**, 641 (2010), http://www.worldscientific.com/doi/pdf/10.1142/S0219749910006514 .

[46] S. Bose, Contemporary Physics **48**, 13 (2007), http://dx.doi.org/10.1080/00107510701342313 .

[47] D. Burgarth and S. Bose, New Journal of Physics **7**, 135 (2005).

[48] Z.-X. Man, N. B. An, Y.-J. Xia, and J. Kim, Annals of Physics **351**, 739 (2014).

[49] D. Burgarth, V. Giovannetti, and S. Bose, Journal of Physics A: Mathematical and General **38**, 6793 (2005).

[50] M. Christandl, N. Datta, A. Ekert, and A. J. Landahl, Phys. Rev. Lett. **92**, 187902 (2004).

[51] K. Eckert, O. Romero-Isart, and A. Sanpera, New Journal of Physics **9**, 155 (2007).

[52] S. Lorenzo, T. J. G. Apollaro, A. Sindona, and F. Plastina, Phys. Rev. A **87**, 042313 (2013).

[53] A. Zwick, G. A. Álvarez, G. Bensky, and G. Kurizki, New Journal of Physics **16**, 065021 (2014).

[54] A. O. Lyakhov and C. Bruder, Phys. Rev. B **74**, 235303 (2006).

[55] A. Zwick, G. A. Álvarez, J. Stolze, and O. Osenda, Phys. Rev. A **85**, 012318 (2012).

[56] N. Y. Yao, L. Jiang, A. V. Gorshkov, Z.-X. Gong, A. Zhai, L.-M. Duan, and M. D. Lukin, Phys. Rev. Lett. **106**, 040505 (2011).

[57] W. B. Gao, A. Imamoglu, H. Bernien, and R. Hanson, Nat Photon **9**, 363 (2015), review.

[58] L. Rondin, J.-P. Tetienne, T. Hingant, J.-F. Roch, P. Maletinsky, and V. Jacques, Reports on Progress in Physics **77**, 056503 (2014).

[59] G. Balasubramanian, P. Neumann, D. Twitchen, M. Markham, R. Kolesov, N. Mizuochi, J. Isoya, J. Achard, J. Beck, J. Tissler, V. Jacques, P. R. Hemmer, F. Jelezko, and J. Wrachtrup, Nat Mater **8**, 383 (2009).

[60] L. Childress, M. V. Gurudev Dutt, J. M. Taylor, A. S. Zibrov, F. Jelezko, J. Wrachtrup, P. R. Hemmer, and M. D. Lukin, Science **314**, 281 (2006).

[61] N. Y. Yao, L. Jiang, A. V. Gorshkov, P. C. Maurer, G. Giedke, J. I. Cirac, and M. D. Lukin, Nat Commun **3**, 800 (2012).

[62] P. Cappellaro, L. Jiang, J. S. Hodges, and M. D. Lukin, Phys. Rev. Lett. **102**, 210502 (2009).

[63] Y. Ping, B. W. Lovett, S. C. Benjamin, and E. M. Gauger, Phys. Rev. Lett. **110**, 100503 (2013).

[64] J. R. Weber, W. F. Koehl, J. B. Varley, A. Janotti, B. B. Buckley, C. G. Van de Walle, and D. D. Awschalom, Proceedings of the National Academy of Sciences **107**, 8513 (2010), http://www.pnas.org/content/107/19/8513.full.pdf .

[65] F. Jelezko, T. Gaebel, I. Popa, A. Gruber, and J. Wrachtrup, Phys. Rev. Lett. **92**, 076401 (2004).

[66] M. Nielsen and I. Chuang, *Quantum Computation and Quantum Information: 10th Anniversary Edition* (Cambridge University Press, 2010).

[67] C. H. Bennett, G. Brassard, C. Crépeau, R. Jozsa, A. Peres, and W. K. Wootters, Phys. Rev. Lett. **70**, 1895 (1993).

[68] A. K. Ekert, Phys. Rev. Lett. **67**, 661 (1991).

[69] R. Horodecki, P. Horodecki, M. Horodecki, and K. Horodecki, Rev. Mod. Phys. **81**, 865 (2009).

[70] V. Giovannetti, S. Lloyd, and L. Maccone, Nat Photon **5**, 222 (2011).

[71] G. Tóth and I. Apellaniz, Journal of Physics A: Mathematical and Theoretical **47**, 424006 (2014).

[72] T. S. Cubitt, F. Verstraete, W. Dür, and J. I. Cirac, Phys. Rev. Lett. **91**, 037902 (2003).

[73] L. Mišta and N. Korolkova, Phys. Rev. A **77**, 050302 (2008).

[74] A. Fedrizzi, M. Zuppardo, G. G. Gillett, M. A. Broome, M. P. Almeida, M. Paternostro, A. G. White, and T. Paterek, Phys. Rev. Lett. **111**, 230504 (2013).

[75] C. Peuntinger, V. Chille, L. Mišta, N. Korolkova, M. Förtsch, J. Korger, C. Marquardt, and G. Leuchs, Phys. Rev. Lett. **111**, 230506 (2013).

[76] C. E. Vollmer, D. Schulze, T. Eberle, V. Händchen, J. Fiurášek, and R. Schnabel, Phys. Rev. Lett. **111**, 230505 (2013).

[77] Q. Guo, L.-Y. Cheng, L. Chen, H.-F. Wang, and S. Zhang, Opt. Express **22**, 8970 (2014).

[78] L. Vaidman, Journal of Physics A: Mathematical and Theoretical **48**, 465303 (2015).

[79] C. H. Bennett, H. J. Bernstein, S. Popescu, and B. Schumacher, Phys. Rev. A **53**, 2046 (1996).

[80] C. H. Bennett, G. Brassard, S. Popescu, B. Schumacher, J. A. Smolin, and W. K. Wootters, Phys. Rev. Lett. **76**, 722 (1996).

[81] C. H. Bennett, D. P. DiVincenzo, J. A. Smolin, and W. K. Wootters, Phys. Rev. A **54**, 3824 (1996).

[82] D. Zueco, F. Galve, S. Kohler, and P. Hänggi, Phys. Rev. A **80**, 042303 (2009).

[83] P. Kok and B. Lovett, *Introduction to Optical Quantum Information Processing* (Cambridge University Press, 2010).

[84] M. Schlosshauer, *Decoherence: And the Quantum-To-Classical Transition*, The Frontiers Collection (Springer, 2007).

[85] A. Kolli, E. J. O'Reilly, G. D. Scholes, and A. Olaya-Castro, The Journal of Chemical Physics **137**, 174109 (2012).

[86] D. P. S. McCutcheon and A. Nazir, The Journal of Chemical Physics **135**, 114501 (2011).

[87] D. P. S. McCutcheon and A. Nazir, New Journal of Physics **12**, 113042 (2010).

[88] A. Kolli, A. Nazir, and A. Olaya-Castro, The Journal of Chemical Physics **135**, 154112 (2011).

[89] N. Makri and D. E. Makarov, The Journal of Chemical Physics **102**, 4600 (1995).

[90] N. Makri and D. E. Makarov, The Journal of Chemical Physics **102**, 4611 (1995).

[91] J. Dalibard, Y. Castin, and K. Mølmer, Phys. Rev. Lett. **68**, 580 (1992).

[92] C. H. Mak and R. Egger, Phys. Rev. E **49**, 1997 (1994).

[93] Y. Tanimura and R. Kubo, Journal of the Physical Society of Japan **58**, 101 (1989).

[94] H. Wang, The Journal of Physical Chemistry A **119**, 7951 (2015), pMID: 26020459, http://dx.doi.org/10.1021/acs.jpca.5b03256 .

[95] M. Beck, A. Jäckle, G. Worth, and H.-D. Meyer, Physics Reports **324**, 1 (2000).

[96] F. B. Anders and A. Schiller, Phys. Rev. Lett. **95**, 196801 (2005).

[97] J. Prior, A. W. Chin, S. F. Huelga, and M. B. Plenio, Phys. Rev. Lett. **105**, 050404 (2010).

[98] F. A. Y. N. Schröder and A. W. Chin, Phys. Rev. B **93**, 075105 (2016).

[99] N. Zhou, Z. Huang, J. Zhu, V. Chernyak, and Y. Zhao, The Journal of Chemical Physics **143**, 014113 (2015), http://dx.doi.org/10.1063/1.4923009.

[100] S. Bera, N. Gheeraert, S. Fratini, S. Ciuchi, and S. Florens, Phys. Rev. B **91**, 041107 (2015).

[101] G. Vidal, Phys. Rev. Lett. **91**, 147902 (2003).

[102] I. Affleck, T. Kennedy, E. H. Lieb, and H. Tasaki, Phys. Rev. Lett. **59**, 799 (1987).

[103] I. Affleck, T. Kennedy, E. H. Lieb, and H. Tasaki, Communications in Mathematical Physics **115**, 477 (1988).

[104] M. Fannes, B. Nachtergaele, and R. F. Werner, EPL (Europhysics Letters) **10**, 633 (1989).

[105] S. Rommer and S. Östlund, Phys. Rev. B **55**, 2164 (1997).

[106] R. Rosenbach, *Numerical Simulation Approaches for the Spin-Boson Model with Applications*, Ph.D. thesis, University of Ulm (2011).

[107] G. Stewart, *Introduction to matrix computations*, Computer science and applied mathematics (Academic Press, 1973).

[108] M. G. E. Perotti, *Matrix Product Formalism*, Ph.D. thesis, Technische Universität München (2005).

[109] R. Orús, Annals of Physics **349**, 117 (2014).

[110] U. Schollwöck, Annals of Physics **326**, 96 (2011), january 2011 Special Issue.

[111] F. Verstraete, J. J. García-Ripoll, and J. I. Cirac, Phys. Rev. Lett. **93**, 207204 (2004).

[112] M. Zwolak and G. Vidal, Phys. Rev. Lett. **93**, 207205 (2004).

[113] M. Suzuki, Communications in Mathematical Physics **51**, 183 (1976).

[114] M. Suzuki, Physics Letters A **146**, 319 (1990).

[115] W. Janke and T. Sauer, Physics Letters A **165**, 199 (1992).

[116] G. Vidal, Phys. Rev. Lett. **93**, 040502 (2004).

[117] E. Mascarenhas, H. Flayac, and V. Savona, Phys. Rev. A **92**, 022116 (2015).

[118] G. Arfken, H. Weber, and F. Harris, *Mathematical Methods for Physicists: A Comprehensive Guide* (Elsevier, 2012).

[119] M. A. Sbaih, M. K. Srour, M. Hamada, and H. Fayad, Electronic Journal of Theoretical Physics **10**, 9 (2013).

[120] M. B. Plenio and S. Virmani, Quantum Information and Computation **7**, 001 (2007).

[121] L. Amico, R. Fazio, A. Osterloh, and V. Vedral, Rev. Mod. Phys. **80**, 517 (2008).

[122] W. K. Wootters, Phys. Rev. Lett. **80**, 2245 (1998).

[123] A. Wallraff, D. I. Schuster, A. Blais, L. Frunzio, R.-S. Huang, J. Majer, S. Kumar, S. M. Girvin, and R. J. Schoelkopf, Nature **431**, 162 (2004).

[124] A. D. O'Connell, M. Hofheinz, M. Ansmann, R. C. Bialczak, M. Lenander, E. Lucero, M. Neeley, D. Sank, H. Wang, M. Weides, J. Wenner, J. M. Martinis, and A. N. Cleland, Nature **464**, 697 (2010).

[125] M. Thorwart, E. Paladino, and M. Grifoni, Chemical Physics **296**, 333 (2004), the Spin-Boson Problem: From Electron Transfer to Quantum Computing ... to the 60th Birthday of Professor Ulrich Weiss.

[126] F. Brito and A. O. Caldeira, New Journal of Physics **10**, 115014 (2008).

[127] J. Hausinger and M. Grifoni, New Journal of Physics **10**, 115015 (2008).

[128] C. Gan, P. Huang, and H. Zheng, Journal of Physics: Condensed Matter **22**, 115301 (2010).

[129] J. Iles-Smith, N. Lambert, and A. Nazir, Phys. Rev. A **90**, 032114 (2014).

[130] H. Hossein-Nejad and G. D. Scholes, New Journal of Physics **12**, 065045 (2010).

[131] H. Hossein-Nejad, V. V. Albert, E. J. O'Reilly, and G. D. Scholes, New Journal of Physics **16**, 019502 (2014).

[132] H.-B. Chen, J.-Y. Lien, C.-C. Hwang, and Y.-N. Chen, Phys. Rev. E **89**, 042147 (2014).

[133] E. J. O'Reilly and A. Olaya-Castro, Nat Commun **5** (2014).

[134] U. Weiss, *Quantum Dissipative Systems*, Series in modern condensed matter physics (World Scientific, 2008).

[135] A. J. Leggett, S. Chakravarty, A. T. Dorsey, M. P. A. Fisher, A. Garg, and W. Zwerger, Rev. Mod. Phys. **59**, 1 (1987).

[136] F. Wilhelm, S. Kleff, and J. von Delft, Chemical Physics **296**, 345 (2004).

[137] H. Wang and M. Thoss, New Journal of Physics **10**, 115005 (2008).

[138] A. Ishizaki and G. R. Fleming, The Journal of Chemical Physics **130**, 234111 (2009).

[139] R. L. Fulton and M. Gouterman, The Journal of Chemical Physics **35**, 1059 (1961).

[140] M. Wagner, Journal of Physics A: Mathematical and General **17**, 2319 (1984).

[141] M. Wagner, Journal of Physics A: Mathematical and General **17**, 3409 (1984).

[142] S. Paganelli and S. Ciuchi, Journal of Physics: Condensed Matter **18**, 7669 (2006).

[143] H. B. Shore and L. M. Sander, Phys. Rev. B **7**, 4537 (1973).

[144] M. Rapp and M. Wagner, Journal of Physics A: Mathematical and General **27**, 2239 (1994).

[145] A. A. Louis and J. P. Sethna, Phys. Rev. Lett. **74**, 1363 (1995).

[146] J. Johansson, P. Nation, and F. Nori, Computer Physics Communications **184**, 1234 (2013).

[147] E. K. Irish, J. Gea-Banacloche, I. Martin, and K. C. Schwab, Phys. Rev. B **72**, 195410 (2005).

[148] M. Haeberlein, F. Deppe, A. Kurcz, J. Goetz, A. Baust, P. Eder, K. Fedorov, M. Fischer, E. P. Menzel, M. J. Schwarz, F. Wulschner, E. Xie, L. Zhong, E. Solano, A. Marx, J.-J. García-Ripoll, and R. Gross, ArXiv e-prints (2015), arXiv:1506.09114 [cond-mat.mes-hall] .

[149] T. J. G. Apollaro, S. Lorenzo, and F. Plastina, International Journal of Modern Physics B **27**, 1345035 (2013), http://www.worldscientific.com/doi/pdf/10.1142/S0217979213450355 .

[150] V. Subrahmanyam, Phys. Rev. A **69**, 034304 (2004).

[151] S. Sarkar, Journal of Quantum Information Science **1**, 105 (2011).

[152] Y.-H. Ji and Y.-M. Liu, Optik - International Journal for Light and Electron Optics **126**, 2414 (2015).

[153] Z.-X. Man, N. B. An, Y.-J. Xia, and J. Kim, Physics Letters A **378**, 2063 (2014).

[154] Y. Li, T. Shi, B. Chen, Z. Song, and C.-P. Sun, Phys. Rev. A **71**, 022301 (2005).

[155] T. Yamamoto, T. Umeda, K. Watanabe, S. Onoda, M. L. Markham, D. J. Twitchen, B. Naydenov, L. P. McGuinness, T. Teraji, S. Koizumi, F. Dolde, H. Fedder, J. Honert, J. Wrachtrup, T. Ohshima, F. Jelezko, and J. Isoya, Phys. Rev. B **88**, 075206 (2013).

[156] D. Antonov, T. Häußermann, A. Aird, J. Roth, H.-R. Trebin, C. Müller, L. McGuinness, F. Jelezko, T. Yamamoto, J. Isoya, S. Pezzagna, J. Meijer, and J. Wrachtrup, Applied Physics Letters **104**, 012105 (2014).

[157] P. Cappellaro, L. Viola, and C. Ramanathan, Phys. Rev. A **83**, 032304 (2011).

[158] M. Markham, J. Dodson, G. Scarsbrook, D. Twitchen, G. Balasubramanian, F. Jelezko, and J. Wrachtrup, Diamond and Related Materials **20**, 134 (2011).

[159] A. Tallaire, M. Lesik, V. Jacques, S. Pezzagna, V. Mille, O. Brinza, J. Meijer, B. Abel, J. Roch, A. Gicquel, and J. Achard, Diamond and Related Materials **51**, 55 (2015).

[160] R. Hanson, F. M. Mendoza, R. J. Epstein, and D. D. Awschalom, Phys. Rev. Lett. **97**, 087601 (2006).

[161] C. Joshi, F. Nissen, and J. Keeling, Phys. Rev. A **88**, 063835 (2013).

[162] M. Schiró, C. Joshi, M. Bordyuh, R. Fazio, J. Keeling, and H. E. Türeci, Phys. Rev. Lett. **116**, 143603 (2016).

[163] X. Chen, C. Zou, Z. Gong, C. Dong, G. Guo, and F. Sun, Light Sci Appl **4**, e230 (2015), original Article.

[164] A. J. Häußler, P. Heller, L. P. McGuinness, B. Naydenov, and F. Jelezko, Opt. Express **22**, 29986 (2014).

[165] S. Takahashi, R. Hanson, J. van Tol, M. S. Sherwin, and D. D. Awschalom, Phys. Rev. Lett. **101**, 047601 (2008).

[166] N. Bar-Gill, L. M. Pham, A. Jarmola, D. Budker, and R. L. Walsworth, Nat Commun **4**, 1743 (2013).

[167] N. L. Johnson, S. Kotz, and N. Balakrishnan, *Continuous Univariate Distribution*, 2nd ed., Wiley series in probability and mathematical statistics: Applied probability and statistics, Vol. 1 (Wiley & Sons, 1994).

[168] K. Lemr, K. Bartkiewicz, A. Černoch, and J. Soubusta, Phys. Rev. A **87**, 062333 (2013).

[169] X. X. Yuan, J.-J. Ma, P.-Y. Hou, X.-Y. Chang, C. Zu, and L.-M. Duan, Scientific Reports **5**, 12452 EP (2015), article.

[170] W.-B. Yan and H. Fan, Scientific Reports **4**, 4820 EP (2014), article.

[171] K. Bartkiewicz, A. Černoch, and K. Lemr, Phys. Rev. A **90**, 022335 (2014).

[172] X.-Y. Chen, F.-Y. Zhang, and C. Li, J. Opt. Soc. Am. B **33**, 583 (2016).

[173] I.-C. Hoi, C. M. Wilson, G. Johansson, T. Palomaki, B. Peropadre, and P. Delsing, Phys. Rev. Lett. **107**, 073601 (2011).

[174] T. Aoki, A. S. Parkins, D. J. Alton, C. A. Regal, B. Dayan, E. Ostby, K. J. Vahala, and H. J. Kimble, Phys. Rev. Lett. **102**, 083601 (2009).

[175] X. Zhan, H. Qin, Z.-h. Bian, J. Li, and P. Xue, Phys. Rev. A **90**, 012331 (2014).

[176] A. Wójcik, T. Łuczak, P. Kurzyński, A. Grudka, T. Gdala, and M. Bednarska, Phys. Rev. A **75**, 022330 (2007).

[177] C. Facer, J. Twamley, and J. Cresser, Phys. Rev. A **77**, 012334 (2008).

[178] G. M. Nikolopoulos, Phys. Rev. Lett. **101**, 200502 (2008).

[179] S. Paganelli, S. Lorenzo, T. J. G. Apollaro, F. Plastina, and G. L. Giorgi, Phys. Rev. A **87**, 062309 (2013).

[180] M. B. Plenio and F. L. Semião, New Journal of Physics **7**, 73 (2005).

[181] P. J. Pemberton-Ross and A. Kay, Phys. Rev. Lett. **106**, 020503 (2011).

[182] H. Fink and C. Schonenberger, Nature **398**, 407 (1999).

[183] S. Tans, M. Devoret, H. Dai, A. Thess, R. Smalley, L. Geerligs, and C. Dekker, Nature **386**, 474 (1997).

[184] I. H. Deutsch, G. K. Brennen, and P. S. Jessen, Fortschritte der Physik **48**, 925 (2000).

[185] A. J. Daley, Quantum Information Processing **10**, 865 (2011).

[186] J.-F. Mennemann, D. Matthes, R.-M. Weishäupl, and T. Langen, New Journal of Physics **17**, 113027 (2015).